A. I. A. PC 338-1 PROJECT

INVESTIGATION OF ENGINE POWERLOSS AND INSTABILITY IN INCLEMENT WEATHER

SUB-COMMITTEE -- ENVIRONMENTAL DEFINITION (WEATHER - RAIN AND HAIL)

23 January 1991

TABLE OF CONTENTS

LIST OF SYMBOLS

b	A constant in the equation relating Z_c, Z_p, and A_c
c	(1) A correction factor used in the derivation of point hail duration (Section 5); (2) a correction factor to the Z_{max} values (Section 6); (3) a constant used in the equation for radar reflectivity of hail (Appendix B)
f( )	Probability density of original variate
k	A correction factor used in the derivation of the prior probability of hailstorms
m	A constant used in curve-fit equations for radar reflectivity of hail as a function of N_o and D_o for given values of t
n	Mean annual number of rain (or hail) cells that pass over a point
t	Liquid water coating thickness surrounding a hailstone
A	The average area in which a given LWC value is equalled or exceeded
A_c	The area enclosed by the Z_c contour
C_1	(1) A proportionality constant between T and D_e (Section 4); (2) a constant used in a set of five equations with five unknowns (Appendix B)
C_2	(1) A constant defined as $C_2 = n \times C_1/525960$ (Section 4); (2) a constant used in a set of five equations with five unknowns (Appendix B)
C_3-C_8	Constants used in a set of five equations with five unknowns (Appendix B)
D	Raindrop (or hailstone) effective diameter
D_e	The effective diameter of the cross-sectional area of which a given LWC value is equalled or exceeded
D_h	Hailshaft diameter
D_{max}	The largest raindrop (or hailstone) in a given distribution
D_{min}	The smallest hailstone in a given distribution
D_p	The assumed effective diameter of the cross-sectional area of which a given HWC value is equalled or exceeded
D_o	Median volume diameter
F( )	Cumulative distribution of original variate
K	Test statistic for the Kolmogoroff-Smirnov maximum deviation test

L	Distance across hailshaft at angle θ
M	Precipitation water content
N	Number of raindrops (or hailstones) having diameters between D and D + dD
N_o	The intercept of the dropsize (or stone size) distribution
P	Probability
P_c	Conditional probability
P_j	Joint probability
P_p	Prior probability
R	Rainrate
S	Hailshaft speed
T	Time it takes (in minutes) for a portion of a rain (or hail) cell that equals or exceeds a given water content to pass over a point
V	Hailstorm translation speed
Z	Radar reflectivity factor
Z_c	Some contour value (smaller than Z_p) about Z_p
Z_p	Core radar reflectivity factor at a given altitude
Z_{max}	The maximum reflectivity value of a cell defined as a "potential hail-producing" cell
α	(1) Exponent of D when N is given by a gamma distribution (Section 4); (2) a constant used in curve-fit equations for radar reflectivity of hail as a function of N_o and D_o for given values of t
γ	First shape parameter of the beta distribution
δ	Stochastic error
ϵ_B	Bias error
ε	A constant used in curve-fit equations for radar reflectivity of hail as a function of N_o and D_o for given values of t
ξ	Specific hailshaft diameter
η	Second shape parameter of the beta distribution
η_r	Radar reflectivity
θ	Flight path angle
λ	(1) Flight path length (Section 9); (2) radar wavelength (Appendix B)
ρ_w	Density of rain water
ρ_H	Density of hailstones
σ_b	Backscatter cross-section of hydrometeors

$\phi(\,)$	Probability density of transformed variate
$\Gamma(\,)$	Complete gamma function
ΔZ	Height above the freezing level
Λ	The slope parameter of the dropsize (or stone size) distribution
$\Phi(\,)$	Cumulative distribution of transformed variate

LIST OF FIGURES

LIST OF TABLES

1.0 Summary

The Aerospace Industries Association (AIA) initiated a study of precipitation water concentration from rain and hailstorms occurring at the world-wide worst-case locations for rain and hail. Graupel, snow, and mixtures of rain/hail were not considered in this study.

Curves were derived that show probability versus rain water content and hail water content. These curves apply at both a single point and for an airplane in flight. The rain curve that applies at a single point location indicates rain water contents of 15.3, 18.9, and 22.4 g m^{-3} at probability levels of 10^{-7}, 10^{-8}, and 10^{-9}, respectively. The single-point, Boeing-derived hail curve (based on ARC data) indicates hail water contents of 8.5, 12.5, and 16.5 g m^{-3} at probability levels of 10^{-7}, 10^{-8}, and 10^{-9}, respectively, while the CFMI-derived hail curve (based on GNEFA data) indicates hail water contents of 8.6, 13.4, and 18.1 g m^{-3} at the 10^{-7}, 10^{-8}, and 10^{-9} probability levels. A very good agreement considering that two completely different sets of weather data were utilized.

The rain and hail water content values listed above are assumed to apply at 19,700 feet MSL (rain), 15,000 feet MSL (Boeing-derived hail), and 12,000 feet MSL (CFMI-derived hail). Complete atmospheric vertical profiles for rain and hail are shown.

2.0 Introduction

The historical data, included in the AIA PC338-1 Study Results presented to the regulatory agencies on 6/7 June 1990, records the number of powerloss events that have been attributed to the effects of inclement weather. Many facets of severe weather have lead to engine powerloss, for instance; turbulence, lightning, wind shear, rain, hail, and/or supercooled liquid water. The scope of the analysis presented in this document, however, is limited to rain and hail.

The objective of the weather threat study (i. e., environmental definition) was to quantify the rain and hail threat in terms of a probability analysis and to ascertain if the current 4% water/air ratio (by weight) of FAR 33.77 (Department of Transportation, 1974) is an appropriate value for worldwide climatology of rain and hail storms. This was accomplished by developing curves that describe the probability of various rain and hail intensity levels occurring in the atmosphere and then comparing these intensity values against current regulations.. In the context of this study, "intensity" refers to the concentration of rain or hail given in units of grams of water per cubic meter ($g\ m^{-3}$). Further details of the quantification of the rain and hail threat are given in Section 3.0.

Considerably more data has been published on rain than on hail. A couple of likely explanations for this are; 1.) rain occurs much more frequently than hail, and 2.) there are more research aircraft equipped to fly into rain storms than into hail storms. Because of the scarcity of published hail data, both the Boeing Company and CFM International (CFMI) initiated contracts with atmospheric research institutions to provide hail data. The respective contractors were the Alberta Research Council in Edmonton, Alberta, Canada, and the Groupement National d'Etudes des Fléaux Atmosphériques in Aubiere, France. These agencies were contracted to supply hail data in terms of radar reflectivity measurements, storm size, etc. The analysis of these data were done by Boeing and CFMI with the goal of having a common definition of the hail threat from the two sets of data. This analyzed data has been provided to the AIA Propulsion Committee (PC) Project PC 338-1, "Investigation of Engine Powerloss and Instability in Inclement Weather", for their use in the study. All decisions on the use of this data were made by the project study group. In all subsequent reference to ARC and GNEFA data, it must be understood that only

the basic data source was supplied by those two organizations. Additional particulars of the rain and hail data sources are provided in Sections 4.1, 5.1, and 6.1.

In addition to the contract with ARC, Boeing also issued a contract to the South Dakota School of Mines and Technology (SDSMT) located in Rapid City, South Dakota. The Institute of Atmospheric Sciences (IAS) at SDSMT has the capability to numerically simulate rain and hail storms with a two-dimensional, time-dependent cloud model. Four storms in which commercial aircraft encountered heavy precipitation (three resulting in engine powerloss) were simulated by SDSMT. Further details and results of the SDSMT simulations are given in Section 10.0.

The results of the weather threat analysis are considered to apply at a single point in space in the "worst case" location. In other words, the rain and hail probability curves describe the likelihood of rain or hail, of a given intensity, occurring at the location in the world most likely to have that given intensity. The probability of an airplane encountering a particular rain or hail intensity over a period of time is discussed in Section 9.0.

3.0 Threat Definition

Water concentration was used to describe the level of intensity of rain and hail. For the remainder of this document, when discussing water concentration, the term *liquid water content* (LWC) will be used in association with rain. *Hail water content* (HWC) will be used when discussing hail. Unless stated otherwise, LWC and HWC will not include the contribution of water from cloud droplets. The basis for ignoring cloud water is that it is assumed that at high concentrations of precipitation, cloud water is swept out by the precipitation particles faster than it is generated in the cloud updraft. As mentioned in Section 2.0, LWC and HWC are given in units of grams of water per cubic meter ($g\ m^{-3}$). Precipitation other than rain and hail, including rain/hail mixtures, snow, and graupel (i.e., soft hail or snow pellets; c. f., Huschke, 1959), are not within the scope of this study.

This study assigns probability levels to given LWC and HWC values. In other words, it describes LWC and HWC as functions of probability:

$$LWC = f_1(P) \tag{3.1}$$

$$HWC = f_2(P) \tag{3.2}$$

In Eqs. (3.1) and (3.2) above, P is the joint probability of a rain or hail storm occurring at a given point *and* of the given LWC or HWC being equalled or exceeded at that point. Expressed symbolically:

$$P = P(\text{joint}) = P(\text{storm} \cap M) = P(\text{storm}) \times P(M|\text{storm}) \tag{3.3}$$

where M is water content (either LWC or HWC), P(storm) is the probability of a storm occurring at a given point and at a given instant, and P(M|storm) is the conditional probability of a given water concentration (M) value occurring at that point and time given the occurrence of the storm. It was assumed that LWC (or HWC) and P have a one-to-one relationship; therefore the probability of a given LWC value, P(LWC), or of a given HWC value, P(HWC), can also be expressed as functions of LWC and HWC:

$$P(LWC) = g_1(LWC) \tag{3.4}$$

$$P(HWC) = g_2(HWC) \tag{3.5}$$

where g_1 and g_2 are the inverse functions of f_1 and f_2 respectively.

Because the probability of a given water concentration (M) varies significantly as a function of location, the approach used was to consider the known "worst case" locations for rain and hail intensity, that is, those locations in the world where high LWC and HWC values have been reported to occur most frequently. This insures that any point in the world could be randomly chosen, at any random instant, and the probability of a given LWC or HWC occurring at that instant would be no higher than that given by Eqs. (3.4) or (3.5), respectively. The considerations discussed in this section shape the framework for the weather threat study as outlined in the following sections.

4.0 Rain

This section documents the portion of the weather analysis pertaining to rain. It is divided into three subsections. In Section 4.1 the data sources are given and discussed. In Section 4.2 the methodology used to develop the LWC probability curve is explained. In Section 4.3 the results and a discussion are presented.

4.1 Data Sources

As discussed previously P(LWC) and P(HWC) were defined as "instantaneous" probabilities (i. e., as the probability of a given LWC or HWC occurring at a given instant). In practice, though, there is a finite time interval over which a datum point is collected. Traditionally, rain data with a temporal resolution of one minute are considered indicative of the instantaneous rain rate. Most of the rain data used in this analysis were taken over one-minute intervals.

An important source of data came from Tattelman and Larson (1989). They analyzed one-minute rain rate data collected by weighing rain gages. Their data spans 10 years (1970-79) and includes 41 stations in the continental United States and one station in Puerto Rico (6-1/2 year data base). Annual average number of occurrences of rain rates from 0.0 to 2.5 mm min^{-1} (0.0 to 150 mm hr^{-1}) for durations ranging from 1 to 30 minutes are given (c. f., Fig. 4.1). Table 4.1 lists the 42 stations they examined; of these, Miami and Tallahassee, Florida had the highest annual average occurrences of 2.5 mm min^{-1} rain rates sustained over a one-minute period.

Bodtmann and Ruthroff (1976) analyzed five years (1966-70) of weighing rain gage data for 20 U. S. stations (Table 4.2). They give the annual average number of occurrences of rain rates from 20 to 280 mm hr^{-1} (0.33 to 4.67 mm min^{-1}) sustained over a one-minute period (c. f., Fig. 4.2). The highest rain rates in their data occurred at Miami.

Jones and Wendland (1984) gave the percent frequency above threshold rain rates for rates between ~4 x 10^{-3} and ~5.4 mm min^{-1} (~0.24 and ~324 mm hr^{-1}) at Urbana, Illinois (Fig. 4.3). These data, taken over a ten-year period from

1970-79, were particularly useful because the upper end, at ~5.4 mm min^{-1}, was higher than any data given by Bodtmann and Ruthroff (1976) or Tattelman and Larson (1989).

Roys and Kessler (1966) discussed water contents of thunderstorms in Oklahoma. Data were collected at altitudes above 25,000 feet by a F-100 airplane during the 1962 National Severe Storms Project. Water entering in the F-100's jet engine is evaporated as the air is warmed through compression. The compressed air is analyzed by a water vapor analyzer and compared to air collected in a reference cavity. This comparison yields the amount of water condensed in the engine. The largest of the 22 measured values of maximum water content reported, and discussed extensively, by Roys and Kessler (1966) was 43.7 g m^{-3}. The authors point out that this value is somewhat suspect, but it can not be ruled out, based on the available data. The other 21 values ranged from 1.2 to 13.8 g m^{-3} with an average value of 8.4 g m^{-3} (Table 4.3).

Finally, Briggs (1972) presented data from Freetown, Sierra Leone, Singapore, Singapore, and London (Heathrow), United Kingdom (Table 4.4) in a paper in which he derived curves of the intensity of rain, as a function of altitude, predicted to be met once in 10^5 flight hours by a Concorde airplane. Of the three locations, Freetown has the highest probability of occurrence of instantaneous rainfall at or exceeding 25, 50, and 100 mm hr^{-1}.

4.2 Methods of Analysis

Data from the disparate sources discussed in Section 4.1 above were evaluated so that individual data points could be plotted on a common graph with probability on the abscissa and LWC on the ordinate. An "envelope" fit gave LWC as a function of probability. The curve fitting technique is discussed in greater detail in Section 4.3.

A straightforward technique was used to convert the data of Tattelman and Larson (1989), Bodtmann and Ruthroff (1976), and Jones and Wendland (1984) to a common format. All three of these studies used rain rate on one of the axes of their plotted data (c.f., Figs. 4.1-4.3). The other axis was either annual average occurrences (Tattelman and Larson, 1989), number of minutes per

year rain rate is exceeded (Bodtmann and Ruthroff, 1976), or percent frequency above threshold rate (Jones and Wendland, 1984). Likewise, the methods to convert the Briggs (1972) data to the common format for this study were straightforward. The first step was to convert rain rates to LWC. The second step was to convert the other axis to exceedance probability.

There are a number of studies in which correlations between LWC (frequently designated "M") and rain rate (R) are reported. Rain rate and LWC are measured independently, but at the same time and location. A plot like that shown in Fig. 4.4 is the result. The points, when plotted on log-log paper, can usually be fit with a straight line, thus defining a power law relationship between M and R. Table 4.5 shows the M-R relations used in the rain analysis described here.

From the Tattelman and Larson (1989) data; Miami and Tallahassee, Florida and Oklahoma City, Oklahoma were the stations chosen to provide data points for the LWC vs. probability graph. Miami and Tallahassee were chosen because high intensity one-minute rain rates were most frequent at these two locations. Oklahoma City is a significant location, as will be discussed later in this section, because the Roys and Kessler data were also collected in Oklahoma. The rain rates at Miami and Tallahassee were converted to LWC using the Mueller and Sims (1966) equation from Table 4.5. The Oklahoma City data was converted using the Jones (1956) equation. The other axis of the Tattelman and Larson (1989) plots is the annual average occurrences. For this study the one-minute duration curves were used and the assumption was made that the probability of a given LWC value being exceeded is equal to the annual average number of minutes per year it is exceeded divided by the number of minutes in a year. The larger the sample population, the better is this assumption.

To clarify how a data point is generated, it is useful to go through the process step by step. For example, in Fig. 4.1 the one-minute duration curve (uppermost curve) shows that the 2.5 mm min^{-1} rain rate occurs ~11 times annually. So the LWC value, using the Mueller and Sims (1966) equation is:

$$LWC = M = 0.0528 \times R\ (= 150\ mm\ hr^{-1})^{0.95} = 6.2\ g\ m^{-3}$$

The probability level is calculated by taking the number of one-minute occurrences divided by the number of minutes in a year:

$$P(LWC) = \sim 11 / (365.25 \times 24 \times 60) = 2.1 \times 10^{-5}$$

So the data point, (P, LWC), is (2.1×10^{-5}, 6.2). This particular point can be seen plotted on Fig. 4.9.

Three data points were calculated from the Bodtmann and Ruthroff (1976) Miami data. Miami had the highest rain rates of the 20 stations in their database. The methods used to calculate the data points were the same as those used to reanalyze the Tattelman and Larson (1989) data.

Two data points were calculated from the Jones and Wendland (1984) Urbana, Illinois data. LWC was calculated from rain rates using the Jones (1956) equation in Table 4.5. Probability was calculated by dividing the axis labelled "percent frequency above threshold rate" by 100.

Two data points were calculated from the Briggs (1972) Freetown data. The 100 mm hr^{-1} data point, and an interpolated data point at 75 mm hr^{-1}, were converted to LWC using the Willis (1984) M-R equation from Table 4.5. Exceedance probability was already given, so no conversion was necessary.

As mentioned earlier, the methods to convert the data of Tattelman and Larson (1989), Bodtmann and Ruthroff (1976), Jones and Wendland (1984), and Briggs (1972) to a common format for this study were straightforward. Converting the Roys and Kessler (1966) data, however, was more complicated. The Roys and Kessler (1966) conditional probability data can be fit with an exponential function. Figure 4.5, from the Handbook of Geophysics and the Space Environment (Fig. 16.27, Jursa, 1985) illustrates the curve fit of the Roys and Kessler (1966) data. It shows the conditional probability, given the occurrence of an Oklahoma thunderstorm, of the maximum LWC within the thunderstorm exceeding a given value of LWC. For example, the curve in Fig. 4.5 indicates that the probability of the maximum LWC within an Oklahoma thunderstorm, P_C(LWC), exceeding 5 g m^{-3} is ~68 %.

The probability of a given LWC value, P(LWC), occurring at a given point at any given instant can be computed using the following equation:

$$P(LWC) = n \times P_c(LWC) \times T(LWC) / 525960 \qquad (4.1)$$

where n is the mean number of thunderstorm cells that pass over the point in a year, $P_c(LWC)$ is the conditional probability, given a thunderstorm, of a given maximum LWC value occurring within the cell, and T(LWC) is the time it takes (in minutes) for the portion of the cell that equals or exceeds the given LWC value to pass over the point. The number in the denominator, 525960, is the number of minutes in a year. $P_c(LWC)$ is given in the Handbook of Geophysics and the Space Environment (Jursa, 1985) as $P_c(LWC) = \exp(-LWC^2/64)$. The unknowns are n and T(LWC). Note that Eq. (4.1) is a specific version of the more general Eq. (3.4).

Figure 4.6 shows a simplified thunderstorm cell model. The concentric circles represent contours of LWC increasing towards the center of the cell. This model generalizes the LWC distribution within a cell. The larger the LWC value, the smaller the cross-sectional area it occupies. With other factors being equal, T(LWC) is proportional to $D_e(LWC)$, the effective diameter of the cross-sectional area of which a given LWC value is equalled or exceeded. If these "other factors" (most notably, cell speed) are independent of LWC, then:

$$T(LWC) = C_1 \times D_e(LWC)$$

where C_1 is the proportionality constant.

So, Eq. (4.1) can be rewritten as:

$$P(LWC) = C_2 \times P_c(LWC) \times D_e(LWC) \qquad (4.2)$$

where $C_2 = n \times C_1 / 525960$. $D_e(LWC)$ can be estimated independently, so if it can be shown that C_2, thereby implying C_1, is indeed constant and its value can be determined, then Eq. (4.2) can be evaluated.

Using the Tattelman and Larson (1989) Oklahoma City data, P(LWC) can be calculated directly by the methods discussed previously, with rain rates converted to LWC using the Jones (1956) equation from Table 4.5. This method gives P(LWC) for $0 \leq LWC \leq 6.7$ g m^{-3}. Equation 4.2 can then be rearranged to solve for C_2:

$$C_2 = P(LWC) / [P_c(LWC) \times D(LWC)] \qquad (4.3)$$

So C_2 can be determined directly for LWC values up to 6.7 g m^{-3} once $D_e(LWC)$ is known. As discussed above, if C_2 remains constant for all LWC values, then Eq. (4.2) can be used to calculate P(LWC) even for LWC > 6.7 g m^{-3}. Consider, however, that Eqs. 4.1 and 4.2 are based on physical arguments that assume thunderstorm rain. In the LWC range from 0 to 6.7 g m^{-3}, the lower values of LWC also occur in stratiform rain. So it might be expected that C_2, as calculated from Eq. (4.3), would not be constant for lower values of LWC, but would "level off" to a constant value as LWC increases, since stratiform rain rarely produces large values of LWC.

Figure 4.7 shows the diameter of the region in which a given LWC value is equalled or exceeded, $D_e(LWC)$, as a function of LWC. As expected, $D_e(LWC)$ decreases as LWC increases. It should be stressed that the curve applies to convective rain only. The methods to derive the curve in Fig. 4.7 are straightforward. The details are given in Appendix A.

The constant, C_2, in Eq. (4.3) can now be solved for, since P(LWC) is given from Tattelman and Larson (for LWC values to 6.7 g m^{-3}), $P_c(LWC)$ is given in the Handbook of Geophysics and the Space Environment (Jursa, 1985) as $P_c(LWC) = \exp(-LWC^2 / 64)$, and as shown in Appendix A, $D_e(LWC) = 4.3\ LWC^{-0.26} [\exp(\ln LWC)^2]^{-0.16}$. Figure 4.8 shows C_2 as a function of LWC. Note that by about LWC = 4.5 g m^{-3}, C_2 levels off to a constant value of $\sim 9.5 \times 10^6$. As discussed previously, this behavior is expected since Eqs. 4.1 - 4.3 were derived with assumptions based on a convective rain model, whereas stratiform rain accounts for much of the lower range of LWC values. The value of C_2 for $4.5 < LWC < 6.7$ g m^{-3} (i. e., $C_2 = 9.5 \times 10^6$) can now be used in Eq. (4.2) for LWC > 4.5 g m^{-3}.

With C_2, P_c(LWC), and D_e(LWC) known, Eq. (4.2) was used to calculate two low probability points, P(20 g m^{-3}) and P(25 g m^{-3}).

4.3 Results

Figure 4.9 shows the rain curve with the various data points, as discussed in the last section. At probability levels of 10^{-7}, 10^{-8}, and 10^{-9}, the corresponding LWC values are 15.3, 18.9, and 22.4 g m-3. The curve was determined by selecting only the highest LWC values in a cluster of data points and curve fitting the selected points. The values were chosen in this manner in order to define a curve that would apply in the worst case location. For example, data points from a location in the Sahara desert could easily have been plotted on Fig. 4.9, but it is clear that it would be unrepresentative for these points to influence the curve fit, since they clearly do not represent a worst case location. Points chosen for the curve fit were: the three Tattelman and Larson (1989) Tallahassee points, the two Roys and Kessler (1966) Oklahoma points, the three Bodtmann and Ruthroff (1976) Miami points, the two Briggs (1972) Freetown, Sierra Leone points, and the Jones and Wendland (1984) Urbana, Illinois point at 14.2 g m^{-3}. The Tattelman and Larson (1989) Miami points were not used, because the Tallahassee points at the same probability level were higher. The Tattelman and Larson (1989) Oklahoma data points also were not used, nor was the Jones and Wendland (1984) Urbana, Illinois data point at 6.7 g m^{-3}.

The data imply that subtropical locations like Florida have the highest probability of LWC values below 10 g m^{-3}, while mid-latitude continental interior locations like Urbana and/or Oklahoma have the highest probability of LWC values above 10 g m^{-3}. Physical arguments can be constructed to support this implication. Florida is located at latitudes below 31° N. where it gets relatively strong surface heating throughout the year. In addition, the state is surrounded by warm ocean water thus insuring a nearly constant supply of moisture laden air. Strong surface heating and an abundant moisture supply are the ideal recipe for convective precipitation, so it is not surprising that Florida experiences convective rainfall year-round. In the midwestern United States, like Oklahoma, there is strong surface heating in the spring and summer. Often the low-level winds are from the south to southeast at this time of the year, bringing warm moisture-laden air from the Gulf of Mexico. Unlike Florida,

however, a mid-level inversion often sets up under these conditions, particularly in the spring and early summer. The inversion inhibits convection until either the low-level temperatures are high enough to allow thermals (rising "bubbles" of warm air) to penetrate the inversion level or until low-level air is forced above the inversion level by a front. When the convection finally is released it can be more vigorous than Florida convection, thereby producing high LWC values. Oklahoma has the potential for very *severe* convection more often than Florida, but since convection is inhibited by the season and inversions, Florida has *moderate* convection more often than Oklahoma.

A reasonable check of the rain curve in Fig. 4.9 is to compare it with the MIL-STD-210C (Department of Defense, 1987) worst case 0.01%, 0.1%, and 0.5% values. Figure 4.10 shows the rain curve with the three MIL-STD-210C points plotted. These points lie above the curve, but it should be kept in mind that the MIL-STD-210C data, taken from Tattelman and Grantham (1983a,b), are the probabilities during the worst month, whereas the curve in Fig. 4.9 is based on annual probabilities. Considering this difference, then, the portion of the probability curve near the MIL-STD-210C points seems reasonable, although it can not be concluded that the MIL-STD-210C points validate the curve because of the differences in temporal scale.

Besides the data used to establish the rain probability curve in Fig. 4.9, a number of extreme LWC data points have been reported. The largest *in situ* rain LWC value is 44 g m^{-3} from an Oklahoma thunderstorm as reported by Roys and Kessler (1966). The world's record 1-minute and 42-minute rainfall of 1.23 inches at Unionville, Maryland on 4 July 1956 and 12 inches at Holt, Missouri on 22 June 1947 (Riordan and Bourget, 1985) translate to LWC values of 60.3 and 15.8 g m^{-3}, respectively (Willis, 1984; Department of Defense, 1987). Table 4.6 shows some extreme rain LWC data and associated data sources.

An important aspect of the weather threat analysis is the vertical distribution of rain LWC in the atmosphere. Table 4.7 shows the assumed profile for LWC used in this study. It implies that LWC is constant from the surface to 6 km MSL and drops off to 0 g m^{-3} at 20 km MSL (Tattelman and Willis, 1985; Department of Defense, 1987). Figure 4.11 shows the vertical distribution of normalized

LWC as determined using the values given in Table 4.7. This distribution is described as all liquid below ~15,000 ft MSL, mostly liquid between ~15,000 - 20,000 ft MSL, and nearly all ice above ~23,000 ft MSL (Department of Defense, 1987). However, recall that this distinction is not made here; i.e., the condensate is assumed to be liquid all the way to 20,000 ft MSL.

Another important aspect of the weather threat analysis is the raindrop size distribution. Marshall and Palmer (1948) reported an exponential distribution of the form:

$$N(D) = N_0 e^{-\Lambda D} \qquad (\text{for } 0 < D < D_{max}) \qquad (4.9)$$

where D is the raindrop diameter, N(D) is the number of drops having diameters between D and D + dD, Λ is the slope parameter, N_0 is the intercept, and D_{max} is the maximum drop diameter (usually taken to be ~0.6 - 0.65 mm, since drops larger than that tend to break up when falling). A refinement on Eq. (4.9) is a gamma distribution:

$$N(D) = N_0 D^{\alpha} e^{-\Lambda D} \qquad (0 < D < D_{max}) \qquad (4.10)$$

which reduces to Eq. (4.9) when $\alpha = 0$. Equation (4.11) below gives LWC:

$$LWC = \frac{1}{6}\rho_w \int_0^{D_{max}} N(D)\, D^3\, dD \qquad (4.11)$$

where ρ_w is the density of rain water. Tattelman and Willis (1985) use Eq. (4.10) to describe the drop size distribution with values for N_0, α, and Λ dependent on rainrate. Figure 4.12a shows the Tattelman and Willis (1985) drop size distribution for the 42-minute world record rainrate of 432 mm hr^{-1} (15.8 g m^{-3}). Approximately 72% of the rain drops are between 0.5 and 2.0 mm. The size category with the most raindrops is 1.0 < D < 1.5 mm, while the mean drop size is 1.4 mm in diameter. Figure 4.12b shows the percent contribution to the total water content from each 0.5 mm size interval. Approximately 75% of the total water content is from drops with diameters between 1.5 and 3.9 mm. The size category contributing the most to the total water content is 2.0 < D < 2.4 mm,

while the median volume diameter, D_o (i. e., the drop size that separates the distribution such that all drops smaller than D_o contribute the same liquid water content as all drops larger than than D_o) is 2.6 mm.

5.0 Hail - ARC

For the purpose of this study, hail is defined as frozen precipitation of a particle size 0.5 cm diameter or greater. This definition excludes smaller sized frozen precipitation, viz, graupel, sleet, snow pellets, etc. This section documents the portion of the weather analysis based on the data supplied to the Boeing company by the Alberta Research Council (ARC). While ARC supplied the data, the actual analysis was carried out by the Boeing Company. In Section 5.1, the ARC data is discussed. In Section 5.2, the methodology used by Boeing to develop a HWC curve, based on the ARC data, is explained. In Section 5.3, the ARC curve is presented and discussed.

5.1 ARC Data

The Alberta Research Council, located in Edmonton, Alberta, Canada, has been collecting weather data for many years. They are a world leader in hail research. As part of their extensive convective storm data base, they have S-band (10-cm wavelength, or 3 GHz) dual-polarization weather radar data from 1974 - 1985. Their S-band radar was operated any time significant weather was within the radar's range. The data were taken in volume scans, consisting of a series of plan-position indicator (PPI) scans (e. g., Battan, 1973) at increasing elevation angle. Each volume scan required either 1.5 or 3 minutes to complete depending on the antenna program in use.

ARC signed a contract with the Boeing Company in early 1989 to provide Boeing with radar data processed to Boeing's specifications (Alberta Research Council, 1990). Data from the month of July, the peak month of Alberta's hail season, from 1983, 1984, and 1985, the years with the best and most complete sets of S-band data, were processed. The PPI scans were converted to a constant-altitude plan-position indicator (CAPPI) format (c. f., East and Dore, 1957; Marshall, 1957; Fig. 5.1) at 2, 4, and 6 km above ground level (AGL); this corresponds to 2.7, 4.7, and 6.7 km above mean sea level (MSL), since the radar is located approximately 0.7 km MSL. Only data within the range interval of 31 to 81 km were used, thereby minimizing ground clutter close to the radar. The ARC data domain is illustrated in Fig. 5.2. Volume scans were extracted for processing from every 30 minutes of data. In addition, when large radar

reflectivity values were noted, then scans that fell in between the 30-minute sampling interval were interrogated in an attempt to find the extreme reflectivity value at each CAPPI altitude for each of the three years. As discussed in Section 5.3, these data were kept separate from the 30-minute data and were not used to derive the final P(HWC) curve.

Storm cells, defined as areas of contiguous echo above 30 dBZ, were identified in each CAPPI scan. The polarization capabilities of the radar allowed ARC to differentiate between regions of rain, hail only, or mixed (rain and hail) using algorithms developed by Dr. Anthony Holt at the University of Essex in the United Kingdom. Within each region of a given category, the maximum reflectivity was recorded. The area of each hail and mixed cell was also recorded and the equivalent diameter was computed ("equivalent diameter" in this case refers to the diameter of a circular region of the same area).

Table 5.1 gives a summary of the total hail data points. There are 414 maximum hail reflectivity data points (30-minute data) from the three July months of 1983-85. Additionally, there are 2868 hailshaft area (equivalent diameter) data points. There are more hailshaft area points than maximum hail reflectivity points because the hailshaft area data includes the mixed (rain and hail) regions. The data points were used to construct cumulative distribution plots of both equivalent diameter and maximum reflectivity.

5.2 Methods of Analysis

The hail curve, given by P(HWC), is a product of the prior probability of a hail storm occurring at a given point and the conditional probability of a given HWC value occurring within that hailstorm:

$$P(HWC) = P_p(HWC) \times P_c(HWC) \qquad (5.1)$$

Equation (5.1) applies specifically to hail, while Eq. (3.3) is a more general expression of the joint probability of a given water content from a convective storm. Comparing Eqs. (3.3) and (5.1), P(HWC) corresponds to P(storm$\cap$M), the prior probability of a hailstorm occurring at a given point is P_p(HWC) in Eq.

(5.1) corresponding to P(storm) in Eq. (3.3), and the conditional probability of HWC, given a hailstorm, is P_c(HWC) in Eq. (5.1) and P(M|storm) in Eq. (3.3).

The first step in the analysis was to convert the 414 hail reflectivity data points into HWC data points. There are a number of Z-M conversions for hail. The Ulbrich and Atlas (1982) conversion equation was used in this analysis because it gave relatively high HWC values in the range of reflectivity values of interest (cf. sec. 8.0 for additional discussion).

Because hail reflectivity is strongly influenced by the liquid water coating thickness, t, on the hailstones, the reflectivity values were corrected to account for this effect (c. f., Appendix B). The Ulbrich and Atlas (1982) equation:

$$Z = 9.22 \times 10^5 M^{1.23} \qquad (5.2)$$

assumes t = 0.01 cm. Because water coating thickness can not be measured directly, it was necessary to estimate t for the Alberta CAPPI altitudes. The reflectivity values were corrected and then converted to HWC using Eq. (5.2).

Liquid water melts and collects on a hailstone if the ambient air temperature is greater than 0°C, but it can also collect on the hailstones at temperatures less than 0°C if the stones are in a wet growth regime (c. f., Macklin and Bailey, 1968; Foote and Knight, 1977). Figure 5.3 shows that the growth regime (wet or dry) is determined by ambient temperature and cloud liquid water content. The mean freezing level in Alberta hailstorms in July is 3.5 km MSL (ARC, personal communication). So the 2.7 km MSL CAPPI level was below the mean hailstorm freezing level and the 4.7 and 6.7 km MSL levels were above the freezing level. It was assumed that hailstones at the 4.7 and 6.7 km MSL levels were growing in a wet-growth regime and that the water-coating thickness was t = 0.01 cm under those conditions. Therefore, the Ulbrich and Atlas (1982) equation could be applied directly to the reflectivity values at the 4.7 and 6.7 km MSL levels. For the 2.7 km MSL level, it was assumed that the stones had a water-coating thickness of t = 0.01 cm at the freezing level and that melting occurred as the stones fell below the freezing level to the 2.7 km MSL level.

The melting model described by Rasmussen and Heymsfield (1987a,b) was used to estimate the amount of melting that occurred as hailstones dropped from the freezing level, at 3.5 km MSL, to the CAPPI level at 2.7 km MSL. A hailstone size of 1.5 cm diameter was chosen for the model run, as representative of the median volume diameter, D_o. (The median volume diameter is the hailstone diameter that evenly splits the size distribution, such that all stones smaller than D_o contribute the same HWC as all stones larger than D_o; see Section 5.3). Figure 5.4 shows the atmospheric profiles used in the melting analysis. The model results estimated a water-coating thickness of t = 0.021 cm at 2.7 km MSL. This increase above the initial 0.01 cm was primarily a result of melting with a small contribution from the collection of cloud water.

The reflectivity values at 2.7 km MSL from the ARC data were corrected to "t = 0.01 cm equivalent reflectivity" values. In other words, the reflectivity values in the ARC data, assumed to be from hailstones coated with 0.021 cm of liquid water, were corrected to what they *would be* if the water coating was 0.01 cm. Since the 2.7 km MSL data was corrected for a t value assumed to be that at the freezing level, the 2.7 km MSL corrected data can be interpreted as actually representing data at the freezing level, 3.5 km MSL. Details of the correction applied to the 2.7 km MSL ARC data are contained in Appendix B.

Equation (5.2) was used to convert the t = 0.01 cm equivalent reflectivity data to HWC data. Figure 5.5 shows the cumulative distribution of HWC values from the ARC data at 2.7, 4.7, and 6.7 km MSL. The 2.7 km MSL CAPPI level has the largest HWC values and therefore the data at this level were used to estimate P_c(HWC) in Eq. (5.1). The data points at 2.7 km MSL that were ultimately used to derive P(HWC) are shown in Fig. 5.5.

The other term on the right hand side of Eq. (5.2), P_p(HWC), was calculated by estimating the mean annual minutes of hail at a worst case location for hail and then dividing this number by the number of minutes in a year. Equation (5.3) below shows how P_p(HWC) was estimated:

$$P_p(HWC) = n \times T \times k(HWC) / 525960 \qquad (5.3)$$

where n is the number of hail storms at a point representing the worst case location, $\bar{T}$ is the mean point hailfall duration, k(HWC) is a correction factor defined below, and 525960 is the number of minutes in a year.

Figure 5.6 shows the number of point haildays throughout the continental United States (Changnon, 1977). Figure 5.6 can be interpreted as a map showing the number of days each year that hail would fall on a given point. Southeastern Wyoming and the Washington coast show the highest point haildays in the United States at 9 and 10 respectively. Figure 5.7 indicates, however, that the hail on the Washington coast is "light" (i.e. likely consisting of graupel, for the most part, rather than hail as defined herein), whereas the hail that occurs in southeastern Wyoming is severe. For this reason a value of 9 haildays per year was used as the peak value in the U. S. for the purposes of this study. There is a precedent for using the peak value of the U. S. as a worst case value globally (c. f., Gringorten, 1971). Gokhale (1975) shows maps similar to the U. S. hailday map for Africa, Argentina, and India that support a value of 9 as worst case. Similarly, Omoto (1974) shows a hailday map for Japan where a value of 5 haildays annually is the maximum. Sulakvelidze (1967) reports a point hailday maximum of 8-10 days for the Soviet Union. To reiterate, the value of 9 haildays per year in southeastern Wyoming was considered the worst case frequency for the purposes of this study. Furthermore, since hail occurs so infrequently (only 9 days out of 365), it was assumed that only one hailfall per hailday occurs at a given point. In other words, n, from Eq. (5.3), was assigned a value of 9.

Mean hailfall duration at a point can be estimated by dividing the mean hailshaft diameter by the mean hailshaft speed, and applying a correction factor, c. A correction factor is necessary for two reasons. The first reason is that the distance through the hailshaft that passes over the point is not necessarily equal to the diameter because the center of the hailshaft doesn't always pass over the point. The second reason that a correction factor is necessary when calculating the mean duration of hail at a point from the mean hailshaft diameter and speed is that the product of the means is not necessarily the mean of the product, i. e. :

$$\bar{a} \cdot \bar{b} \neq \overline{ab}$$

So the equation to calculate the mean point hail duration, T, is:

$$T = c\, D_h / S \qquad (5.4)$$

where c is the correction factor, D_h is the mean hailshaft diameter, and S is the mean hailshaft speed. The correction factor, c, was calculated using data presented by Changnon (1970) from Illinois. He reported T, D_h, and S, each measured independently, from which c was calculated. He gave a value of T = 3.6 min for daytime storms, S = 30 mi hr^{-1}, and he reported a mean maximum hailstreak width of 1.1 mi which was used in this study as a value for D_h. Using these values and rearranging Eq. (5.4), a value of 1.64 was calculated for c. It was then assumed that the correction factor is applicable world wide. The median hailshaft diameter of the ARC data is 3.15 km. A value of 15 m s^{-1} was used for S, based on a mean South Dakota hailstreak speed reported by Changnon (1970). Using Eq. (5.4), then, with c = 1.64, D_h = 3150 m, and S = 15 m s^{-1}, a value of T = 344 s (about 6 min) was calculated. This value for T is supported by measured values of T at various locations as shown in Table 5.2.

The correction factor in Eq. (5.3), k(HWC), is necessary because it was recognized that the higher HWC values within a hailshaft occupy a smaller cross-sectional area and therefore the duration of larger HWC values at a point will be considerably smaller than the overall hail duration. A simple correction was applied based on an assumed across-shaft HWC distribution. It was assumed that for hailstorms with a peak HWC value $\geq$ 4 g m^{-3}, HWC increases inward from the edges of the shaft such that there is a region within the hailshaft (that has a cross-sectional area with diameter one-third the diameter of the overall shaft) where the peak HWC value occurs uniformly. For hailstorms with peak HWC $\leq$ 2 g m^{-3} it was assumed that the peak value is uniformly distributed across the entire shaft. For hailstorms with peak HWC between 2 and 4 g m^{-3}, the diameter of the inner region where it is assumed that the peak HWC value is uniformly distributed, is linearly interpolated between the value for hailstorms with peak HWC $\leq$ 2 and $\geq$ 4.

In other words, the diameter of the inner region where the peak HWC value is assumed to occur, D_p, is given by:

$$D_p = \begin{cases} D_h & \text{for} \quad HWC_p \le 2 \\ \frac{1}{3} D_h \, (5 - HWC_p) & \text{for} \quad 2 < HWC_p < 4 \\ \frac{1}{3} D_h & \text{for} \quad HWC_p \ge 4 \end{cases}$$

where HWC_p is the peak HWC value within the hailshaft. Figure 5.8 shows across-shaft HWC distributions from both model-generated and natural hailstorms superimposed with the assumed distribution described above.

By substituting D_p for D_h in Eq. (5.4) it becomes clear that k(HWC) is defined by:

$$k(HWC) = \begin{cases} 1 & \text{for} \quad HWC \le 2 \\ \frac{1}{3} \, (5 - HWC) & \text{for} \quad 2 < HWC < 4 \\ \frac{1}{3} & \text{for} \quad HWC \ge 4 \end{cases} \qquad (5.5)$$

Notice that the product $D_h \cdot k(HWC)$ is a function describing the effective diameter of the cross-sectional area of which a given HWC value is equalled or exceeded. $D_h \cdot k(HWC)$ is to hail cells what $D_e(LWC)$ is to rain cells. Figure 5.9 shows a comparison of $D_h \cdot k(HWC)$ and $D_e(LWC)$. For water contents larger than ~10 g m^{-3}, $D_h \cdot k(HWC)$ exceeds $D_e(LWC)$ and therefore it is likely that the estimate of $D_h \cdot k(HWC)$ used in this study is conservative in the sense that extreme HWC values are assumed to occur over a larger region than they actually occur in nature.

With n, T, and k(HWC) defined, Eq. (5.3) can be used to solve for $P_p(HWC)$:

$$P_p(HWC) = \begin{cases} 1 \times 10^{-4} & \text{for} \quad HWC \leq 2 \\ 3.33 \times 10^{-5} \, (5 - HWC) & \text{for} \quad 2 < HWC < 4 \\ 3.33 \times 10^{-5} & \text{for} \quad HWC \geq 4 \end{cases} \qquad (5.6)$$

5.3 Results

With P_p(HWC) and P_c(HWC) known, then Eq. (5.1) was used to solve for P(HWC). The three P_c(HWC) points, indicated in Fig. 5.5, were multiplied by P_p(HWC), then curve fitted. The resulting curve, which is defined by P(HWC) = $1.39 \times 10^{-5} \cdot \exp(-HWC/1.73)$, is shown in Fig. 5.10. At probability levels of 10^{-7}, 10^{-8}, and 10^{-9}, the HWC values are 8.5, 12.5, and 16.5 g m^{-3}, respectively. The highest measured value from the ARC 30-minute data was 9.3 g m^{-3}, which has a corresponding probability of occurrence of 6.4×10^{-8}. All values to the left of ($9.3, 6.4 \times 10^{-8}$) were extrapolated.

Figure 5.11 shows a comparison of the rain and ARC-derived hail curves. As might be expected, P(LWC) exceeds P(HWC) at all probability levels along the abscissa. The two curves tend to converge to the left, which also might be expected since atmospheric conditions favorable for producing extreme rainfall often are also conducive to hail storm formation.

It should be re-emphasized that the curve in Fig. 5.10 represents the probability of hail occurring at a point at a worst case location for hail. P(HWC) does not give the probability of an airplane encountering hail of various intensity. The airplane threat analysis is discussed in Section 9.0.

As discussed previously, the data used to construct the hail curve in Fig. 5.10 were obtained by extracting a maximum reflectivity value for each hail region at evenly spaced intervals of 30 minutes. In addition to the 30-minute data, ARC examined the data at smaller time intervals when a particularly large hail reflectivity value was discovered in the 30-minute data. In other words, if a large reflectivity value was discovered in one of the 30-minute scans, then ARC would examine each scan immediately before and after the scan with the large

reflectivity value. (Recall that each scan took about 3 minutes to complete, so for every scan examined in 30 minute intervals, there are approximately 9 scans that were not examined. These 9 scans, however, were examined when a large reflectivity was discovered in the routine 30 minute data extraction.)

Table 5.3 shows the maximum HWC, calculated from reflectivity using Eq. (5.2), for each CAPPI level of each month of July of the three years of ARC data. The single highest HWC value from the entire data base is 10.9 g m^{-3} from 1985. Parenthetically, the South Dakota School of Mines and Technology T-28 armored research airplane (Johnson and Smith, 1980) recorded an HWC value of 12 g m^{-3} for this same storm during a research project being conducted in Alberta in 1985 (Musil and Smith, 1988).

The T-28 airplane has penetrated thunderstorms in a number of research projects. An HWC value of 14 g m^{-3} in an Alabama thunderstorm was reported by Musil and Smith (1989), but ice particles were rather small and may have been predominantly graupel (Dennis Musil, personal communication). Smith *et al.* (1976) reported a precipitation water concentration of 12 g m^{-3} in a Colorado thunderstorm during the United States National Hail Research Experiment, but there was no mention of whether the precipitation was in the form of hail, rain, or a hail/rain mixture. The T-28 data is valuable because it is collected within clouds, but for safety reasons the airplane does not intentionally fly into regions where a ground-based radar indicates reflectivity values above 55 dBZ. Therefore, it's possible that even higher HWC values could have been measured if the airplane could have safely flown into those regions where reflectivity exceeds 55 dBZ.

An important aspect of the weather threat analysis is the hailstone size distribution. As discussed in Appendix B, the size distribution is usually considered to be exponential as given by Eq. (B.1):

$$N(D) = N_0 e^{-\Lambda D} \qquad \text{for } (D_{min} < D < D_{max})$$

where N_0 and Λ are defined in Section 4.3 and Appendix B. The minimum hailstone diameter, D_{min}, is specified as 5 mm, while the maximum hailstone

diameter, D_{max}, is often considered infinite for calculation purposes. Equation (5.7) below gives HWC:

$$HWC = \frac{1}{6}\rho_H \int_{D_{min}}^{D_{max}} N(D)\, D^3\, dD \qquad (5.7)$$

where ρ_H is the density of the hailstones. Equations (5.8) and (5.9) below, from Ulbrich and Atlas (1982), can be rearranged and combined with Eq. (B.11), also from Ulbrich and Atlas (1982), to give equations for N_0 and Λ as a function of HWC.

$$N_0 = 95.6\, D_0^{0.39} \qquad (5.8)$$

$$HWC = \pi\, \rho_H\, N_0 / \Lambda^4 \qquad (5.9)$$

So, for a given HWC, Eqs. (B1) and (5.7) can be used to estimate the contribution of the total number of hailstones and HWC from selected hailstone size intervals (similar to Fig. 4.12, but for hail). Figure 5.12a shows the hailstone size distribution as calculated from Eq. (B1) with N_0 and Λ calculated by assuming an HWC of 13 g m^{-3} and assuming D_{min} = 5 mm and $D_{max} = \infty$. Approximately 89% of the hailstones are between 0.5 and 1.5 cm. The size category with the most hailstones is $0.5 < D < 1.0$ cm, while the mean stone size is 0.95 cm in diameter. Figure 5.12b shows the percent contribution to the total HWC from each 1 mm size interval as calculated from Eq. (5.7) with HWC = 13 g m^{-3}, D_{min} = 5 mm, $D_{max} = \infty$, and $\rho_H = 9 \times 10^5$ g m^{-3}. Approximately 58% of the total HWC is from stones with diameters between 1.0 and 2.0 cm. The size category contributing the most to the total HWC is $1.0 < D < 1.5$ cm, while the median volume diameter, D_0, is 1.6 cm.

6.0 Hail - GNEFA

This section documents the portion of the weather analysis based on data supplied to CFM International [through the Société National d'Etude et de Construction de Moteurs d'Aviation (SNECMA)] by the Groupement National d'Etudes des Fléaux Atmosphériques (GNEFA). While GNEFA supplied the data, the actual analysis was carried out by CFMI. In Section 6.1, GNEFA data are discussed. In Section 6.2, the methodology used by CFMI to develop a HWC curve, based on GNEFA data, is explained. In Section 6.3, the GNEFA-based curve is presented and discussed.

6.1 GNEFA Data

The Groupement National d'Etudes des Fléaux Atmosphériques, located in Aubiere, France employs some of the world's leading experts on hail and hailstorms. CFMI, through SNECMA, signed a contract with GNEFA in early 1989 to provide a report on the physical characteristics of hailstorms (Husson *et al.*, 1989).

Included in the data provided to CFMI by GNEFA were S-band weather radar data collected in the Napf region of Switzerland (near Zurich) as part of the Grossversuch IV program (Federer *et al.* 1978; Waldvogel *et al.* 1978). The radar operated in a PPI mode at a constant elevation angle of 5.5°, with each PPI scan requiring about one minute to complete. Only data within a range of 30 km from the radar were used.

The radar data consists of a set of 253 Z_{max} values, where Z_{max} is defined as the maximum reflectivity value of a "potential hail-producing" cell (Fig. 6.1). A cell is defined as a potential hail producer if a PPI radar echo contour exceeds 45 dBZ and a hail hazard criterion, measured in range-height indicator (RHI) mode by another radar, is met. All cells which had produced hail at the ground were considered hail producers, but not all cells considered hail producers discharged hail measured at ground level (Waldvogel and Grimm, 1979). The 253 cells providing Z_{max} values make up the complete Grossversuch IV radar-identified cell data of the years 1977-1982.

6.2 Methods of Analysis

Much of the same methodology used to develop the ARC hail curve, as described in Section 5.2, was also used to develop the GNEFA hail curve. Equation (5.1) was used with the term P_p(HWC) replaced by P_p, i. e., the prior probability used was a constant, independent of HWC. Equation (5.2) was used to convert reflectivity to HWC, but only after the reflectivity values were corrected for the effects of hailstone melting below the freezing level.

The most important difference between the Boeing and CFMI methodologies is that a correction factor was applied to the GNEFA reflectivity data. The GNEFA data shown in Fig. 6.1 differs from the ARC data in that ARC values represent maximum reflectivity within a hail cell *at the time it happened to be scanned.* A GNEFA value, on the other hand, represents the *single highest* reflectivity value within a hail cell that occurred *sometime during the life of the cell* (or at least throughout the portion of the cell's life when it was within the range of the radar). This is an important distinction because if Eq. (5.1) is used with P_c(HWC) calculated from the uncorrected GNEFA data, then P(HWC) will <u>not</u> give the probability of a given HWC value occurring at a point *at any random instant.* The reason that it will not is that GNEFA reflectivity values do not represent the conditional probability of maximum reflectivity within a hail cell at any random instant, because only the single highest value in a cell was recorded regardless of when it occurred.

Therefore, CFMI assumed that the storm is made of one or several cells for which the HWC distribution is Gaussian at a given time. This is confirmed by examples shown in Fig. 6.2 and 6.3 where a radar followed the evolution of HWC above a fixed point. CFMI elected to use a $\pm 2\sigma$ volumetric Gaussian distribution to correct the GNEFA values. The HWC values, converted from the GNEFA reflectivity values using Eq. (5.1), were multiplied by a constant correction factor, c = 0.5, to get an "average" HWC (Gashignard and Gires, 1989b).

The term P_c(HWC), defined in Section 5.2, was determined after correcting GNEFA reflectivity values for the effects of water coating on hailstones from melting that had occurred below the freezing level. The correction technique

was identical to that used on the ARC data, except that the value of t used for the GNEFA data differed from that used for the ARC data. GNEFA-supplied radar data was collected with a radar scanning scheme designed to maximize the chances of seeing hailstorms at a level 1 km below the freezing level (Husson *et al.*, 1990). It was assumed for the purpose of correcting for water coating, that the GNEFA data was taken 1 km below the freezing level. The melting model and initial conditions used to correct the ARC data were applied to the GNEFA data, but the modelled hailstone was allowed to fall to 1 km below the freezing level instead of only 0.8 km as was the case for the ARC correction. The resulting water-coating thickness was t = 0.024 cm. The GNEFA reflectivity values were corrected for this effect as described in Appendix 2 except that $dBZ_{t=0.021}$ (the ARC value) was replaced by $dBZ_{t=0.024}$ everywhere. The corrected reflectivity values were then converted to HWC using Eq. (5.2). At this stage the HWC values were multiplied by the constant, c = 0.5, referred to above.

To calculate prior probability, P_p, the following equation was used:

$$P_p = n \times T / 525960 \qquad (6.1)$$

where n and T are defined in Section 5.2. Notice that Eq. (6.1) differs from Eq. (5.3) only in that the factor, k(HWC), was not considered. The Boeing-derived value of six minutes for the point duration, T, was used in Eq. (6.1). The number of storms passing over a point, n, was determined from GNEFA-supplied data. From 300 measurement points in Switzerland, the highest number of hail occurrences at a single point was 18 over a 7 year period (Gashignard and Gires, 1989a). This yields:

$$n = 18 / 7 = 2.57$$

So using Eq. (6.1) with n = 2.57 and T = 6, P_p is equal to 2.93×10^{-5}.

6.3 Results

With P_p and P_c(HWC) known, Eq. (5.1) could then be used to solve for P(HWC). Four values of HWC were used to calculate four P(HWC) points. These four

points were then curve fitted. The resulting curve, defined by P(HWC) = 6.75 x 10^{-6}·exp(-HWC/2.05), is shown in Fig. 6.4. At probability levels of 10^{-7}, 10^{-8}, and 10^{-9} the HWC values are 8.6, 13.4, and 18.1 g m^{-3}, respectively. The largest HWC value of the four fitted points is 10.2 g m^{-3}, which has a corresponding probability of occurrence of 4.7 x 10^{-8}. So all values to the left of (10.2, 4.7 x 10^{-8}) were extrapolated.

7.0 Comparison of Boeing and CFMI Hail Results

Figure 7.1 shows both the Boeing-derived and CFMI-derived hail curves. The two curves cross each other at about $P(8\ g\ m^{-3}) = 1.4 \times 10^{-7}$. The CFMI curve has larger HWC values than the Boeing curve at probabilities less than 1.4×10^{-7}, whereas the Boeing curve has higher HWC values for probabilities greater than 1.4×10^{-7}. In general, though, there is good agreement between the two curves. At a probability level of 10^{-9}, for example, the Boeing HWC is 16.5 g m^{-3} and the CFMI HWC is 18.1 g m^{-3}, a difference of only 1.6 g m^{-3}.

A significant aspect of the weather threat study concerns the vertical distribution of hail in the atmosphere. In particular, as explained in Section 9.0, it is important to identify the level in the atmosphere at which the hail curves in Fig. 7.1 apply. A majority of above-ground-level hail data in the available literature has been collected by weather radar; therefore, altitude distributions have been derived from reflectivity profiles of hailstorms.

Table 7.1 lists a number of different studies in which information on the altitude of maximum reflectivity for hailstorms is given. In each of these references, values given are mean quantities for a number of hailstorms. The altitude of maximum reflectivity ranges from 0.2 to 2.5 km above the freezing level. The data shown in Table 7.1 are consistent with results given by Atlas (1966) in which he describes a "balance level" where precipitation is suspended above the freezing level. In contrast, however, to the results summarized in Table 7.1, are the reflectivity profiles given by Schmid and Waldvogel (1986). Figure 7.2 shows their derived profiles of radar reflectivity. They were obtained with a more general, but complicated, method than the methods used to determine the values given in Table 7.1. Schmid and Waldvogel (1986) argue that their profiles better represent hailstorms throughout their life history. They suggest that earlier reflectivity profiles, such as Donaldson's, are representative for growing and mature hail cells, which possibly miss large, low-altitude reflectivity values in decaying hail cells. The level of maximum reflectivity in Fig. 7.2 appears to be 1 km below the freezing level. Increased radar reflectivity due to melting, however, accounts for the peak at 1 km. In other words, hail water content at the freezing level is greater than at 1 km below, even though radar reflectivity is smaller at the freezing level than at 1 km below.

For this study, the freezing level is considered the altitude of maximum HWC. As discussed in Section 5.2, hail that occurs in the central United States is representative of the most severe and most frequent worldwide. Figure 7.3 shows average freezing level heights in the United States in June, the peak month for hailstorm frequency. Superimposed on the freezing level map is the annual hailday frequency map. The region of the most severe hail (Fig. 5.7) extends southward to the Colorado-New Mexico border. A freezing level height of 15,000 feet appears to be the upper limit within this region of most severe hail. Boeing, therefore, chose 15,000 feet as the level at which maximum HWC occurs. Figure 7.4 shows average freezing level heights over Europe in June. Because the most severe hail in Europe occurs in France and Switzerland, CFMI chose 12,000 feet as the level at which maximum HWC occurs.

ARC data were used to determine the variation of HWC with altitude above the freezing level. As indicated in Fig. 5.5, the probability of a given HWC value decreases with increasing altitude above the freezing level. Stated alternatively, the HWC value at a given probability level decreases with increasing altitude. The rate at which HWC decreases with altitude depends on the probability level of interest. As discussed in Section 9.0, the 10^{-8} probability level on the airplane threat curve (Fig. 9.4) has been selected as the reference value by which to set the hail standard. The ARC HWC value at 10^{-8} probability on the airplane curve is 8.7 g m^{-3}.

To calculate the change in HWC with altitude, ARC cumulative hail probability curves (Fig. 5.5) were examined at the probability level corresponding to 8.7 g m^{-3} on the 2 km AGL curve, i. e., 99.8%. Data shown in Fig. 5.5 were curve fitted and then the 6 km AGL data was extrapolated to 99.8% cumulative probability. As discussed in Section 5.2, the correction for the extra water-coating on hailstones at 2.7 km MSL essentially renders the 2.7 km MSL data equivalent to that at the freezing level, 3.5 km MSL. Therefore, the 2.7 km MSL HWC data was assumed to apply at 3.5 km MSL for the purposes of calculating HWC variation with altitude. In summary, variation of HWC with increasing altitude above the freezing level was calculated from the HWC values at 99.8% cumulative hail probability at 3.5, 4.7, and 6.7 km MSL. This provided three data points, which were subsequently curve-fitted, as indicated in Fig. 7.5 by the

portion of the curve to the right of $H - H_0 = 0$, where H_0 is height above the freezing level.

To calculate the variation of HWC with altitude below the freezing level, the Rasmussen and Heymsfield (1987a) melting model was used. The modeled hailstone was allowed to fall below the freezing level until the critical amount of liquid water, before the onset of water shedding, had been reached. Figure 7.5 shows the variation of normalized HWC as a function of altitude from the freezing level. The portion of the curve to the left of $H - H_0 = 0$ was derived from the Rasmussen and Heymsfield (1987a) melting model as described above.

Figure 7.6 shows a vertical profile, relative to the freezing level, of the 10^{-8} probability HWC from both the Boeing-derived and CFMI-derived airplane threat hail curves (Fig. 9.4). As discussed above, the level at which the maximum HWC is expected to occur is the freezing level. For the Boeing curve, 15,000 feet is considered the freezing level, and for the CFMI curve, 12,000 feet is considered the freezing level. It should be kept in mind that the curves shown in Fig. 7.6 strictly refer to HWC. For example, total water content, including melted hail, below the freezing level can actually exceed that at the freezing level, but only the portion of the water content that is still ice is considered HWC in this analysis.

8.0 HWC ERROR ANALYSIS

8.1 Formulation

8.1.1 The Basic Error Equation

The threat has been defined as (Sec. 3.0, Eq. (3.1))

$$P_j = P_p \cdot P_c \tag{8.1}$$

where P_j, P_p, and P_c are the relevant joint, prior and conditional probabilities discussed in Section 3.0. The differential of Eq.(8.1) (in finite increment form) is the basic error equation,

$$\Delta P_j = P_c \Delta P_p + P_p \Delta P_c \tag{8.2}$$

The expansion of the prior and conditional probability errors in terms of errors in the contributing parameters are presented below.

8.1.2 The Prior Probability Error

The prior probability is given by (cf. Sec. 5.2)

$$P_p = \frac{n \cdot D_h}{S} \cdot k \tag{8.3}$$

with all parameters (n = haildays, D_h = mean hailshaft diameter, S = mean storm translation speed, and k = correction factor discussed in Sec. 5.2) appropriately dimensioned. Then the relative error in prior probability is the logarithmic differential of (8.3),

$$\frac{\Delta P_p}{P_p} = \frac{\Delta n}{n} + \frac{\Delta D_h}{D_h} - \frac{\Delta S}{S} + \frac{\Delta k}{k} \tag{8.4}$$

In our threat definition, n has been defined as the number of haildays in the geographic region where hailstorms are most frequent. We can speak of a climatological range in n, and show thereby a climatological range in threat. If our particular choice n = 9 is in "error," then that error must be considered a subjective error in judgement. The only intrinsic, objective error in n is that which results from "sampling errors" committed during the amassing of the climatological data to determine the average n. This error is inversely proportional to the square root of the sample size -- which, in the case of climatological data for the n-estimate, is huge. Objectively then, once the choice of n has been made, for all practical purposes $\Delta n/n = 0$ regardless of the magnitude of $n>0$ (be it for Cheyenne, Edmonton, Chicago, Lucerne, Switzerland, or where ever).

The impact of sample size on the sampling error can be further used to argue a small $\Delta S/S$ in comparison with $\Delta D_h/D_h$, because the sample size for the S-estimate is large compared with that for D_h. Neglecting $\Delta S/S$ then, the net result is the approximation for the prior probability error

$$\Delta P_p = P_p\left(\frac{\Delta D_h}{D_h} + \frac{\Delta k}{k}\right) \qquad (8.5)$$

The cumulative distribution of equivalent hailshaft diameters as determined from the ARC data is shown in Fig. 8.1. The data for diameters less than about 1 km are suspect, because 1 km is about the resolution cell size of the ARC radar at the nominal radar range at which the cell size data were acquired. For sizes above 1 km there is, by Student's t-test at the 95 percent confidence level (Hahn and Shapiro, 1967), no significant difference between the geometric mean of the measured distribution and that of a log normal distribution with geometric mean 3.2 km and geometric standard deviation 3.0 km. The implication is that $\Delta D_h/D_h$ at the one sigma level is about 0.11. Also, the "error" in k derives primarily from the range in hailstorm translational speeds, say 25 percent. *In toto* the incremental error in prior probability is therefore estimated as

$$\Delta P_p = P_p(0.11 + 0.25) \tag{8.6}$$

8.1.3 The Conditional Probability Error

The conditional exceedance probability is the complement of the cumulative distribution of HWC, Φ(HWC); i.e.,

$$P_c = 1 - \Phi(HWC) \tag{8.7}$$

The P_c error increment is thus

$$\Delta P_c = -\Delta\Phi(HWC) \tag{8.8}$$

or, taking the differential of the right-hand side,

$$\Delta P_c = -\phi(HWC)\Delta(HWC) \tag{8.9}$$

where ϕ(HWC) is the probability density of the HWC distribution; Δ(HWC) is now the error in the HWC estimate.

At this point recall that both the ARC and GNEFA HWC data are values calculated from radar data according to an assumed, functional relationship between HWC and the radar reflectivity factor, Z, expressed in decibels dBZ = 10log(Z); i.e., in general,

$$HWC = g(dBZ) \tag{8.10}$$

The relationship now, between the probability density of the original or measured variate, dBZ, and the transformed or calculated variate, HWC, is

$$\phi(HWC) = f(dBZ)\left|\frac{d(dBZ)}{d(HWC)}\right| \tag{8.11}$$

where the derivative on the right-hand side is the Jacobian of the

transformation. Note from this equation that the cumulative distributions of the two variates are equal,

$$\Phi(HWC) = F(dBZ) \tag{8.12}$$

when Φ(HWC) is evaluated at the HWC given by the dBZ in the F(dBZ) distribution, and vice versa.

Now substitute Eq. (8.11) into Eq. (8.9), with the derivative treated as a ratio of finite increments;

$$\Delta P_c = -f(dBZ)\Delta(dBZ) \tag{8.13}$$

Equation (8.13) thus expresses the error in P_c in terms of the error in the directly measured reflectivity factor. This can be represented as the sum of a bias error, ϵ_B(dBZ), and a stochastic error, δ(dBZ), so that

$$\Delta(dBZ) = \epsilon_B(dBZ) + \delta(dBZ) \tag{8.14}$$

The discussion of each of these errors follows.

8.1.3.1 Bias Error -- The bias error is argued as follows. The radar return from a single hailstone is determined by its size, shape, and composition (solid ice plus water shell). The "backscatter cross section" is the measure of the effectiveness of the return, and is given exactly by the equations of Mie scattering theory (Kerker, 1969). The volume backscatter is determined by summing the individual Mie cross sections over the spectrum of hailstones in the radar resolution cell, i.e., the hailstorm volume illuminated by the radar pulse. This summation over unit volume, which defines the reflectivity, η_r, is expressed as:

$$\eta_r = \int_{0.5}^{D_{max}} \sigma(D)N(D)dD \tag{8.15}$$

where $\sigma(D)$ is the hailstone backscatter cross section (usually cm^2) as a function of hailstone diameter, and N(D) is the hailstone number density (usually number per m^3 per cm size interval); the integration is from the minimum to the maximum hailstone diameter, and the units of η_r are cm^2/m^3.

The reflectivity factor in units mm^6/m^3 is related to η_r by

$$Z = 10^6 \frac{\lambda^4}{\pi^5 |k|^2} \eta_r \qquad (8.16)$$

where λ is the radar radiation wavelength in cm, and $|k|^2 = 0.93$ is the radio refractivity for water (Battan, 1959). This definition of Z is in deference to its similarity to the Rayleigh scattering formula, which indicates $\sigma(D)$ as proportional to the sixth power of the scattering particle diameter.

The numerical evaluation of Eq. (8.16) using Eq. (8.15) is an unwieldy calculation that requires complete knowledge of the hailstone size distribution. Consequently, it is usually avoided in practice through use of an empirical relationship derived from experimental data, that expresses Z in terms of bulk parameters of the hailshaft volume, e.g., HWC (generic Eq. (8.10)).

The Ulbrich and Atlas equation (Eq. (5.10)) is one example of such an empirical relationship. It is the result of a linear least square regression of log Z onto log (HWC), as calculated from Z versus HWC data pairs determined experimentally by Federer and Waldvogel (1975) during the course of a single hailstorm near Lucerne, Switzerland. Solved for HWC, it provides a good basis for estimating HWC from radar data over the range of Z,HWC-values in the data set from which it was derived.

Nevertheless, a better representation of the relationship between Z and HWC --

especially for the high HWC's of interest here, when Mie scattering effects become increasingly complicated -- starts with Eq. (8.16) expressed as

$$Z = 10^6 \frac{\lambda^4}{\pi^5 |k|^2} \int_{0.5}^{D_{max}} \sigma(D) N_0 e^{-\Lambda D} dD \tag{8.17}$$

where

$$N(D) = N_0 \exp(-\Lambda D) \tag{8.18}$$

is the hailstone number density given as an exponential distribution. Empirical equations for the parameters of this distribution in terms of HWC are (Ulbrich and Atlas, 1982)

$$\left.\begin{aligned} N_0 &= 92.3(HWC)^{0.089} && \text{a.)} \\ \Lambda &= 1.30\left(\frac{HWC}{N_0}\right)^{0.25} && \text{b.)} \end{aligned}\right\} \tag{8.19}$$

Use of these equations in Eq. (8.17) provides the alternate relationship between Z and HWC better suited to cases of high HWC.

The dashed curve in Fig. 8.2 is dBZ versus HWC as calculated from Eq. (5.10) expressed in decibels, viz.,

$$dBZ = 59.647 + 12.3\log(HWC) \tag{8.20}$$

The solid curve is from Eq. (8.17), with values for $\sigma(D)$ as given by Battan, *et al.* (1970) for hailstones with 0.02 water shell thickness (cf. Sec. 5.2). The plotted points are from a least square, second order, semi-log curve fit to the solid line,

$$dBZ = 59.95164 + 14.62608\log(HWC) - 1.250366\log^2(HWC) \tag{8.21}$$

The difference between the two curves along the ordinates, i.e., the difference between Eqs. (8.20 and 8.21), is the bias error in Eq. (8.14); i.e.,

$$\epsilon_B(dBZ) = -0.30264 - 2.32608\log(HWC) - 1.250366\log^2(HWC) \qquad (8.22)$$

For dBZ > 59 this is a negative bias, which reflects the inherent conservatism of the Ulbrich and Atlas equation for purposes here. That is, for given dBZ above 59, the HWC inferred from (8.20) is high relative to that from (8.21).

The bias error in P_c is

$$(\Delta P_c)_B = [-0.30264 - 2.32608\log(HWC) - 1.250366\log^2(HWC)]\, f(dBZ) \qquad (8.23)$$

8.1.3.2 Stochastic Error -- The stochastic reflectivity error now, is also made up of two components, viz., a measurement error and a "transformation" error,

$$\delta(dBZ) = \delta(dBZ)_{meas} + \delta(dBZ)_{trans} \qquad (8.24)$$

both of which may be considered zero mean. The measurement error is determined by the accuracy of the radar used for the reflectivity measurements. The stated accuracies for the ARC and GNEFA radars are, "to within two dBZ," and, "to one dBZ," respectively. Assume such accuracy is at the 3.0 sigma level. Therefore, on average at the one 1.0 sigma level, take $\Delta(dBZ)_{meas} = 1.5/3.0 = 0.5$ dBZ. The stochastic error in P_c due to that in the dBZ measurement is thus:

$$(\delta P_c)_{meas} = 0.5\, f(dBZ) \qquad (8.25)$$

The transformation error is that which results from uncertainties in the Z or dBZ versus HWC relationship, ascribable for the most part to storm-to-storm

variations in the make-up of the hailstone size distribution. Therefore, consider the differential of Eq. (8.17),

$$\delta Z = \delta N_o \int_{0.5}^{D_{max}} \sigma(D) e^{-\Lambda D} dD - \delta\Lambda \int_{0.5}^{D_{max}} \sigma(D) D N_o e^{-\Lambda D} dD + \delta D_{max} \left(\sigma(D_{max}) N_o e^{-\Lambda D_{max}} \right) \quad (8.26)$$

where δN_o and $\delta\Lambda$ are incremental errors in the parameters of the hailstone size distribution, and δD_{max} is the error in the specification of the maximum hailstone size. Cheng and English (1983) derived the following equation for N_o in terms of Λ

$$\log N_o = A + B \cdot \log \Lambda \quad (8.27)$$

This again is the result of a linear least square regression between experimentally determined $\log(N_o)$ and $\log(\Lambda)$ data pairs. The differential of Eq. (8.27) expresses the relative error in N_o in terms of that in Λ, i.e.,

$$\frac{\delta N_o}{N_o} = B \frac{\delta\Lambda}{\Lambda} \quad (8.28)$$

Note that this relation depends only on the slope, and not on the intercept of the N_o,Λ regression equation. Although the intercept does appear to differ on average in the regression equations derived for European as opposed to North American hailstorms, the slope shows no significant variation about a mean value B≈3.9 (Cheng and English, 1983). Therefore, Eq. (8.28) with B=3.9 may be considered valid worldwide. Then treating the D under the integral of the second term on the right-hand side of Eq. (8.25) as a constant at the median

hailstone volume diameter D_0, the first two terms on the right-hand side combine and the equation can be rewritten as

$$\frac{\delta Z}{Z} = 0.2303 \cdot \delta(\mathrm{dBZ}) = \left(3.9 - \Lambda D_0\right)\frac{\delta\Lambda}{\Lambda} + \frac{\sigma(D_{max})\,N_0 e^{-\Lambda D_{max}}}{Z}\,\delta D_{max} \qquad (8.29)$$

The second term on the right-hand side is small compared to the first and may be neglected. Thus, using the data of Ulbrich and Atlas (1982) to approximate $\Delta\Lambda/\Lambda = 0.4$ at the one sigma level, and using their asymptotic value $\Lambda D_0 = 3.672$ as appropriate in cases of high HWC, the stochastic error in P_c resulting from the transformation error can be estimated from

$$(\delta P_c)_{trans} = 0.4\ f(\mathrm{dBZ}) \qquad (8.30)$$

8.2 Evaluation

8.2.1 The Probability Density

What remains to complete the error analysis is an expression for the probability density of the experimental dBZ values. Shown in Fig. 8.3 are the cumulative distributions of dBZ as determined from both the ARC and GNEFA experiments. The figure emphasizes that these data are not directly comparable, because of the inherently different natures of the two experiments (cf. Sec. 6.2). That is, experimental procedures were such that data from the ARC experiment represent the usual random sample drawn from some "initial" population; those from the GNEFA experiments are the extreme values drawn from subsets of data from that initial population.

The two cumulative distributions therefore compare only the extreme dBZ-value. Little information about the initial distribution is available from that of the extreme values. What can be said, however, is that in the asymptotic approach to the extreme, the extreme value distribution is displaced upward relative to the random sample distribution (higher dBZ for given cumulative probability) by

an amount proportional the natural logarithm of the sample size (253 for the GNEFA data); and retains the shape of the initial population or sample distribution to greater or lesser degree, depending on the actual way in which the asymptotic approach to the extreme value is accomplished (cf. Gumbel, 1958, Chapter 5, for a complete discussion). This is precisely the behavior depicted in Fig. 8.3.

The ARC sample distribution is thus taken as the representation of the initial or population distribution. Accordingly, this distribution is replotted in Fig. 8.4, superimposed on a curve of the cumulative beta distribution,

$$F(x;\gamma,\eta)=\begin{cases}0, & x<0\\ \dfrac{\Gamma(\gamma+\eta)}{\Gamma(\gamma)\Gamma(\eta)}\displaystyle\int_0^x t^{\gamma-1}(1-t)^{\eta-1}dt, & 0\le x\le 1\\ 1, & x>1\end{cases} \qquad (8.31)$$

with distribution parameters η and γ, and transformed variate t, given by

$$\gamma = 1.5491$$

$$\eta = 4.6872$$

$$t=\frac{(dBZ-40.54)}{(82.54-40.54)}$$

and where Γ denotes the complete gamma function. The distribution parameters were estimated from the sample mean and standard deviation of the ARC data as described by Hahn and Shapiro (1967). The beta distribution was selected to represent the initial distribution because the shape parameters η and γ allow for a variety of distribution shapes; and because it is bounded at the upper as well as the lower end. Therefore it is a more realistic basis for extrapolating probabilities beyond the observed data than would be a distribution unbounded to the right (e.g., a log normal distribution), in that it effectively "aims" the extrapolation to some specified "maximum possible" HWC (there is a physical upper limit to the HWC Mother Nature can produce).

This "aiming" is accomplished through the definition of the reduced variate, t; i.e., the denominator in this definition is the difference between the presumed

maximum dBZ value (82.54 dBZ), and the minimum value observed (40.54 dBZ). From Eq. (8.21), a dBZ of 82 implies an HWC of about 60 g/m^3. This is about the LWC associated with the world record one-minute rainfall rate as observed at Unionville, MD (cf. Sec. 5.3). Specifying this for maximum HWC thus acknowledges some remote possibility for the occurrence of all this condensate in the frozen rather than the liquid state.

The modified Kolmogoroff-Smirnov (K-S) maximum deviation test (Crutcher, 1975) is appropriate for testing whether a set of observations are from some completely specified distribution. The test statistic is calculated from

$$K = | F_o(dBZ) - F_n(dBZ) |_{max} \qquad (8.32)$$

where the absolute value is of the maximum difference between the postulated and the sample distributions, $F_o(dBZ)$ and $F_n(dBZ)$, respectively. The subscript n is used to indicate that the sample statistic is a function of sample size. Tables of K for a range of sample sizes are available for determining via the null hypothesis, whether $F_n(dBZ)$ lies entirely within the band $F_o(dBZ)$ +/- K at *a priori* probability 1 - α, where α is a specified confidence level.

To apply the test here, the K-table for the gamma distribution with scale parameter equal to 4 was used because there is no such table available for the beta distribution per se (Crutcher, 1975). However, the shape of the gamma distribution in this case is close to that of the beta distribution given by Eq.(8.31). Therefore, it was felt that this approach would minimize the risk of not rejecting models when they should be when using the non-parametric K-S test on parameterized data (Crutcher, 1975). With this rationale, application of the test indicates there is no significant difference between the observed and assumed distributions at the 95 percent confidence level.

In light of the above then, the beta distribution is considered a valid representation of F(dBZ); the associated probability density function is

$$f(x;\gamma,\eta)=\begin{cases}\dfrac{1}{(82.54-40.54)}\cdot\dfrac{\Gamma(\gamma+\eta)}{\Gamma(\gamma)\,\Gamma(\eta)}\,t^{\gamma-1}(1-t)^{\eta-1}, & 40.54\le x\le 82.54\\ 0, \quad \text{elsewhere}\end{cases} \tag{8.33}$$

8.2.2 The Joint Probability Error

The individual stochastic error components discussed above are uncorrelated. Therefore, their root mean square value is the square root of the sum of the squares of the individual error components as given in Eqs. (8.6), (8.25), and (8.30). Plus and minus three times this value, added to the bias error as stated by Eq. (8.23), gives about the three sigma joint probability error band,

$$\Delta P_j = P_j\left\{\begin{array}{c}-.30264-2.32608\log(HWC)+1.250366\log^2(HWC)\\ \pm\dfrac{3\left[0.11^2+0.25^2+0.5^2+0.4^2\right]^{1/2}}{[1-F(dBZ)]}\end{array}\right\} f(dBZ) \tag{8.34}$$

The originally presented HWC joint probability curve, plus the error band developed from Eq. (8.34) is shown in Fig. 8.5. The offset of the error band is due to the bias error; the width of the band is determined by the stochastic errors. Note again the conservatism of the original curve; conservative in the sense that the original curve is at about the + 3-sigma level (99.9 percentile) of the error band relative to the adjusted curve (plotted solid points).

9.0 Airplane Threat Analysis

9.1 Introduction

Previous sections discussed rain and hail concentrations occurring at a point for an instant of time. The airplane threat analysis evaluates the conditional probability of an airplane spending a finite period of time during an extreme rain or hail encounter. This conditional probability will be called the duration probability P_t. The duration probability accounts for the transient nature of airplane encounters with extreme concentrations of rain or hail. The duration probability is also necessary to establish a correlation between rain and hail threat levels and engine test requirements.

The horizontal extent of extreme rain concentrations is large relative to hail. Because of this size difference, the duration probability of rain is assumed to be 1.0. The following analysis evaluates the duration probability of hail encounters.

9.2 Assumptions

The duration probability analysis is based on the following assumptions:

1) Hailshafts are circular, that is, there is no preferred direction or orientation relative to airplane path.
2) The airplane enters the hailshaft at its perimeter.
3) The airplane passes through the hailshaft in level flight.
4) Hailshafts are stationary relative to airplane motion.
5) The HWC distribution through the hailshaft is uniform.
6) The airplane passes through the hailshaft along a straight line.
7) The duration probability is independent of HWC.

The above assumptions simplify the analysis and provide a conservative estimate of the duration probability.

9.3 Definitions

Figure 9.1 shows the geometry imposed by the above assumptions. The diameter of the hailshaft is D_h. The angle of the airplane path relative to the hailshaft is θ. The distance across the hailshaft at angle θ is L. Flight path length, that is, the distance traveled over the duration period, is λ.

Figure 9.2 shows the relative frequency distribution of equivalent hailshaft diameters derived from data provided by ARC and GNEFA. The relative frequency distribution is the number of hailshaft measurements in each diameter interval divided by the total number of hailshaft measurements. The ARC frequency distribution was derived from dual-polarization radar measurements as discussed in Section 5.0. The GNEFA frequency distribution was obtained from hailpad measurements.

The following analysis uses the GNEFA hailshaft diameter frequency distribution. The GNEFA data was chosen because it better characterized the hailshafts in the diameter range of interest, 10,000 feet and above.

9.4 Formulation

The first step in calculating the duration probability is to determine the airplane flight path length λ. Flight path length is the product of true airspeed and duration time. The airspeed and duration time used in the following example calculation are representative values for large commercial airplanes. A typical airspeed for a large commercial airplane penetrating inclement weather is 280 Knots Indicated Airspeed (KIAS). True airspeed can be calculated from indicated airspeed, altitude and ambient temperature. The altitude and ambient temperature for this calculation were chosen as 15,000 feet above mean sea level (MSL) and 0°C. These conditions correspond to the altitude and ambient temperature of the maximum HWC in a North American hailshaft. Under these conditions, 280 KIAS corresponds to a true airspeed of 603 ft/sec. Flight crews who have flown large commercial airplanes through extreme hail conditions have reported that the encounter lasted about 30 seconds. The flight path length for a 30 second duration at 603 ft/sec is 18,090 feet.

The second step is to relate distance across the hailshaft to hailshaft diameter D_h and flight path angle θ. (Refer to Fig. 9.1.) The distance across the hailshaft at angle θ can be written:

$$L = D_h * \sin\theta \tag{9.1}$$

The third step is to evaluate the duration probability in terms of the above geometrical considerations. The probability that L is greater than λ at a given hailshaft diameter can be written $P\{L>\lambda, D_h=\xi\}$. This expression can be rewritten as the conditional probability that $L>\lambda$, with the condition that $D_h=\xi$, multiplied by the probability that $D_h=\xi$.

$$P\{L>\lambda, D_h=\xi\} = P\{L>\lambda \mid D_h=\xi\} * P\{D_h=\xi\} \tag{9.2}$$

Equation (9.2) can be further modified by substituting Eq. (9.1) for L and rearranging the terms to give:

$$P\{L>\lambda, D_h=\xi\} = P\{\theta>\arcsin(\lambda/D_h) | D_h=\xi\} * P\{D_h=\xi\} \tag{9.3}$$

The term $\theta>\arcsin(\lambda/D_h)$ in Eq. (9.3) can be interpreted as the angle in which L is greater than the flight path length λ. In other words, if the flight path angle is θ or greater, a hailshaft will encompass the airplane flight path. For a given flight path length and hailshaft diameter, the ratio of angles in which L exceeds λ is $(\pi/2 - \theta)/(\pi/2)$. Although the geometry was developed for angles from zero to $\pi/2$, this ratio also applies to angles from zero to π.

The probability that the line segment L exceeds the flight path length λ, for a given hailshaft diameter, can be written:

$$P\{\theta>\arcsin(\lambda/D_h) | D_h=\xi\} = (\pi/2 - \arcsin(\lambda/\xi))/(\pi/2) \tag{9.4}$$

Substituting Eq. (9.4) into (9.3) gives:

$$P\{L>\lambda, D_h=\xi\} = [(\pi/2 - \arcsin(\lambda/\xi))/(\pi/2)] * P\{D_h=\xi\} \tag{9.5}$$

The term $P\{D_h=\xi\}$ can be expressed as the frequency distribution of hailshaft diameters from Fig. 9.2.

$$P\{D_h=\xi\} = f_D(\xi) \tag{9.6}$$

The final step is to consider the duration probability over the relevant range of hailshaft diameters and flight path lengths. The duration probability for all hailshaft diameters greater than the flight path length is determined by substituting Eq. (9.6) into (9.5) and integrating from λ to infinity.

$$P_t = P\{L > \lambda\} = \int_{\lambda}^{\infty}[(\pi/2 - \arcsin(\lambda/\xi))/(\pi/2)]^* f_D(\xi)\, d\xi \tag{9.7}$$

9.5 Results

Figure 9.3 shows the results of numerically integrating Eq. (9.7) for flight path lengths up to 36,000 feet. Given a flight path length, λ = 18090 ft, the duration probability is 0.10. In other words, given the condition that an airplane is traveling 603 ft/sec and has encountered a hailshaft, there is a 0.10 probability that the airplane will spend 30 seconds or more in the hailshaft.

Under the assumption that duration probability is independent of HWC, the threat to an airplane can be written as the product of P_j (from Fig. 7.1) and P_t (from Fig. 9.3).

$$P = P_j{}^*P_t \tag{9.8}$$

The curves shown in Fig. 7.1 can be factored to account for a given P_t. The P_t for the example condition (15,000 ft, 280 KIAS and 0°C T_{amb}) is 0.10. The airplane threat curves are obtained by multiplying the abscissa in Fig. 7.1 by 0.10. Airplane threat curves for the example condition are shown in Fig. 9.4. Equations given in Sections 5.0 and 6.0 can be modified to calculate the HWC for other values of P_t:

$$\text{BOEING:} \quad HWC = -1.73^*\ln[(P)/(P_t{}^*1.39^*10^{-5})] \tag{9.9}$$

CFMI: $HWC = -2.05*\ln[(P)/(P_t*6.75*10^{-6})]$ (9.10)

Where P is the over-all threat probability, and P_t is the duration probability. The following example summarizes the calculation of the HWC at an over-all threat probability of 10^{-8} for an aircraft traveling 180 KIAS:

1) True airspeed at 180 KIAS, 15,000 ft and 0°C is 378 ft/sec.
2) Flight path length for a 30-second duration is 11,340 ft.
3) Duration probability from Fig. 9.3 is 0.26.
4) At an over-all probability of 10^{-8}, the HWC calculated from Eq. (9.9) is 10.2 g/m^3.

9.6 Conclusions

The airplane threat analysis discussed in this section provides a means of estimating the conditional probability that the airplane will remain in rain or hail for a given period of time. This conditional probability has been called duration probability P_t. For extreme **rain**, P_t was chosen as 1.0. For extreme **hail**, P_t can be determined from the curve shown in Fig. 9.3.

10.0 SDSMT Storm Simulations

The Institute of Atmospheric Sciences (IAS) at the South Dakota School of Mines and Technology (SDSMT), located in Rapid City, South Dakota, is an internationally recognized leader in the field of hailstorm research. Over the last several years IAS has developed and refined a number of models that numerically simulate convective clouds, including hail-producing clouds. In February, 1989, Mr. William Tank of Boeing visited IAS, at which time he was briefed on the modelling work being conducted at IAS and shown sample model output. Shortly thereafter a contract was negotiated between IAS and Boeing calling for IAS to simulate specific convective cloud cases associated with the 24 May 1988 and 26 July 1988 engine flameout events near New Orleans, Louisiana and Philadelphia, Pennsylvania respectively (Farley *et al.*, 1989). Subsequent contracts were negotiated to simulate the cloud cases associated with the 29 September 1989 engine flameout over the Adriatic Sea (Farley *et al.*, 1990a), and the 15-16 August 1989 hail encounter near Phoenix, Arizona (Farley *et al.*, 1990b).

All of these cases were simulated using a two-dimensional, time-dependent, cloud model. Atmospheric wind, potential temperature, water vapor, cloud liquid, cloud ice, rain, snow, and graupel/hail (in the form of ice pellets, frozen rain, graupel, and small hail) are the main dependent variables. The model that was used for the Boeing simulations employed bulk water parameterization techniques for the microphysics. Refer to Farley *et al.* (1989) for a full description of the model. Boeing supplied the rawinsonde sounding data and other appropriate meteorological data necessary for model initialization in each case.

Several model runs were carried out for each of the four simulations using various assumptions concerning autoconversion threshold, mesoscale convergence, homogeneous freezing temperature, and surface temperature (Farley *et al.*, 1989, 1990a, b). In addition, the atmospheric soundings from different times and nearby locations were combined in various ways in an attempt to best represent the conditions at the time of the incidents. The input parameters were varied in this way to test for model sensitivity, allowing IAS to determine the input parameters that need to be examined carefully. For each

simulation, IAS indicated the model run(s) that they felt best represented the incident storm.

10.1 New Orleans

Table 10.1 summarizes the results of the various model runs conducted by IAS for the New Orleans flameout incident. The case highlighted by bold type, model run BOE1 A02, is the run that IAS feels best represents storms that might have developed at the time of the incident. The maximum HWC that had occurred during the BOE1 A02 run was 4.66 g m^{-3}. It is unknown whether or not this was the HWC that the airplane actually encountered. It is simply the maximum value produced in a simulated storm using the most representative initial conditions for the time at which the incident occurred, as subjectively determined by the experts at IAS. The very high HWC values of some of the runs are the result of model-sensitivity testing with initial conditions that are not necessarily indicative of the actual pre-storm environment. The simulations for the New Orleans case are discussed in detail by Farley *et al.* (1989).

10.2 Philadelphia

Table 10.2 shows the results of the IAS model runs for the Philadelphia flameout incident. The bold-type highlighted model run, BOE2 B01, is the simulation that IAS has determined as the run most representative of storms that might have developed at the time of the incident. The maximum HWC that had occurred during this run was 3.1 g m^{-3}. As discussed in Section 10.1, this value does not necessarily indicate the concentration of HWC that the airplane encountered. A comparison of Tables 10.1 and 10.2 seems to indicate, however, that the New Orleans simulations produced higher HWC values than the Philadelphia simulations, on average. The Philadelphia simulations are discussed further by Farley *et al.* (1989).

10.3 Adriatic

Several model runs were carried out by IAS for the flameout incident that occurred over the Adriatic Sea. Figure 10.1 shows the results of the three simulations judged by IAS to be the most representative of storms that might

have developed in the vicinity of the incident (IAS makes no mention of which of the three runs they consider as the most representative). Figure 10.1 shows that the HWC maxima of runs BBIF01, BBIF02, and BBIF03 are ~5.2 g m^{-3}, ~10 g m^{-3}, and ~9.5 g m^{-3}, respectively. The model simulations of the Adriatic incident are discussed in detail by Farley *et al.* (1990a).

10.4 Phoenix

Figure 10.2 shows the results of three model simulations of the Phoenix hail encounter incident. The results of model run BOE4A2 (Fig. 10.2b) are considered by IAS as most representative of storms that may have developed in the vicinity of Phoenix at the time of the incident. The maximum HWC of run BOE4A2 was ~5.1 g m^{-3}. The Phoenix simulations are discussed further by Farley *et al.* (1990b).

11.0 Conclusions

In this study an attempt was made to assign probability levels to various LWC (rain) and HWC (hail) values. Figures 4.9 and 7.1, the rain and hail curves respectively, show the main results of the study. These curves were developed such that they could be considered to apply over a point at the worst case world-wide locations for rain and hail (the CFMI hail curve was developed such that it could be considered to apply at a worst case location in Europe).

These curves are the starting point for determining the threat to an airplane. The PC 338-1 committee recommended evaluating the airplane threat at 10^{-8} probability per flight. Figure 9.4 shows the probability of an airplane encountering a range of HWC values for 30-second duration assuming an indicated airspeed of 280 knots at 0°C. The CFMI-derived HWC value corresponding to 10^{-8} probability is 9.1 g m^{-3}. This value is considered to apply at 12,000 feet MSL. The Boeing-derived HWC value corresponding to 10^{-8} probability is 8.7 g m^{-3}. This value is considered to apply at 15,000 feet MSL. Taking air density into consideration, 8.7 g m^{-3} at 15,000 feet MSL corresponds to a water-to-air ratio of 1.2%. It was assumed that the rain curve in Fig. 4.9 could be directly applied to an airplane. This is equivalent to assuming that the conditional probability, given that an airplane encounters rain, of the encounter lasting for at least 30 seconds is 100% (i.e., $P_t = 1$). The LWC value at 10^{-8} probability is 19 g m^{-3}. This value is considered to apply at 19,700 feet. The corresponding water-to-air ratio is 2.9%.

Figure 11.1 is a synthesis of the most pertinent plots from this document. Figures 11.1 a.) and b.) show the worst-case-location curves of probability versus LWC and HWC respectively. Figures 11.1 c.) and d.) show the vertical distribution of rain and hail water contents. Figures 11.1 e.) and f.) show raindrop and hailstone size distributions. Figure 11.1 g.) shows rain and hail cell diameter versus water content. Finally, Fig. 11.1 h.) shows the Boeing- and CFMI-derived curves for airplane parameters of 280 KIAS, 0°C, and 30-second duration.

The Institute of Atmospheric Sciences at the South Dakota School of Mines and Technology simulated four storms associated with airplane hail encounters,

three of which resulted in engine powerloss. The HWC values they considered as most representative of the actual storms that may have formed on the days for which the incidents occurred ranged from 3.1 to 10 g m^{-3}.

Bibliography

Alberta Research Council, 1990: Boeing Hail Study.

Atlas, D., 1966: The balance level in convective storms. *J. Atmos. Sci.*, **23**, 635-651.

Aydin, K., T. A. Seliga, and V. Balaji, 1986: Remote sensing of hail with a dual linear polarization radar. *J. Climate Appl. Meteor.*, **25**, 1475-1484.

Battan, L. J., 1973: *Radar Observations of the Atmosphere.* The University of Chicago Press, 324 pp.

_____, S. R. Browning, and B. M. Herman, 1970: Tables of the radar cross-sections of dry and wet ice spheres. *Tech. Rep. 21*, Institute of Atmospheric Physics, University of Arizona, 11 pp.

Bodtmann, W. F. and C. L. Ruthroff, 1976: The measurement of 1 min rain rates from weighing raingage recordings. *J. Appl. Meteor.*, **15**, 1160-1166.

Briggs, J., 1972: Probabilities of aircraft encounters with heavy rain. *Meteor. Mag.*, **101**, pp. 8-13.

Changnon, S. A., Jr., 1970: Hailstreaks. *J. Atmos. Sci.*, **27**, 109-125.

_____, 1977: The scales of hail. *J. Appl. Meteor.*, **16**, 626-648.

Cheng, L. and M. English, 1983: A relationship between hailstone concentration and size. *J. Atmos. Sci.*, **40**, 204-213.

Crutcher, H. L., 1975: A note on the possible misuse of the Kolmogorov-Smirnov test. *J. Appl. Meteor.*, **14**, 1600-1603.

Dennis, A. S., C. A. Schock and A. Koscielski, 1970: Characteristics of hailstorms of western South Dakota. *J. Appl. Meteor.*, **9**, 127-135.

Department of Defense, 1987: *Military Standard, Climatic Information to Determine Design and Test Requirements for Military Systems and Equipment*, MIL-STD-210C, 9 January 1987, Office of the Under Secretary of Defense, Research and Engineering, Washington, D. C.

Department of Transportation, 1974: Federal Aviation Regulations. Part 33. Airworthiness Standards: Aircraft Engines.

Donaldson, R. J., 1961: Radar reflectivity profiles in thunderstorms. *J. Appl. Meteor.*, **18**, 292-305.

East, T. W. R. and B. V. Dore, 1957: An electronic constant-altitude display. *Proc. Sixth Wea. Radar Conf.*, Amer. Meteor. Soc., 325-330.

Farley, R. D., 1987: Numerical modeling of hailstorms and hailstone growth. Part III: Simulation of an Alberta hailstorm—Natural and seeded cases. *J. Climate Appl. Meteor.*, **26**, 789-812.

_____, F. J. Kopp, and H. D. Orville, 1989: Numerical simulation of thunderstorms responsible for jet engine flameouts. Report SDSMT/IAS/R-89/04, Institute of Atmospheric Sciences, S. D. School of Mines and Technology, Rapid City, SD. 41 pp.

_____, H. D. Orville, and F. J. Kopp, 1990a: Numerical simulation of the thunderstorm associated with the jet engine flameout over the Adriatic Sea. Report SDSMT/IAS/R-90/03, Institute of Atmospheric Sciences, S. D. School of Mines and Technology, Rapid City, SD. 20 pp.

_____, _____, and _____, 1990b: Numerical simulations of the Phoenix hailstorm of 15-16 August 1989. Report SDSMT/IAS/R-90/06, Institute of Atmospheric Sciences, S. D. School of Mines and Technology, Rapid City, SD. 20 pp.

Federer, B. and A. Waldvogel, 1975: Hail and raindrop size distributions from a Swiss multicell storm. *J. Appl. Meteor.*, **14**, 91-97.

_____, _____, W. Schmid, F Hampel, E. Rosini, D. Vento, P. Admirat and J. F. Mezeix, 1978: Plan for the Swiss randomized hail-suppression experiment. Design of Grossversuch IV. *Pure and Appl. Geophys.*, **117**, 548-571.

Foote, G. B., and C. A. Knight, Eds., 1977: Hail: A Review of Hail Science and Hail Suppression. *Meteorological Monograph*, American Meteorology Society, Boston, 277 pp.

Gashignard, E. and P. E. Gires, 1989a: Natural Hail Threat: Proposed CFMI Approach. CFMI presentation to Boeing, November 1989, 20 pp.

_____, and _____, 1989b: Hail Studies. Part I: Studies Conducted by GNEFA. Part II: CFMI Approach to Hail Threat. CFMI presentation, December 14, 1989, 44 pp.

Gokhale, N. R., 1975: *Hailstorms and Hailstone Growth.* State University of New York Press, Albany, New York, 465 pp.

Gringorten, I. I., 1971: *Hailstone Extremes for Design.* AFCRL-72-0081, 23 pp.

Gumbel, 1958: *Statistics of Extremes.* Columbia University Press, New York, 375 pp.

Hahn, G. J. and S. S. Shapiro, 1967: *Statistical Models in Engineering.* John Wiley and Sons, Inc., New York, 355 pp.

Herman, B. M. and L. J. Battan, 1961: Calculations of Mie back-scattering from melting ice spheres. *J. of Meteor.*, **18**, 468-478.

Huschke, R. E., Ed., 1959: *Glossary of Meteorology.* American Meteorological Society, Boston, MA, 638 pp.

Husson, D., J. P. Cammas, H. Izzaoui, S. Laudet, D. Ramond, and J. F. Mezeix, 1989: Estimation de la Concentration de Grele Dans les Precipitations Orageuses. Final Report for S.N.E.C.M.A. / G.N.E.F.A. Contract. Aubiere, France.

Johnson, G. N. and P. L. Smith, 1980: Meteorological instrumentation system on the T-28 thunderstorm research aircraft. *Bull. Amer. Meteor. Soc.*, 61, 972-979.

Jones, D. M. A., 1956: Rainfall drop-size distribution and radar reflectivity. Res. Rept. no. 6. Urbana: Meteor. Lab., Illinois State Water Survey.

_____, and W. M. Wendland, 1984: Some statistics of instantaneous precipitation. *J. Climate Appl. Meteor.*, **24**, 1059-1067.

Jursa, A. S., Ed., 1985: *Handbook of Geophysics and Space Environment.* Published by the Air Force Geophysics Laboratory. [ADA 167000.]

Kerker, M., 1969: *The Scattering of Light and Other Electromagnetic Radiation.* Academic Press, New York, 666 pp.

Konrad, T. G., 1978: Statistical models of summer rainshowers derived from fine-scale radar observations. *J. Appl. Meteor.*, **17**, 171-188.

Kyle, T. G. and W. R. Sand, 1973: Water content in convective storm clouds. *Science*, **180**, 1274-1276.

Macklin, W. C. and I. H. Bailey, 1968: The collection efficiencies of hailstones. *Quart. J. Roy. Meteor. Soc.*, **94**, 393-396.

Marshall, J. S., 1957: The constant-altitude presentation of radar weather patterns. *Proc. Sixth Wea. Radar Conf.*, Amer. Meteor. Soc., 321-324.

_____, and W. M. K. Palmer, 1948: The distribution of raindrops with size. *J. Meteor.*, **5**, 165-166.

Mueller, E. A., and A. L. Sims, 1966: Investigation of the Quantitative Determination of Point and Areal Precipitation by Radar Echo

Measurements. Tech. Rep. ECOM-00032-F, Contract DA-28-043 AMC-00032 (E) Illinois State Water Survey, Urbana, 88 pp. [AD 645218.]

Musil, D. J. and P. L. Smith, 1988: Hail growth processes in an Alberta hailstorm. *J. Wea. Mod.*, **21**, 65-72.

_____, and _____, 1989: Interior characteristics at mid-levels of thunderstorms in the southeastern United States. *Atmos. Res.*, **24**, 149-167.

Omoto, Y., 1974: Hailstorms in Japan. World Meteorological Society, Geneva, WMO 339, 207-215.

Rasmussen, R., and A. J. Heymsfield, 1987a: Melting and shedding of graupel and hail. Part I: Model physics. *J. Atmos. Sci.*, **44**, 2754-2763.

_____, and _____, 1987b: Melting and shedding of graupel and hail. Part II: Sensitivity study. *J. Atmos. Sci.*, **44**, 2764-2782.

Riordan, P. and P. G. Bourget, 1985: *World Weather Extremes.* ETL-0416, 77 pp.

Roys, G. P. and E. Kessler, 1966: Measurements by aircraft of condensed water in Great Plains thunderstorms. National Severe Storms Project Rep. No. 19, Washington, D. C.

Schmid, W. and A. Waldvogel, 1986: Radar hail profiles in Switzerland. *J. Climate Appl. Meteor.*, **25**, 1002-1011.

Smith, P. L., D. J. Musil, S. F. Weber, J. F. Spahn, G. N. Johnson, and W. R. Sand, 1976: Raindrop and hailstone size distributions inside hailstorms. *Preprint Int. Cloud Physics Conf.*, Boulder, Amer. Meteor. Soc., 252-257.

Sulakvelidze, G. K., 1967: *Rainstorms and Hail*, Gidromet., Leningrad. [Translated Israel Program for Scientific Translations, Jerusalem, 1969.]

Tattelman, P., and D. D. Grantham, 1983a: *Northern Hemisphere Atlas of 1-Minute Rainfall Rates.* AFGL-TR-83-0267, 81 pp. [ADA145411.]

_____, and _____, 1983b: *Southern Hemisphere Atlas of 1-Minute Rainfall Rates.* AFGL-TR-83-0285, 81 pp. [ADA145421.]

_____, and K. P. Larson, 1989: *Effects of Rain Attenuation on Satellite EHF Communications in the United States.* AFGL-TR-89-0012.

_____, and P. T. Willis, 1985: *Model Vertical Profiles of Extreme Rainfall Rate, Liquid Water Content, and Drop-Size Distribution.* AFGL-TR-85-0200, 34 pp.

———, and D. Atlas, 1982: Hail parameter relations: A comprehensive digest. *J. Appl. Meteor.*, **21**, 22-43.

Waldvogel, A., B. Federer, W. Schmid, and J. F. Mezeix, 1978: The kinetic energy of hailfalls. Part II: Radar and hailpads. *J. Appl. Meteor.*, **17**, 1680-1693.

Wilk, K. E., 1961: Radar investigations of Illinois hailstorms. Sci. Rep. 1, USAF 19(604)-4940, Ill. State Water Survey, 42 pp.

Willis, P. T., 1984: Functional fits to some observed drop size distributions and parameterizations of rain. *J. Atmos. Sci.*, 41, 1648-1661.

Appendix A: Raincell Diameter as a Function of LWC

Equation A.1 below, derived from radar reflectivity data (Konrad, 1978), provides a framework for establishing D(LWC).

$$Z_p(dBZ) - Z_c(dBZ) = -b\ A_c^{1/2} \qquad (A.1)$$

In Eq. A.1, $Z_p(dBZ)$ is the core radar reflectivity (i. e., peak reflectivity) at a given altitude, $Z_c(dBZ)$ is some contour value (smaller than Z_p) about $Z_p(dBZ)$, b is a constant, and A_c is the area enclosed by the $Z_c(dBZ)$ contour. The "constant", b, has units of dBZ/km and is dependant on $Z_p(dBZ)$ as indicated in Fig. A.1.

The average area of a region where a given reflectivity level is equalled or exceeded can be determined for a range of reflectivities if the core reflectivity frequency distribution is known. Once the reflectivity areas are known, it is a trivial exercise to convert them to LWC areas. The Donaldson (1961) frequency distribution of core reflectivity of New England rain-producing thunderstorms was used, along with the Roys and Kessler (1966) frequency distribution of Oklahoma thunderstorms. The Donaldson (1961) data were converted to LWC using a Z-M equation derived by eliminating R, by substitution, from the Jones (1956) Z-R and M-R equations.

This method gives the average area in which a given LWC value is equalled or exceeded, A(LWC); from which D(LWC) is easily calculated. In addition to obtaining D(LWC) data points using the method outlined above, Briggs (1972) gave direct values of rain rate vs. average cell diameter for Heathrow, Singapore, and Freetown. Data from the latter two locations were used.

Figure A.2 shows a plot of the various points calculated from the Donaldson (1961), Roys and Kessler (1966), and Briggs (1972) data. The data points have been fit with a curve defined by:

$$D(LWC) = 4.3\ LWC^{-0.26}\ [\exp(\ln LWC)^2]^{-0.16} \qquad (A.2)$$

Equation A.2 is used to evaluate D(LWC) in Eqs. 4.7 and 4.8.

Appendix B: Hail Reflectivity as a Function of Water-coating Thickness

Hail that is coated with liquid water can have a much different radar reflectivity than the same hail dry. The magnitude of the difference depends on the liquid water coating thickness, the hailstone size distribution, and the radar wavelength. Figure B.1 shows the backscatter cross section, σ_b, of water-coated ice spheres as a function of water-coating thickness for ice spheres of various radii for a 10-cm wavelength radar. [Radar reflectivity, Z, is proportional to σ_b; c. f., Battan, 1973; Eq. (B.2) below.] For ice spheres with radii less than ~0.5 cm, the liquid water coating, t, has little effect on σ_b for $t < \sim 10^{-4}$ cm, but for $t > \sim 10^{-4}$ cm, an increase in t results in an increase in σ_b. Smaller ice spheres, with radius less than ~0.5 cm, are within the Rayleigh scattering range for a 10-cm radar (c. f., Battan, 1973). Ice spheres with radii greater than ~0.5 cm are Mie scatterers and the behavior of σ_b with increasing t (for $t > \sim 10^{-4}$ cm) is very erratic and highly dependent on the ice sphere radius.

A scheme, like that proposed in Section 5.2, to correct the t = 0.021 cm reflectivity values to t = 0.01 cm equivalent values, should take into account the effects of the Mie scatterers on the reflectivity, since typically some large hailstones are present. Hailstone size distributions are widely reported as exponential of the following form:

$$N(D) = N_0 e^{-\Lambda D} \tag{B.1}$$

where N(D), usually given in units of m^{-3} cm^{-1} or m^{-3} mm^{-1}, is the number of stones per cubic meter in a given stone diameter interval. N_0 and Λ are constants determined from measurements for a specific location. Equation (B.1) indicates that the number of large stones decreases exponentially with increasing size, but the large stones have a significant contribution to radar reflectivity because, as shown by Eq. (B.2) below, reflectivity is determined from backscatter cross section, and as Fig. B.1 indicates, σ_b increases with increasing hailstone radius. Radar reflectivity is given by:

$$Z = c\int_a^b N(D) \cdot \sigma_b(D)\, dD \tag{B.2}$$

where c is a constant for a given radar and precipitation type, and the limits of integration are typically a = 0 or 0.5 cm[1] and b = D_{max}[2] or ∞.

Using the tables of σ_b given by Battan *et al.* (1970), Ulbrich and Atlas (1982) derived equations for the radar reflectivity of hail as a function of N_o and the median volume diameter, D_o, for t = 0, 0.01, 0.05, and 0.10 cm and for three different radar wavelengths, λ = 3.21, 5.5, and 10 cm (Table B.1). Figure B.2 shows radar reflectivity versus water-coating thickness for five different assumed hail distributions (specified by N_o and D_o), calculated using Table B.1 for a 10 cm radar. Reflectivity increases with increasing water-coating thickness, in the range $0 \leq t \leq 0.10$ cm, for the five distributions chosen. In fact, it can be shown that $Z_{t=0.10} > Z_{t=0.05} > Z_{t=0.01} > Z_{t=0}$ for all hail distributions defined by N_o and D_o with $N_o > 0$ and $0.73 > D_o > 1.95$ cm. To calculate $Z_{t=0.021}$ for a given No and Do one can calculate $Z_{t=0}$, $Z_{t=0.01}$, $Z_{t=0.05}$, and $Z_{t=0.10}$ from the equation in Table B.1 and then fit those four points with a third order curve and use the curve-fit equation to calculate $Z_{t=0.021}$. Figure B.3 shows, in graphical form how this is done.

In Section 5.2, however, the problem is not how to calculate $Z_{t=0.021}$ for a given N_o and D_o, instead the problem is how to calculate $Z_{t=0.01}$ if $Z_{t=0.021}$ is known, but N_o and D_o are unknown. This is accomplished by solving a system of five equations with five unknowns. By definition:

$$dBZ = 10 \log Z$$

Substituting the equation for Z from Table B.1:

$$dBZ = 10 \log [\alpha N_o D_o^m \exp(-\varepsilon D_o)]$$

$$= 10 \log N_o + 10 \log [\alpha N_o D_o^m \exp(-\varepsilon D_o)] \qquad \text{(B.3)}$$

---

[1] Traditionally, ice particles less than 0.5 cm diameter are not considered hail.
[2] Some authors (i. e., Ulbrich and Atlas, 1982) consider the size distribution to be a truncated exponential with no stones larger than some maximum diameter, D_{max}.

D_o can be estimated as explained below, thereby reducing the 2nd term on the right hand side of Eq. (B.3) to a constant for a given water-coating thickness. This results in four equations:

$$dBZ_{t=0} = 10 \log N_o + C_1 \quad \text{(B.4)}$$

$$dBZ_{t=0.01} = 10 \log N_o + C_2 \quad \text{(B.5)}$$

$$dBZ_{t=0.05} = 10 \log N_o + C_3 \quad \text{(B.6)}$$

$$dBZ_{t=0.10} = 10 \log N_o + C_4 \quad \text{(B.7)}$$

where C_1, C_2, C_3, and C_4 are calculated from the values of α, m, and ε in Table B.1 for the given value of t, and from the estimated value of D_o. The fifth equation comes from the equation for a third order curve fit from four points:

$$dBZ_{t=t_1} = C_5\, dBZ_{t=0} + C_6\, dBZ_{t=0.01} + C_7\, dBZ_{t=0.05} + C_8\, dBZ_{t=0.10} \quad \text{(B.8)}$$

where, for example,

$$C_5 = (t_1 - 0.01)(t_1 - 0.05)(t_1 - 0.10) / (0 - 0.01)(0 - 0.05)(0 - 0.10) \quad \text{(B.9)}$$

Using $t_1 = 0.021$ in Eq. (B.8) gives the fifth equation:

$$dBZ_{t=0.021} = C_5\, dBZ_{t=0} + C_6\, dBZ_{t=0.01} + C_7\, dBZ_{t=0.05} + C_8\, dBZ_{t=0.10} \quad \text{(B.10)}$$

where $dBZ_{t=0.021}$ is the uncorrected ARC value and from Eq. (B.9) it is obvious that C_5, C_6, C_7, and C_8 are easily calculated. So, Eqs. (B.4) - (B.7) and (B.10) are a system of five equations with five unknowns, with the unknowns being $dBZ_{t=0}$, $dBZ_{t=0.01}$, $dBZ_{t=0.05}$, $dBZ_{t=0.10}$, and N_o. Notice that one of the unknowns, $dBZ_{t=0.01}$, is the t = 0.01 cm equivalent reflectivity of interest.

The solution outlined above, however, was predicated on being able to estimate D_o. Ulbrich and Atlas (1982) derived an empirical relationship between HWC and D_o using data from Federer and Waldvogel (1975):

$$HWC = 1.49\ D_o^{4.39} \tag{B.11}$$

Initially HWC is estimated from $Z_{t=0.021}$ using Eq. (5.2), and then D_o is estimated using Eq. (B.11). The D_o value calculated in this manner, though, is in theory an overestimation since HWC was calculated using $Z_{t=0.021}$ and not the t = 0.01 cm equivalent reflectivity, $Z_{t=0.01}$. It is used, however, the first time the system of five equations is solved to get an estimate of $dBZ_{t=0.01}$. Then a second estimate of D_o is calculated from the first $dBZ_{t=0.01}$ estimate and the process is repeated in this matter, eventually converging on a value of $dBZ_{t=0.01}$.

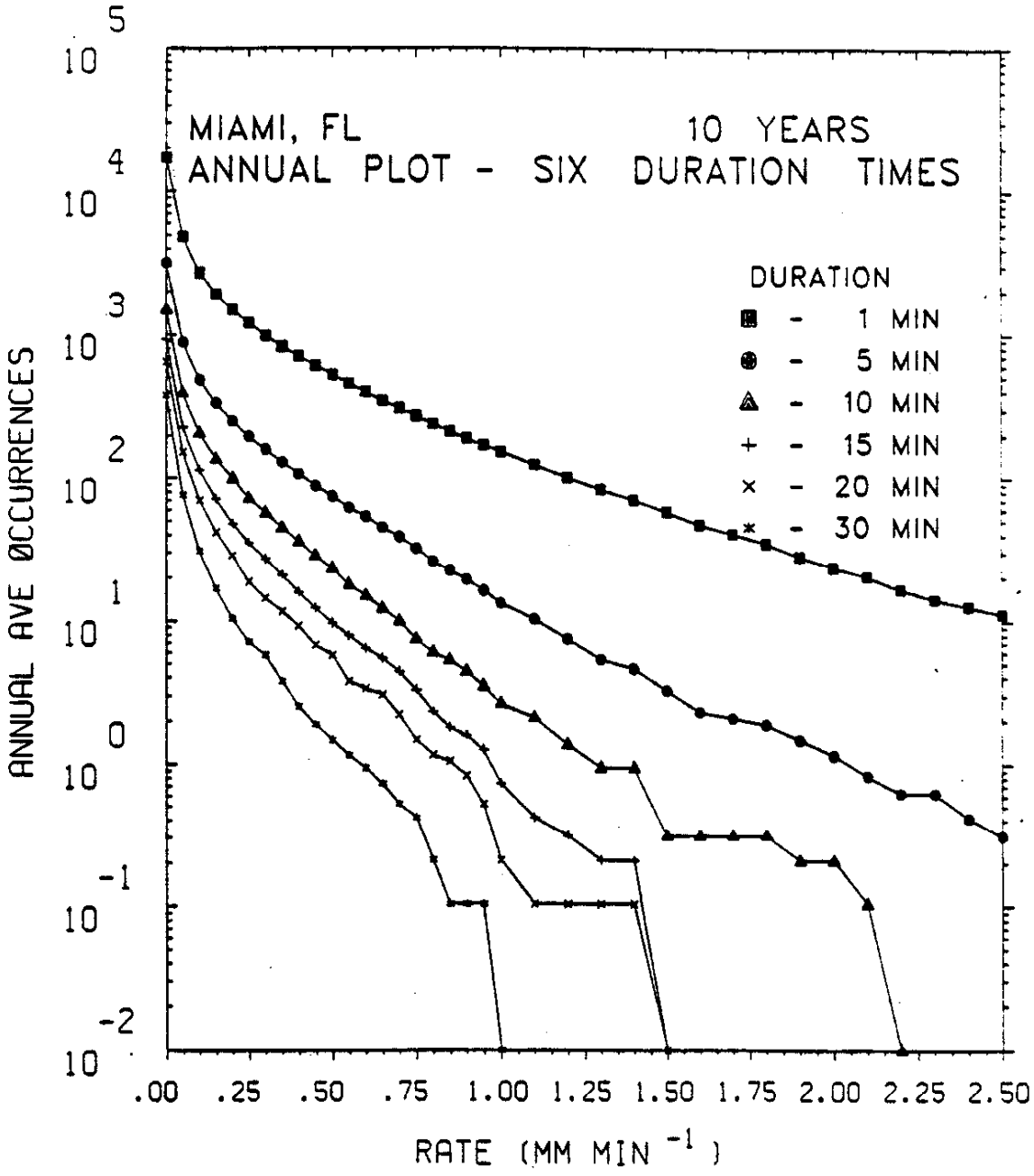

Fig. 4.1. Annual average number of occurrences of 1-min rain rates for six duration times at Miami, Fl. Rain rates are those equalled or exceeded during each minute of the specified duration. (From Tattelman and Larson, 1989)

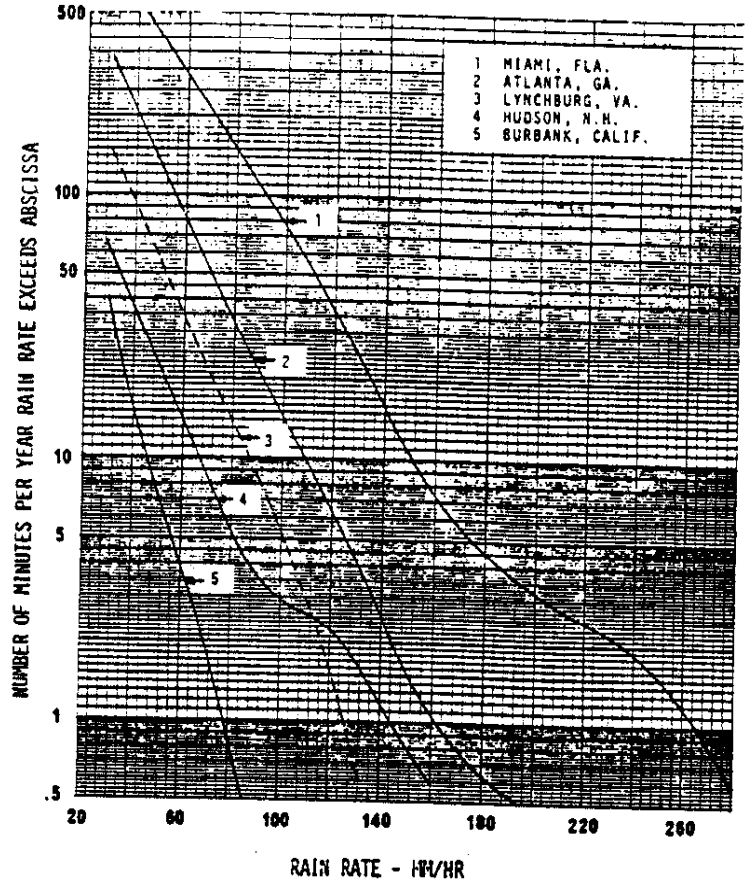

Fig. 4.2. Number of minutes per year given rain rate is exceeded for five locations including Miami. (From Bodtmann and Ruthroff, 1976)

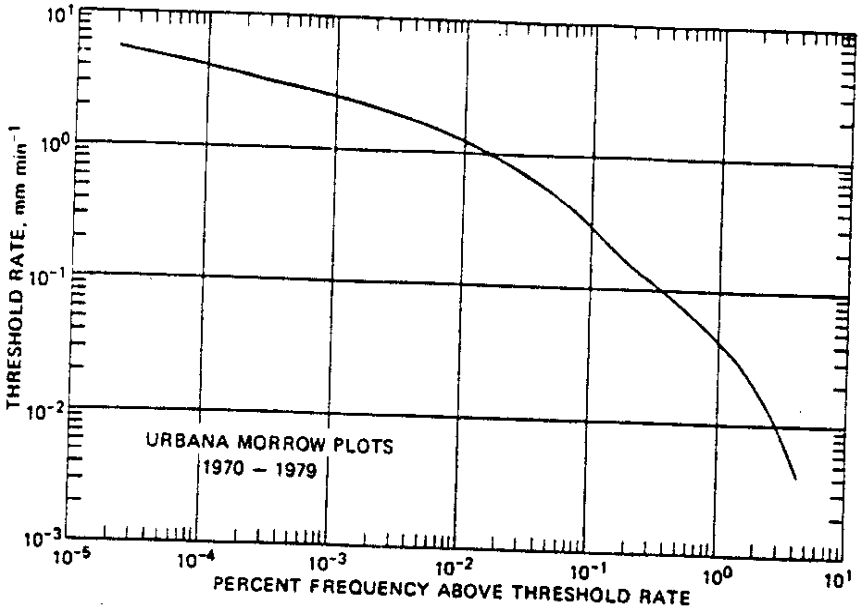

Fig. 4.3. The percent frequency of occurrence of precipitation above threshold rates for the ten-year interval 1970-79, for Urbana, IL (1 min rates). (From Jones and Wendland, 1984)

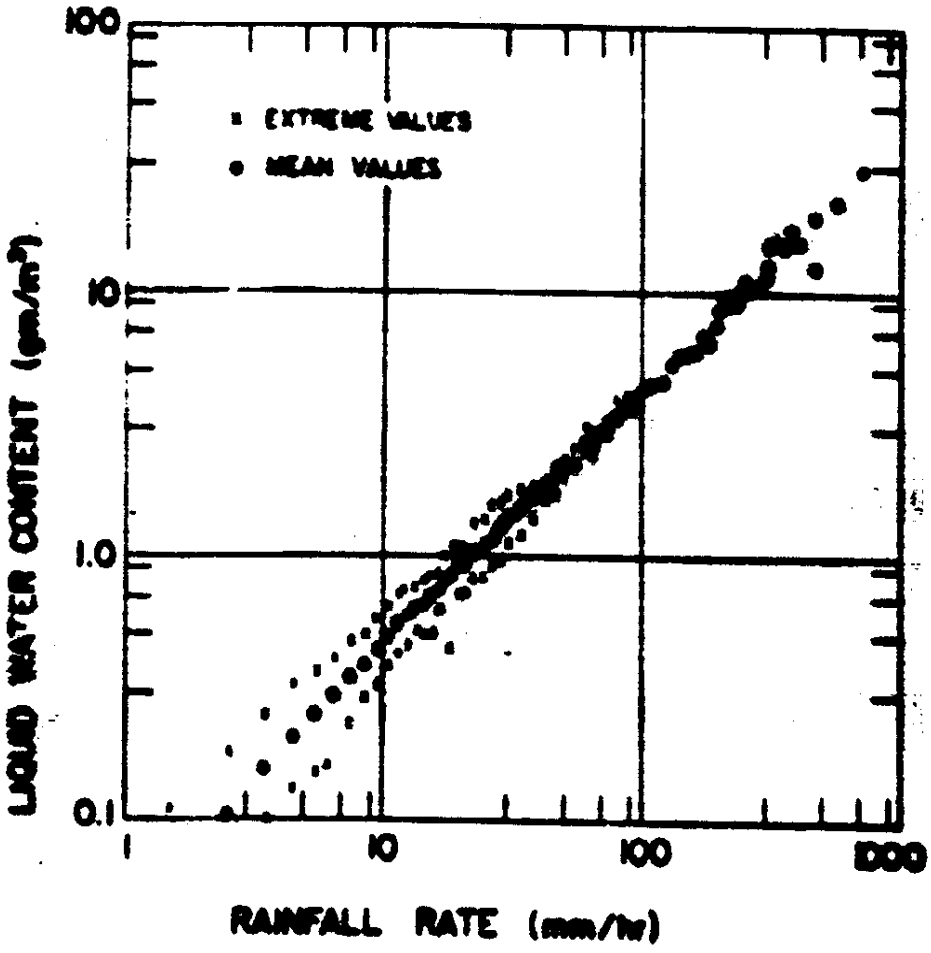

Fig. 4.4. Example of a scatter plot of rainfall rate versus liquid water content. (From Mueller and Sims, 1966)

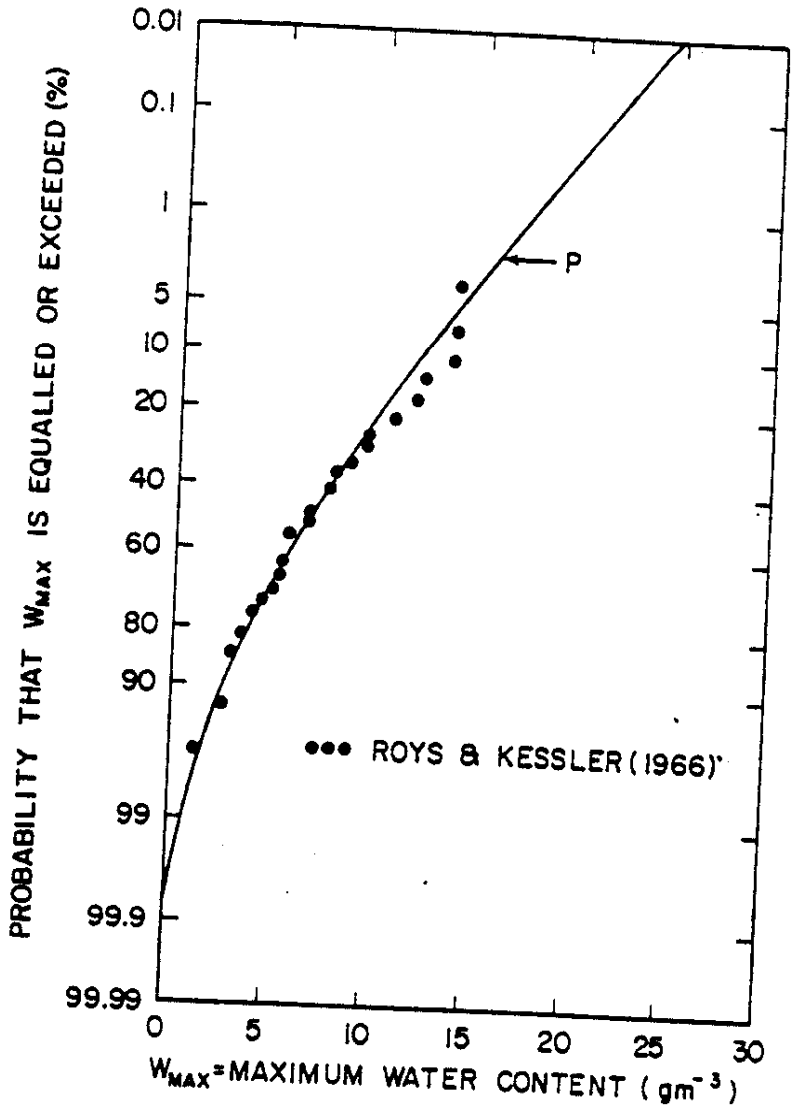

Fig. 4.5. Probability of maximum liquid water content within Oklahoma thunderstorms. (From Jursa, 1985)

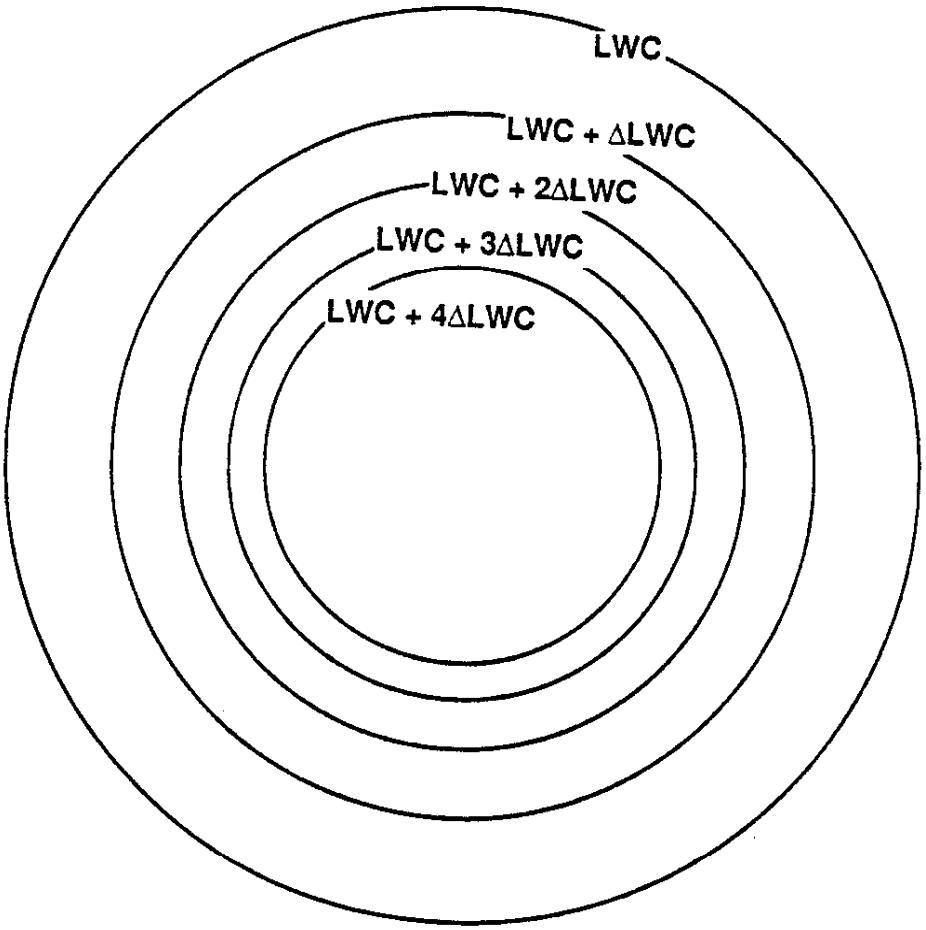

Fig. 4.6. Simplified cross-section of a thunderstorm cell.

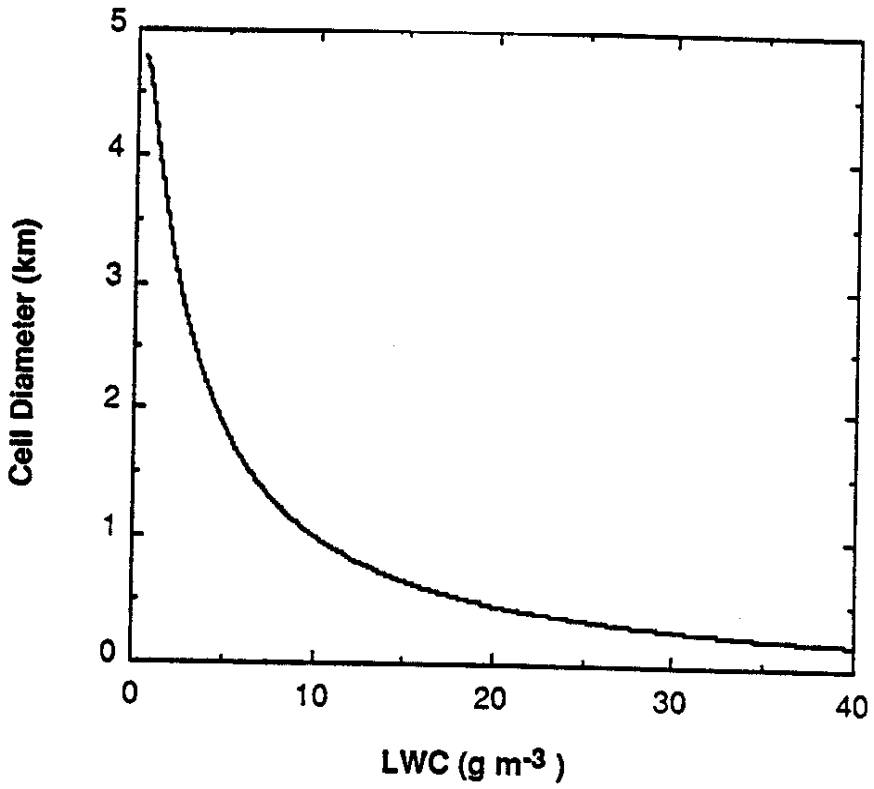

Fig. 4.7. Diameter of the region in which a given LWC value is equalled or exceeded as a function of LWC.

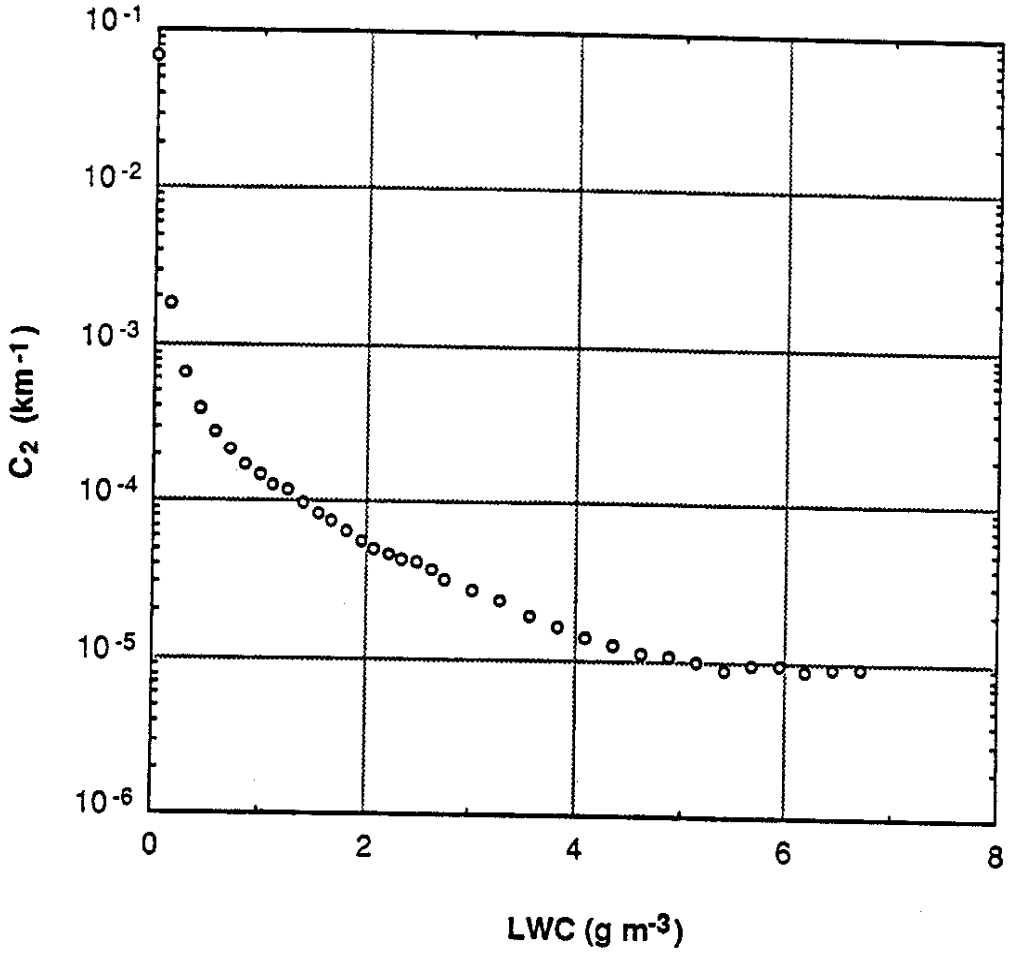

Fig. 4.8. The "constant", C_2, as a function of LWC.

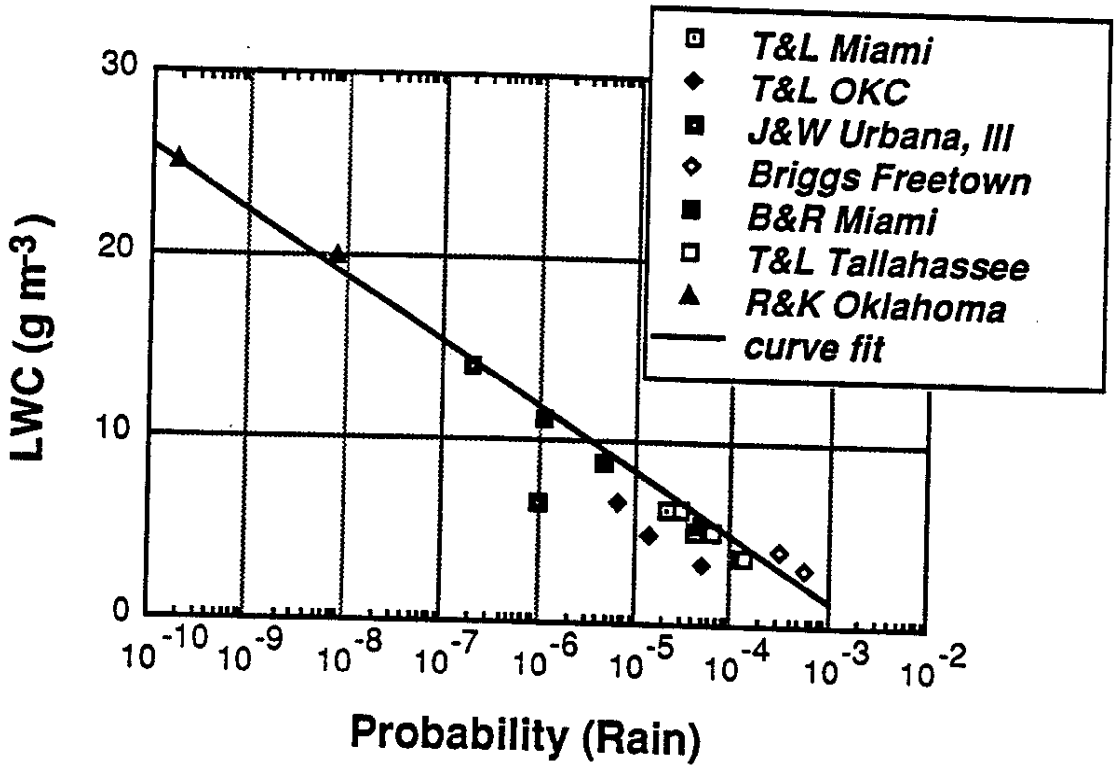

Fig. 4.9. The probability of a given LWC value being equalled or exceeded at a point at any random instant in a worst case location for each probability level. Data points, as described in the text, are indicated.

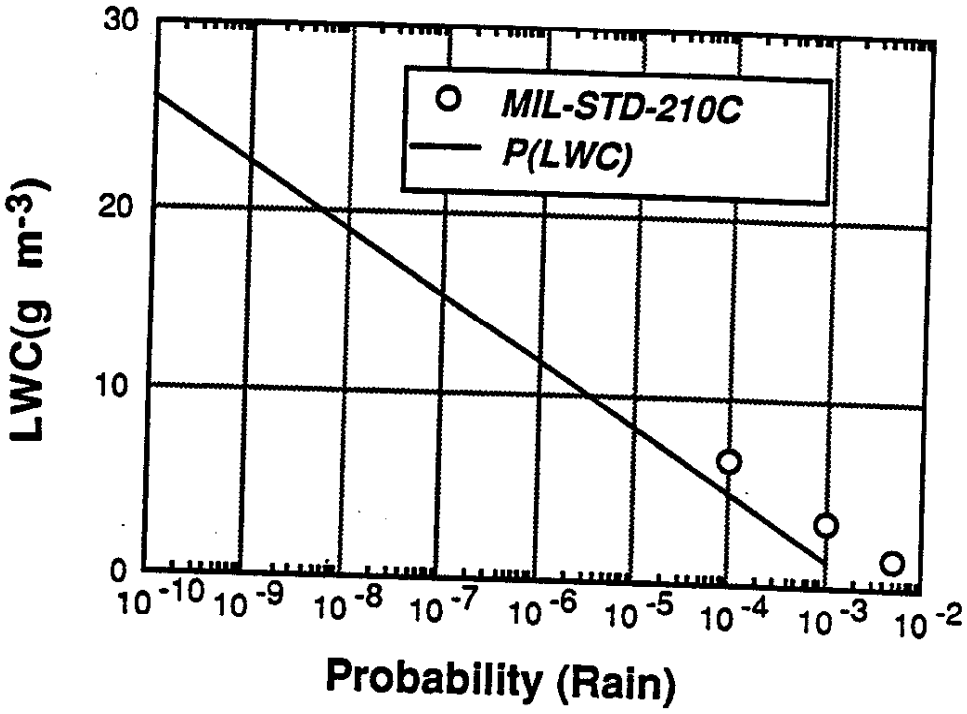

Fig. 4.10. The rain curve as in Fig. 4.9 with the MIL-STD-210C (Department of Defense, 1987) 0.5%, 0.1%, and 0.01% of time worst case, worst month data points.

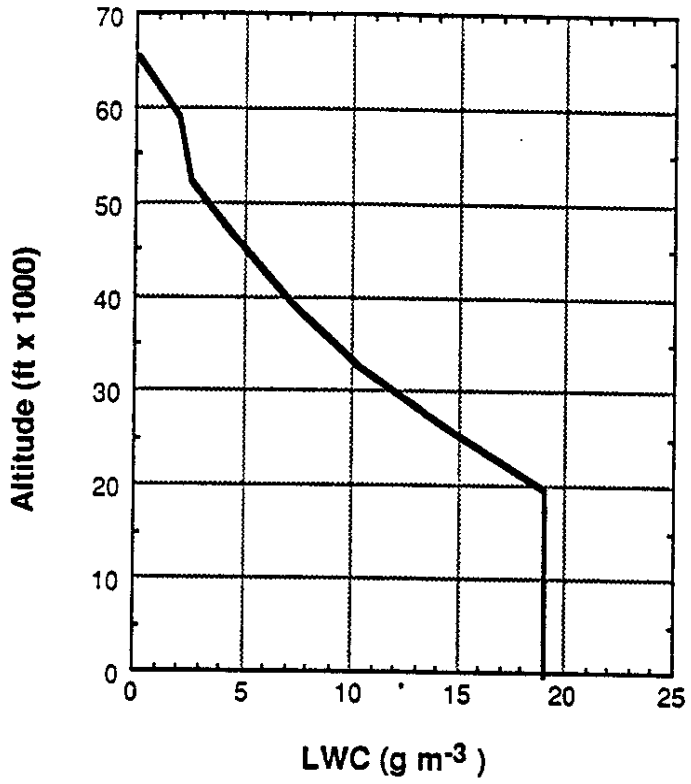

Fig. 4.11. Vertical profile of LWC for the 10^{-8} probability LWC of 18.9 g m^{-3}.

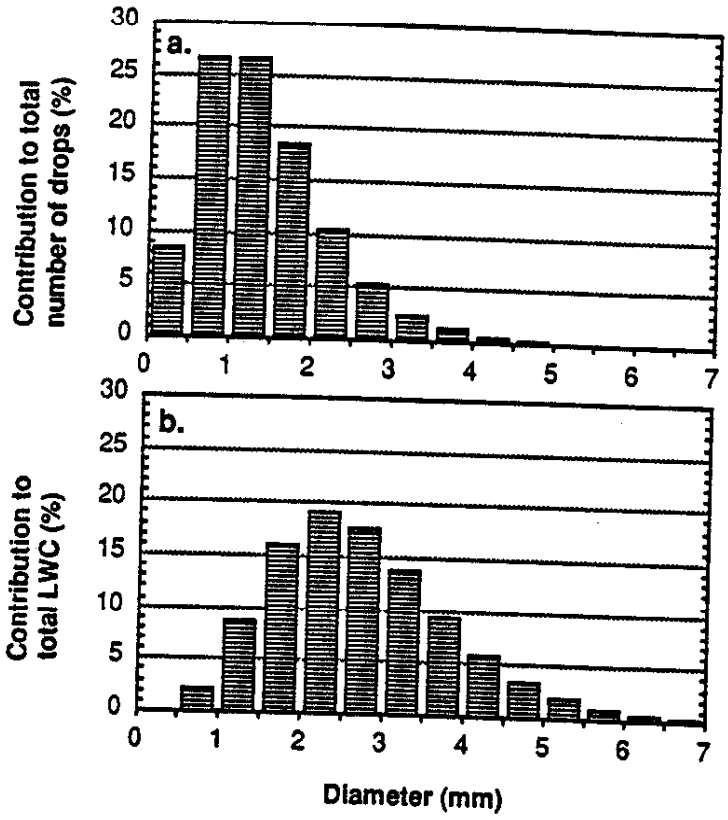

Fig. 4.12. a.) The contribution to the total number of raindrops from each 0.5 mm diameter interval, b.) the contribution to the total LWC from each 0.5 mm diameter interval.

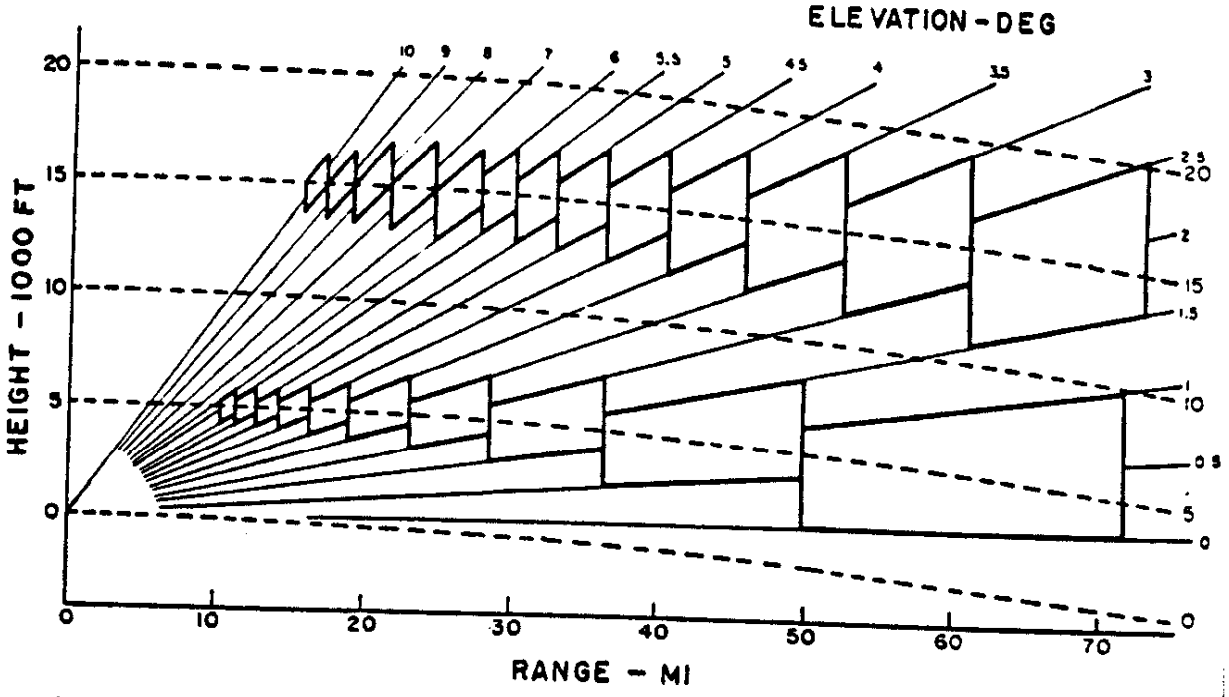

Fig. 5.1. Lines of constant altitude (dashed) corrected for the earth's curvature and normal refraction plotted against range. Diagram illustrates how a CAPPI is obtained.. (From Marshall, 1957).

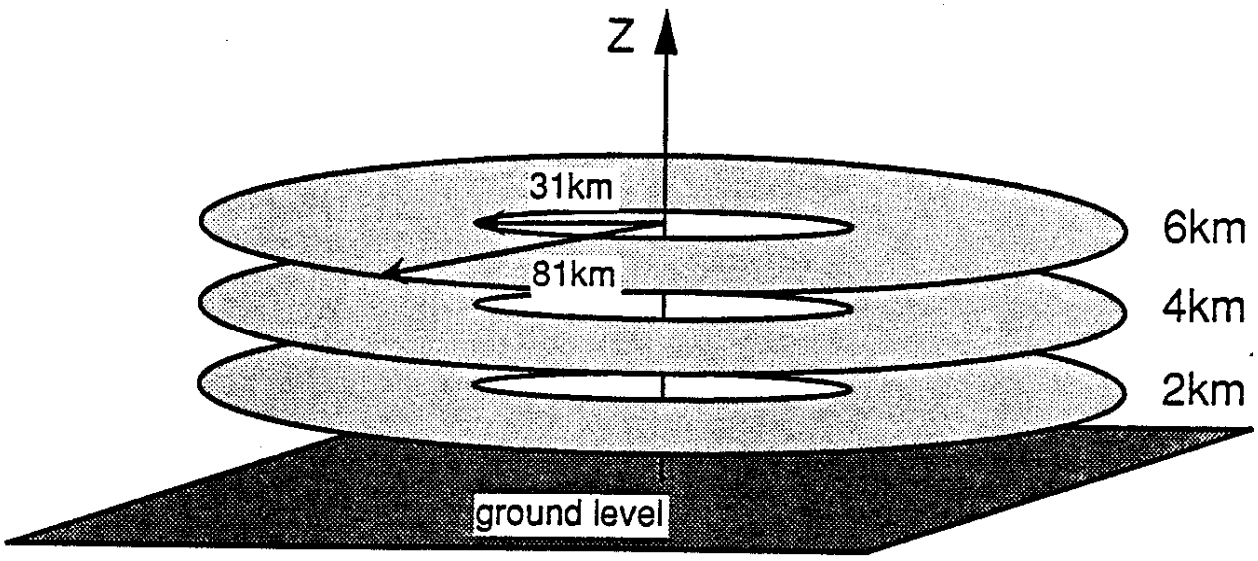

Fig. 5.2. The ARC data domain. The light stippled regions are the CAPPI levels at 2, 4, and 6 km above ground level.

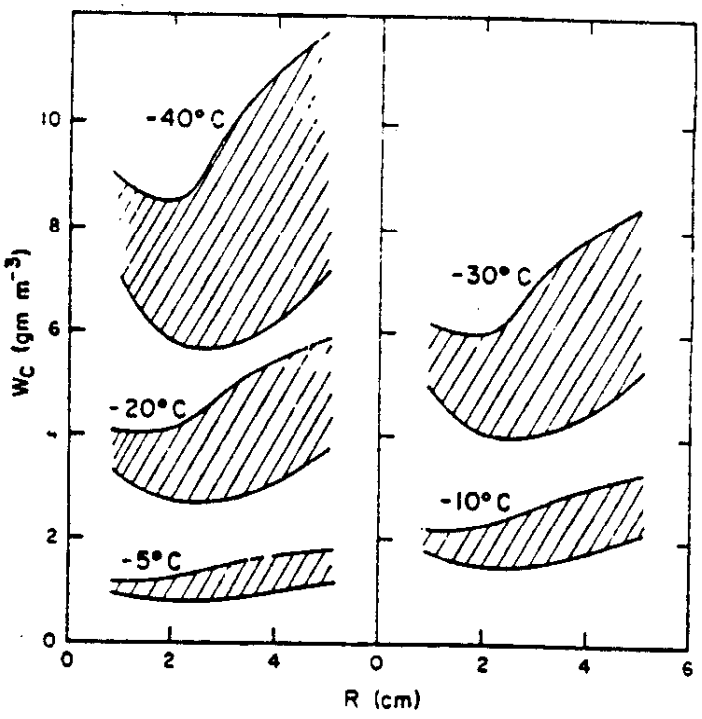

Fig. 5.3. Values of the critical liquid water concentrations, W_c, necessary for wet growth of hailstones, as a function of the stone radius, R, for different ambient temperatures. The stippled region reflects the range of collection efficiencies, depending mainly on cloud droplet radius. (From Macklin and Bailey, 1968)

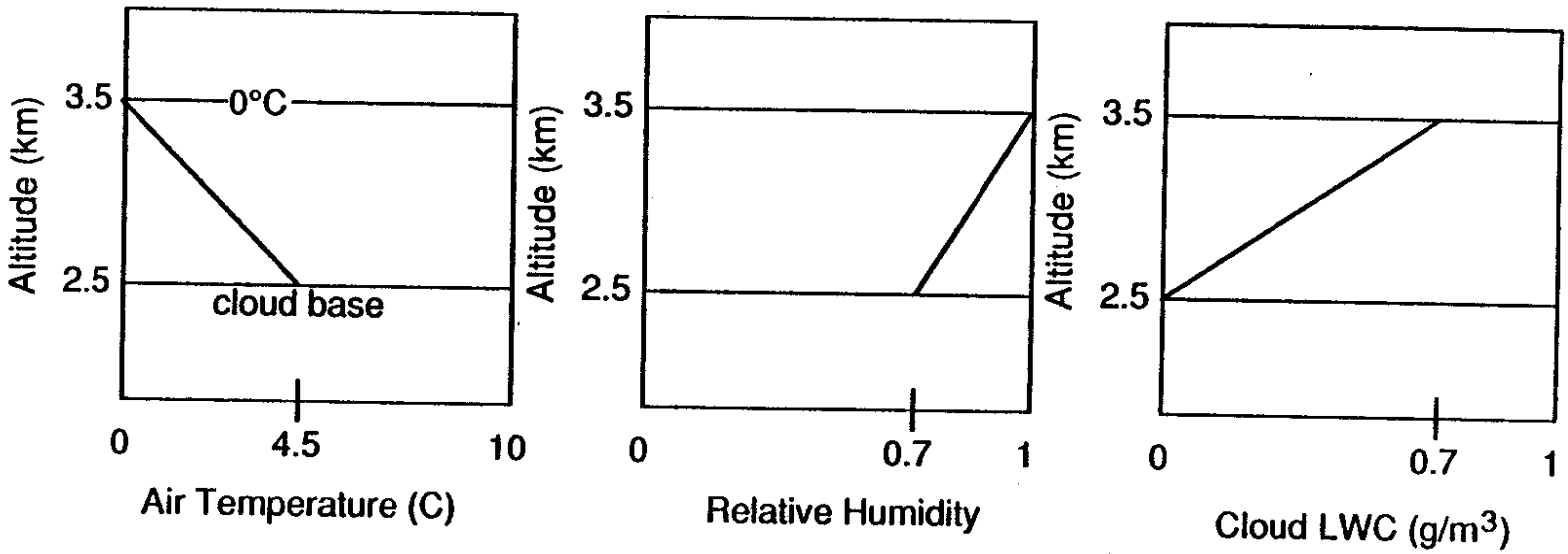

Fig. 5.4. Atmospheric inputs used in the Rasmussen and Heymsfield (1987) melting model. The cloud base and freezing level heights are averages for Alberta hailstorms (ARC, private communication). Altitude is given in height above mean sea level.

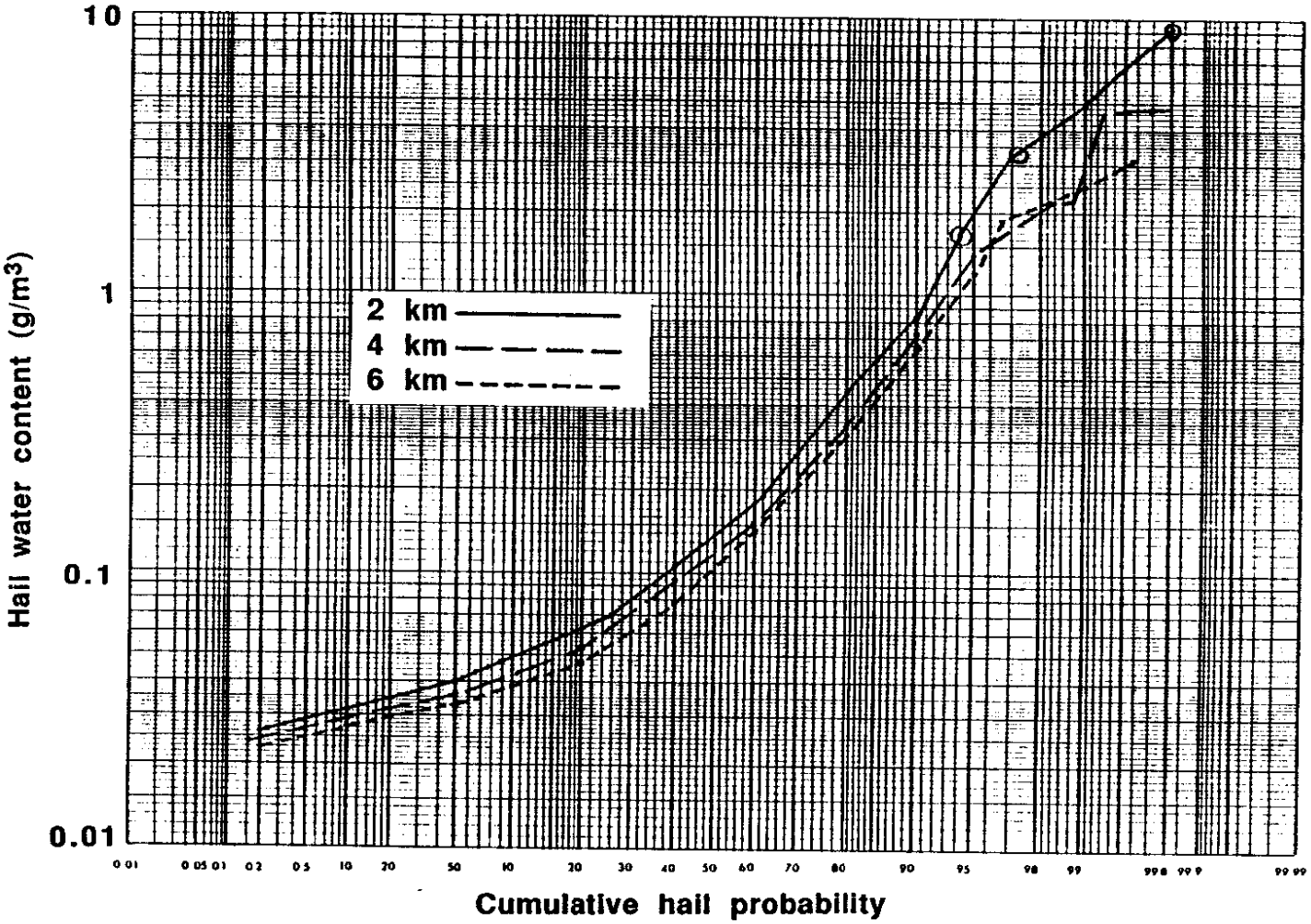

Fig. 5.5. Cumulative HWC distributions at 2, 4, and 6 km above ground level, derived from ARC reflectivity data.

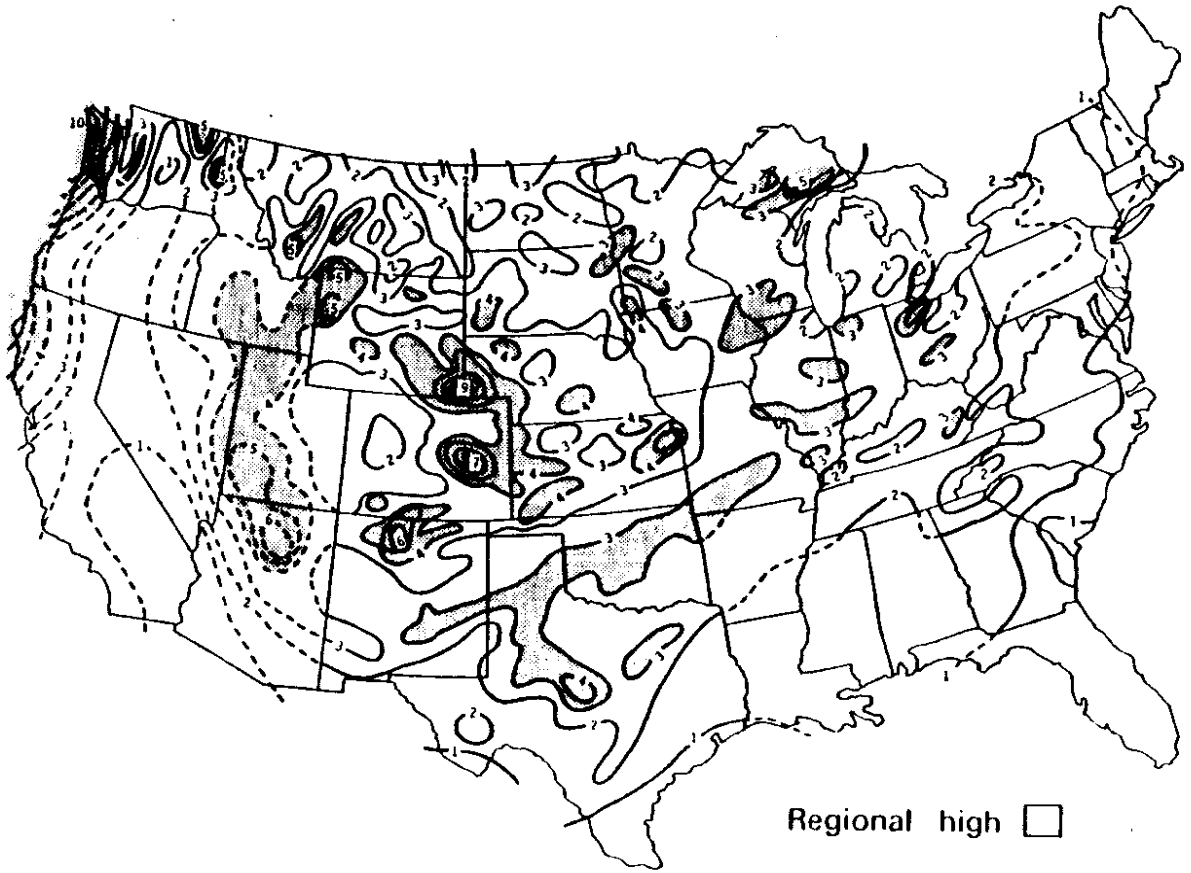

Fig. 5.6. Average annual number of days with hail based on point frequencies. (From Changnon, 1977.)

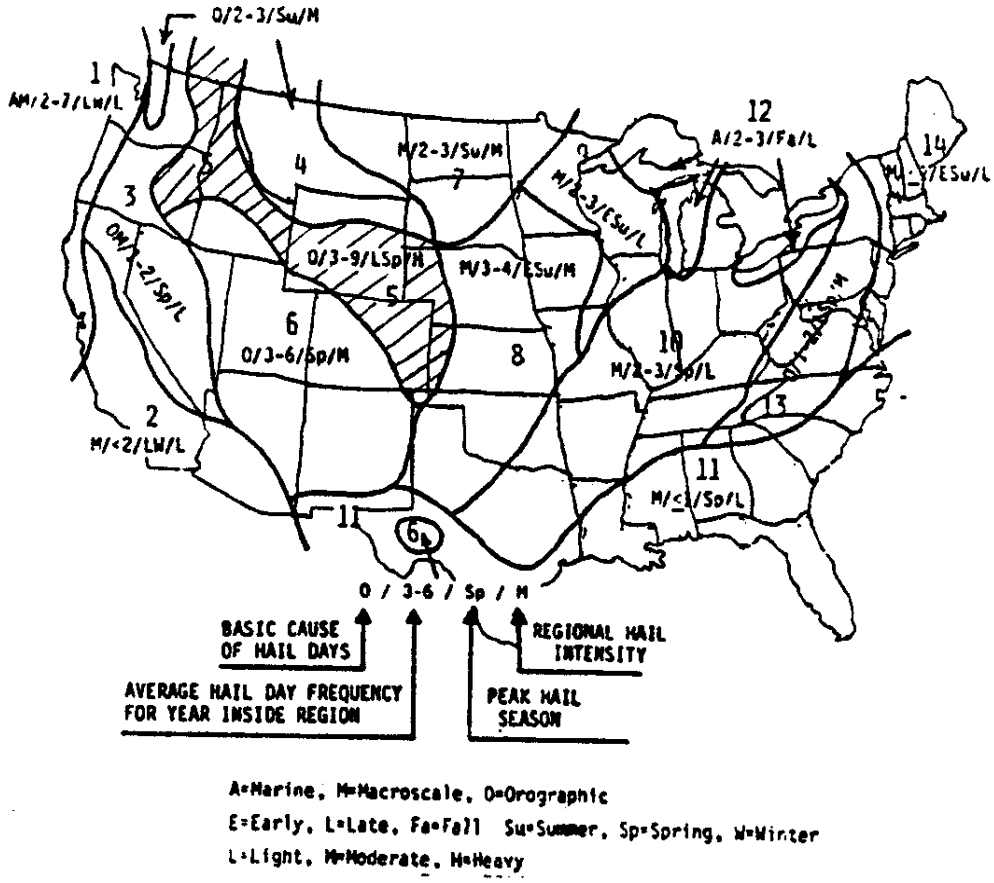

Fig. 5.7. Hail regions of the United States. The striped region is where the most severe hail occurs. (After Changnon, 1977.)

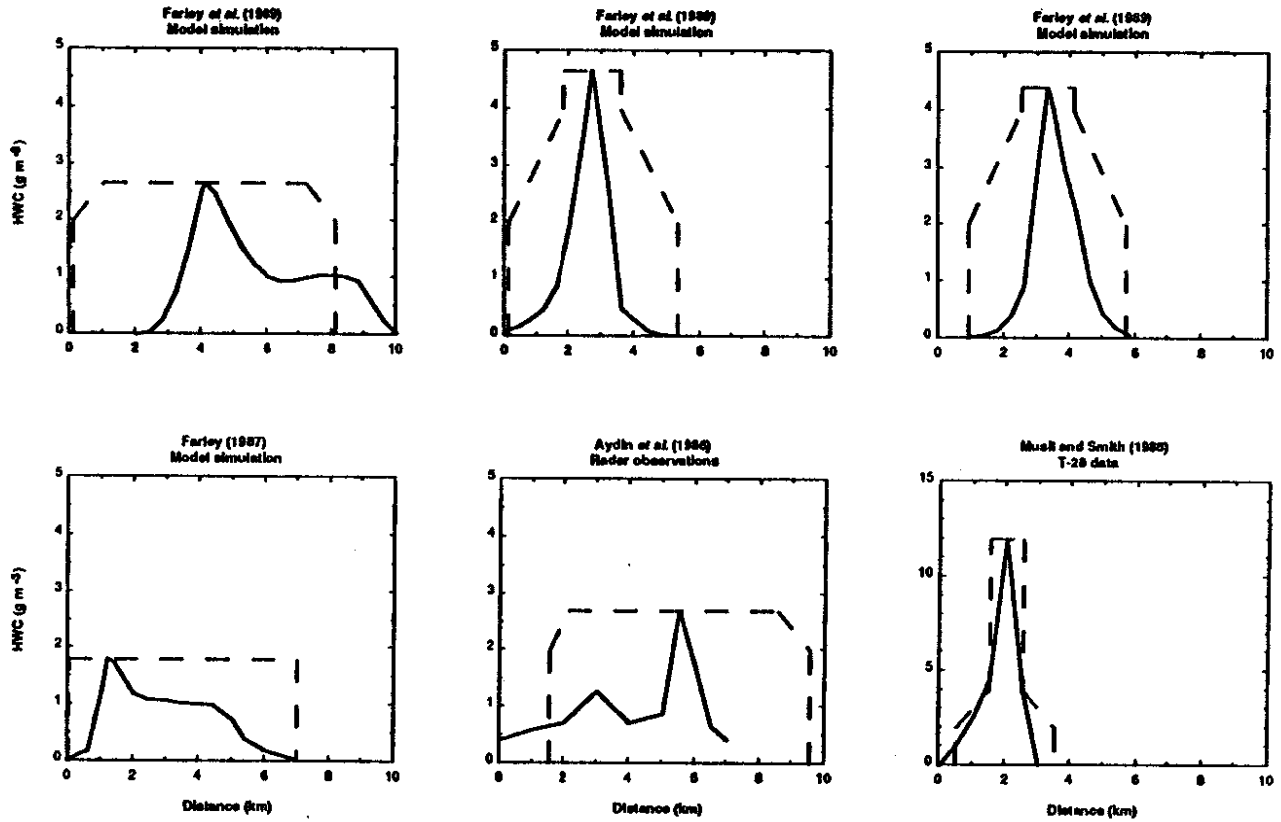

Fig. 5.8. Examples of across-cell HWC distributions (solid curves) and the implied HWC distribution (dashed curves) based on the assumptions concerning hail shaft diameter as a function of HWC as discussed in the text. Farley (1987) and Farley *et al.* (1989) distributions are based on model results from a 2-D, time dependent cloud model. The Aydin *et al.* (1986) HWC distribution is based on radar reflectivity data which has been converted to HWC here. The Musil and Smith (1988) HWC distribution is based on data collected by the armoured T-28 airplane.

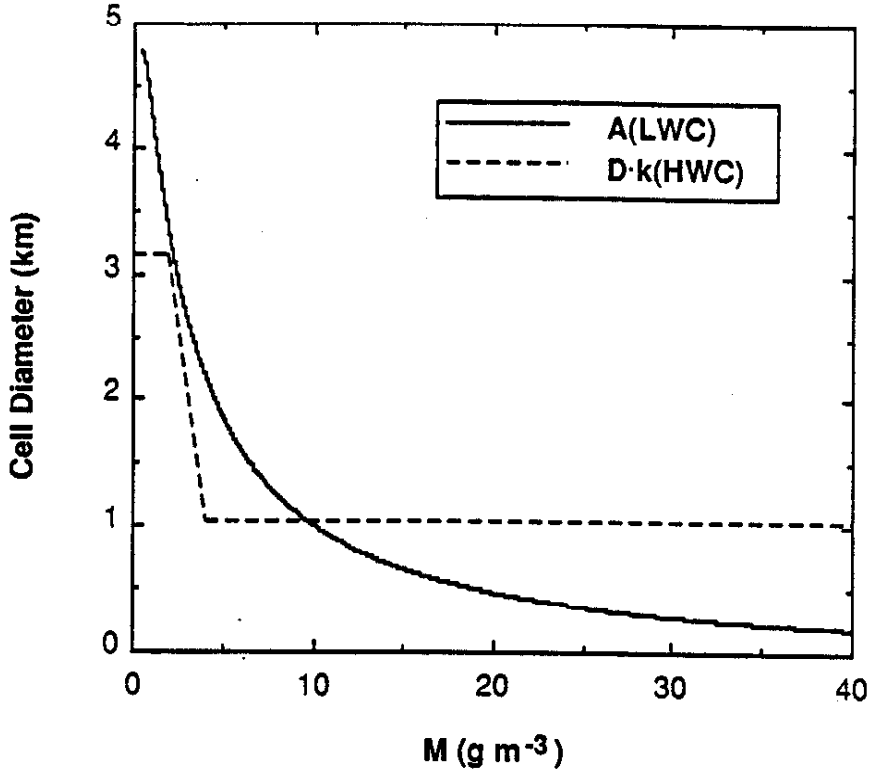

Fig. 5.9. As in Fig. 4.7 except with the diameter of the region in which a given HWC value is equalled or exceeded as a function of HWC, D·k(HWC), included.

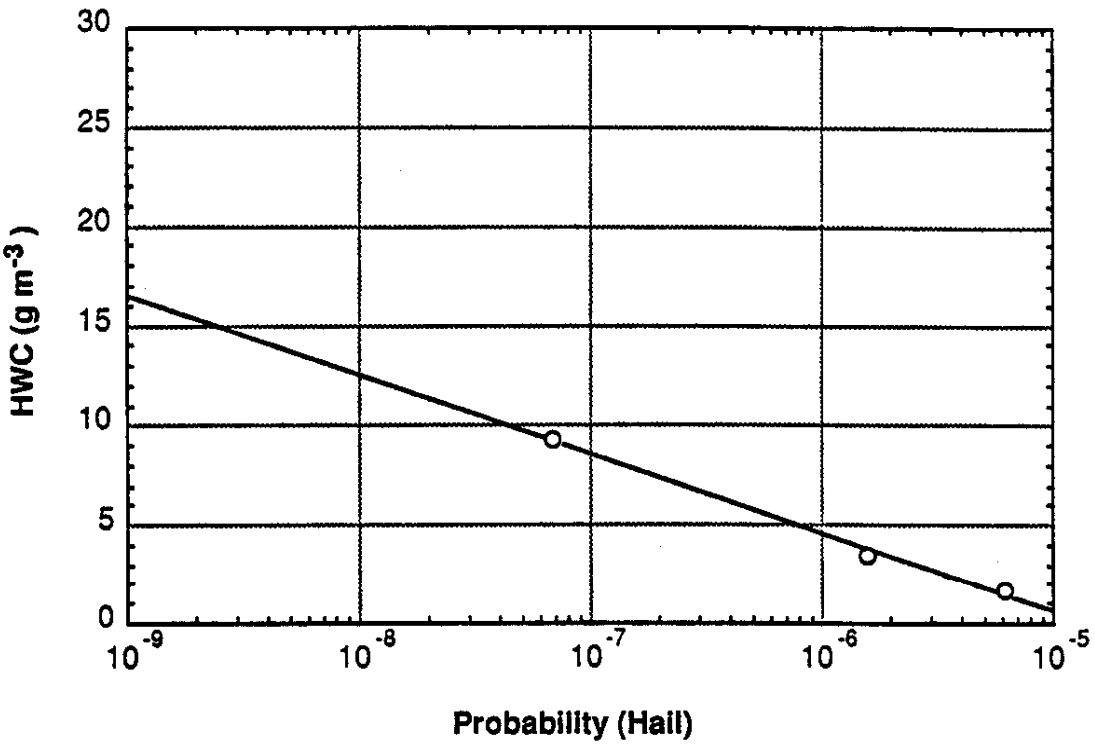

Fig. 5.10. The Boeing-derived hail curve with the three data points used to define the curve fit.

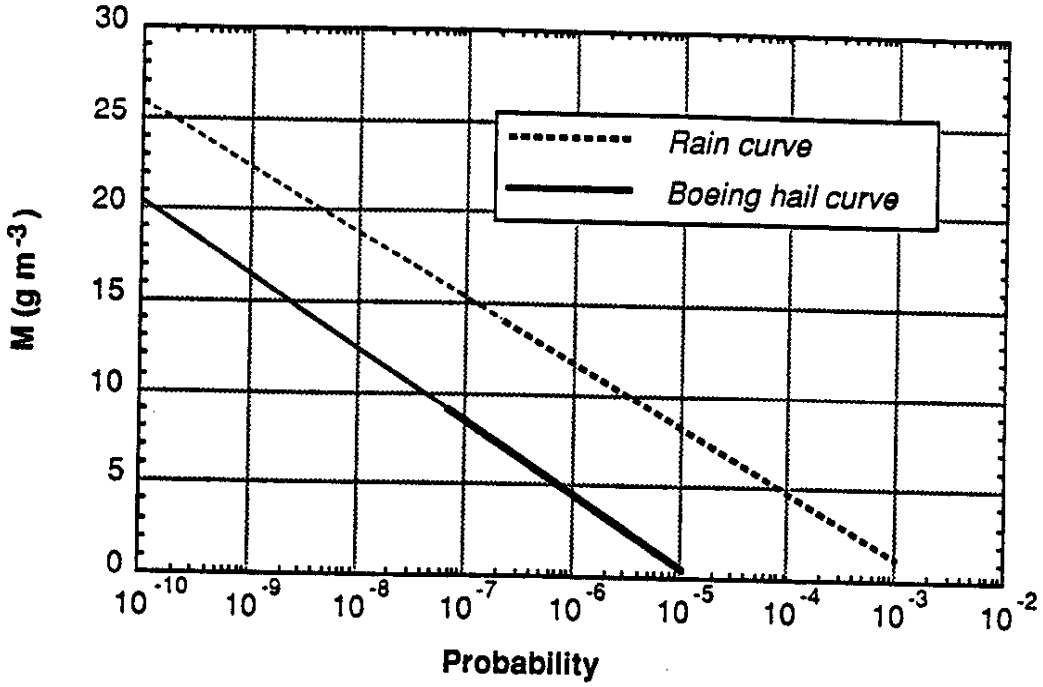

Fig. 5.11. Comparison of the rain curve and Boeing-derived hail curve. Thin portion of the curves indicate extrapolated data.

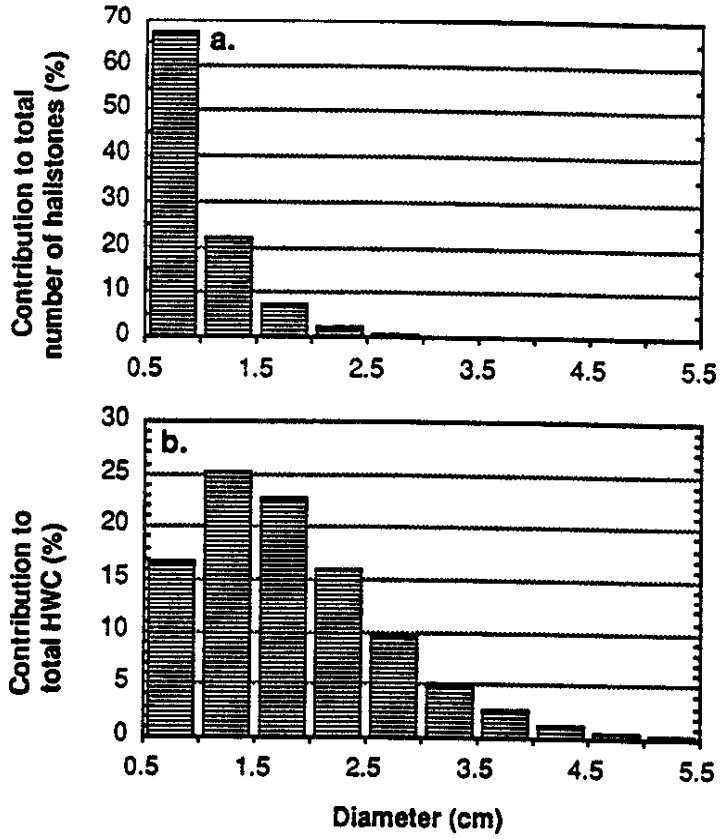

Fig. 5.12. a.)The contribution to the total number of hailstones from each 0.5 cm diameter interval, b.) the contribution to the total HWC from each 0.5 cm diameter interval.

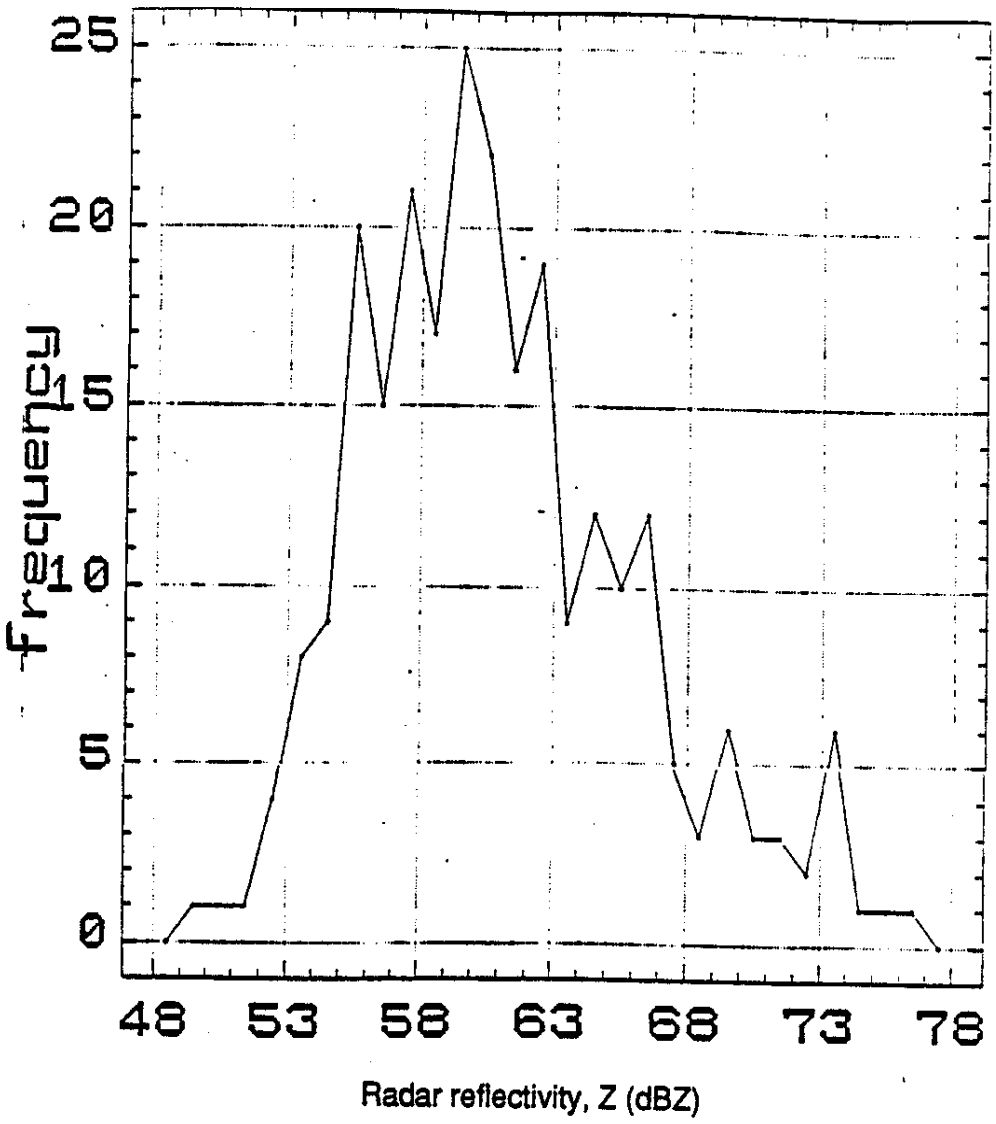

Fig. 6.1. Frequency distribution of the 253 GNEFA-supplied Z_{max} values. (From Husson *et al.*, 1989.)

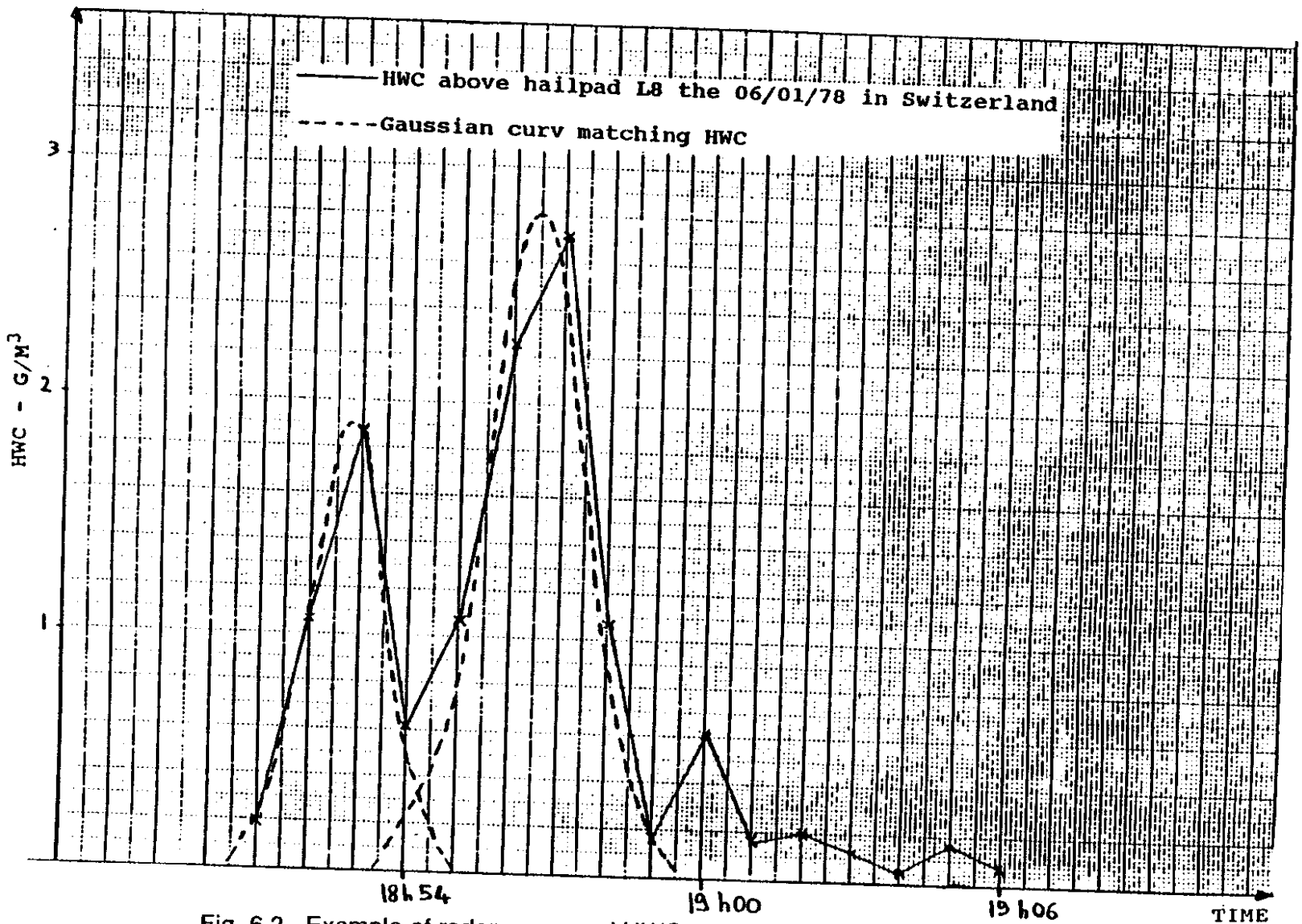

Fig. 6.2. Example of radar-measured HWC versus time over a fixed point in Switzerland on 01 June 1978.

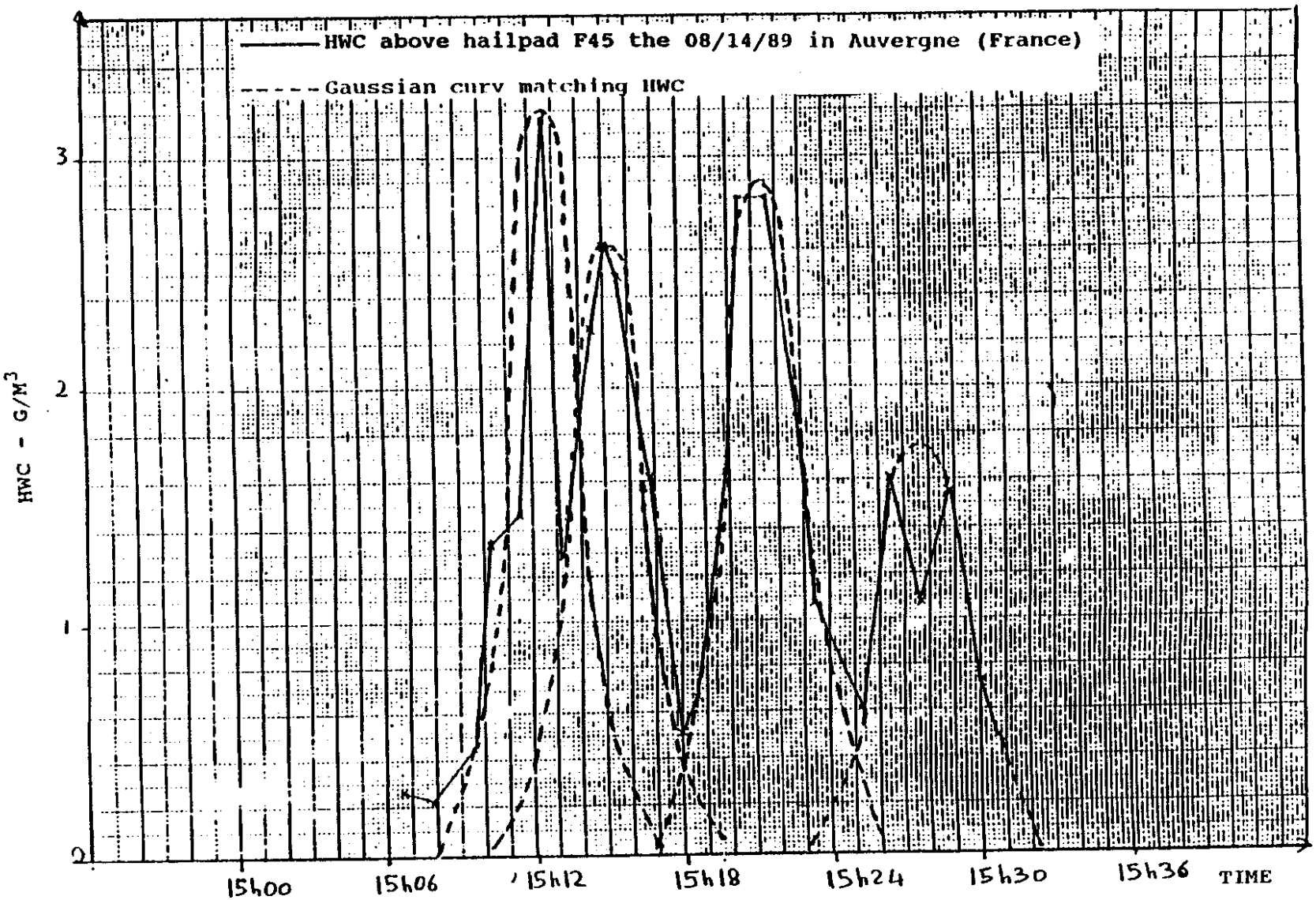

Fig. 6.3. As in Fig. 6.2 except in France on 14 August 1989.

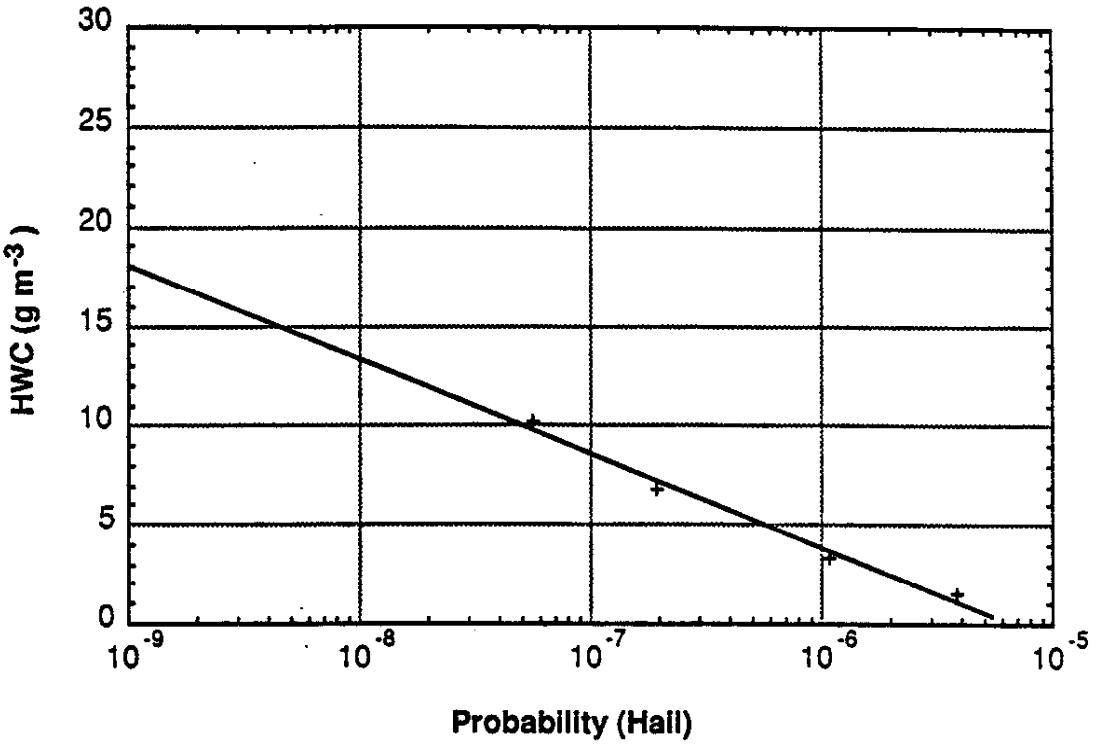

Fig. 6.4. The CFMI-derived hail curve with the four data points used to define the curve fit.

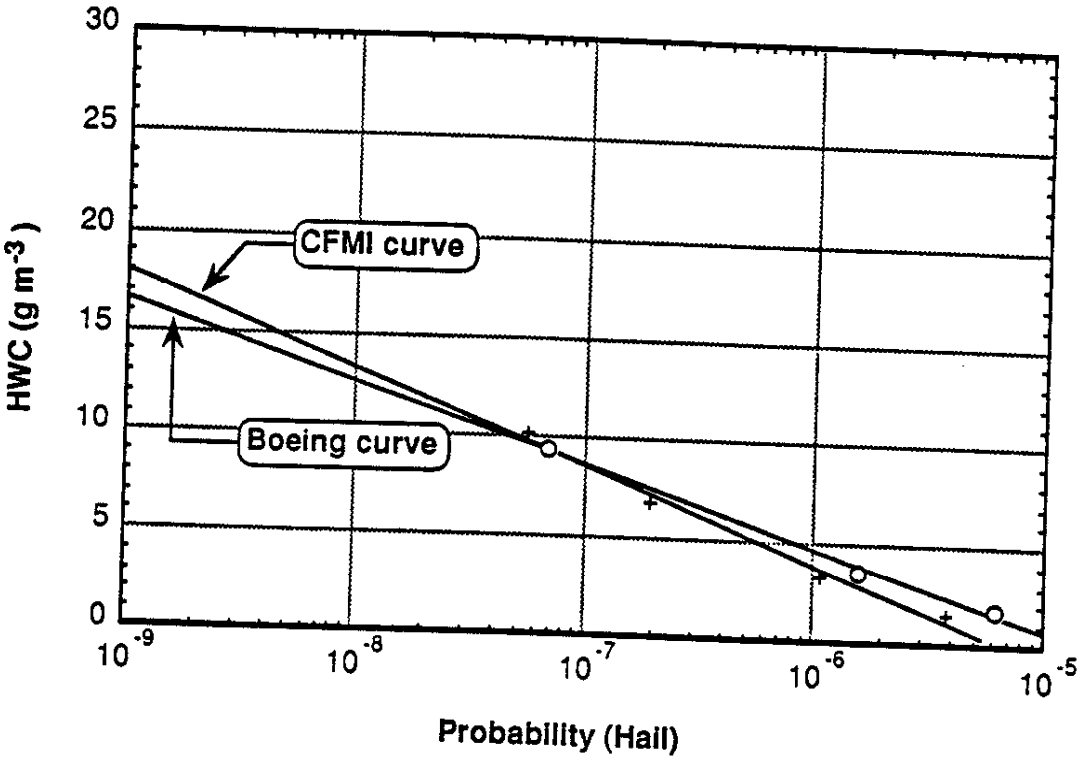

Fig. 7.1. Comparison of the Boeing-derived and CFMI-derived hail curves.

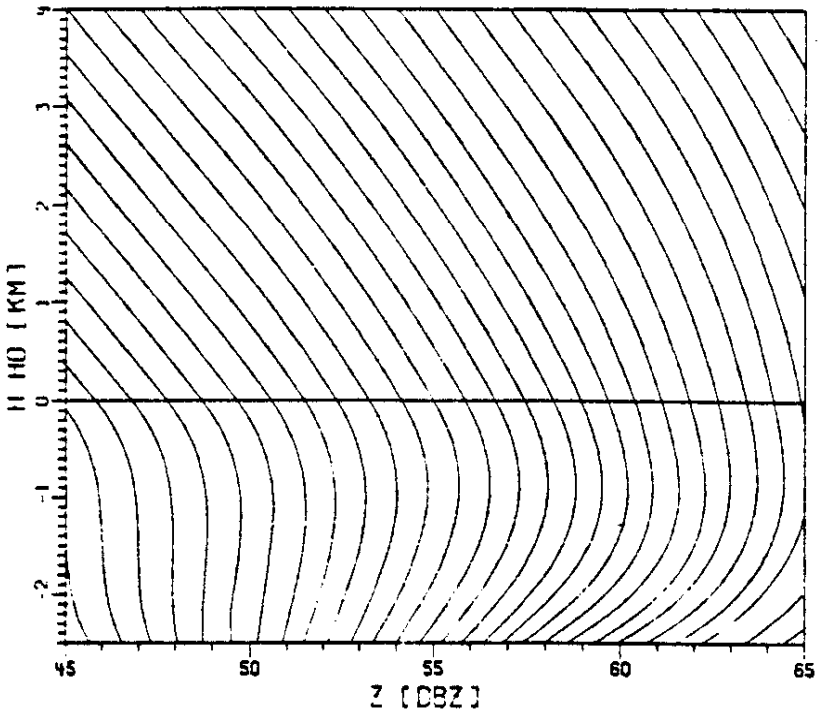

Fig. 7.2. Radar reflectivity profiles obtained by methods discussed by Schmid and Waldvogel (1986). On the ordinate, H is height, and HO is the height of the freezing level. (From Schmid and Waldvogel, 1986.)

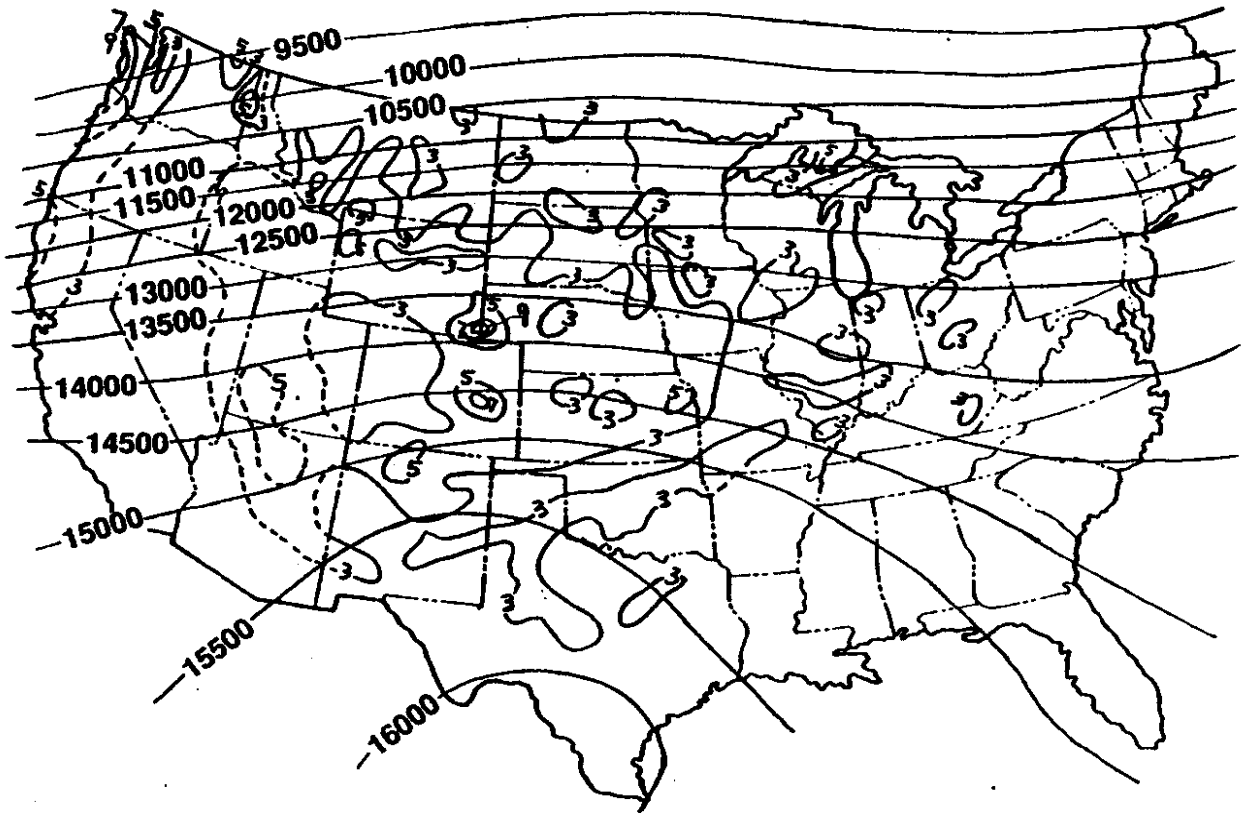

Fig. 7.3. Isopleths of mean June freezing level height in feet in the United States. Superimposed is the annual average number of days with hail as in Fig. 5.6.

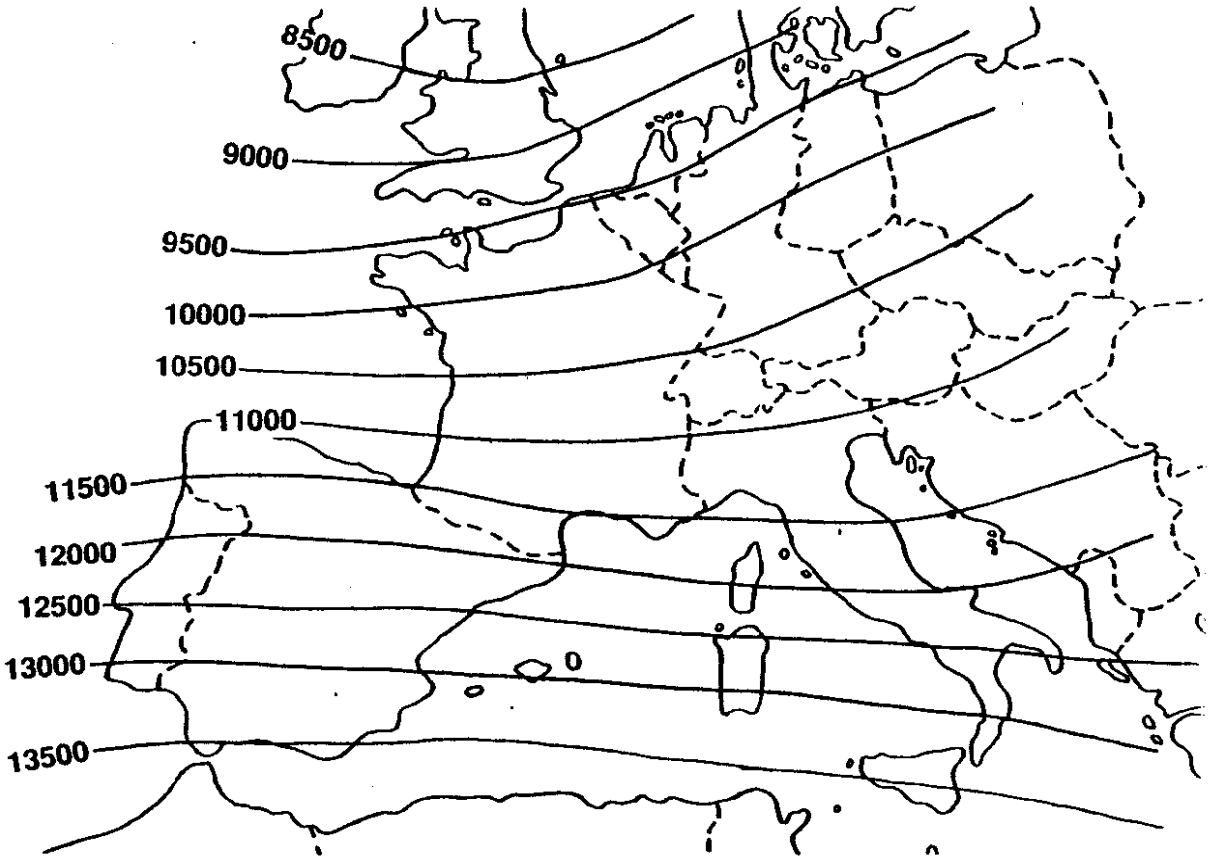

Fig. 7.4. Isopleths of mean June freezing level height in feet in Europe.

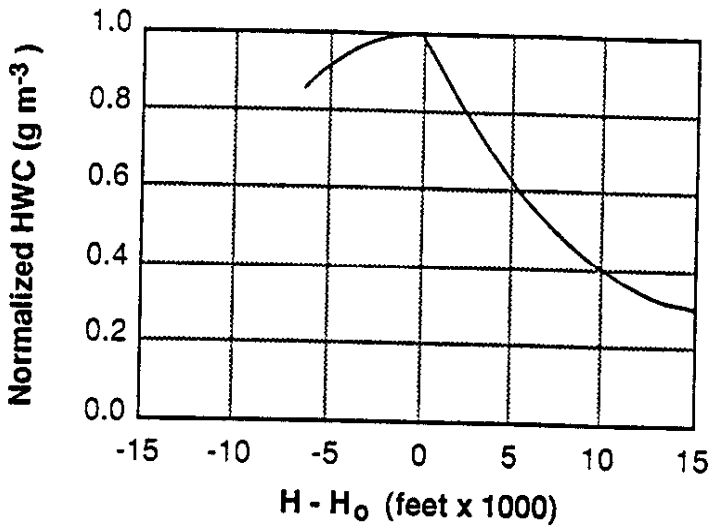

Fig. 7.5. Normalized HWC as a function of height, H, above the freezing level height, H_o.

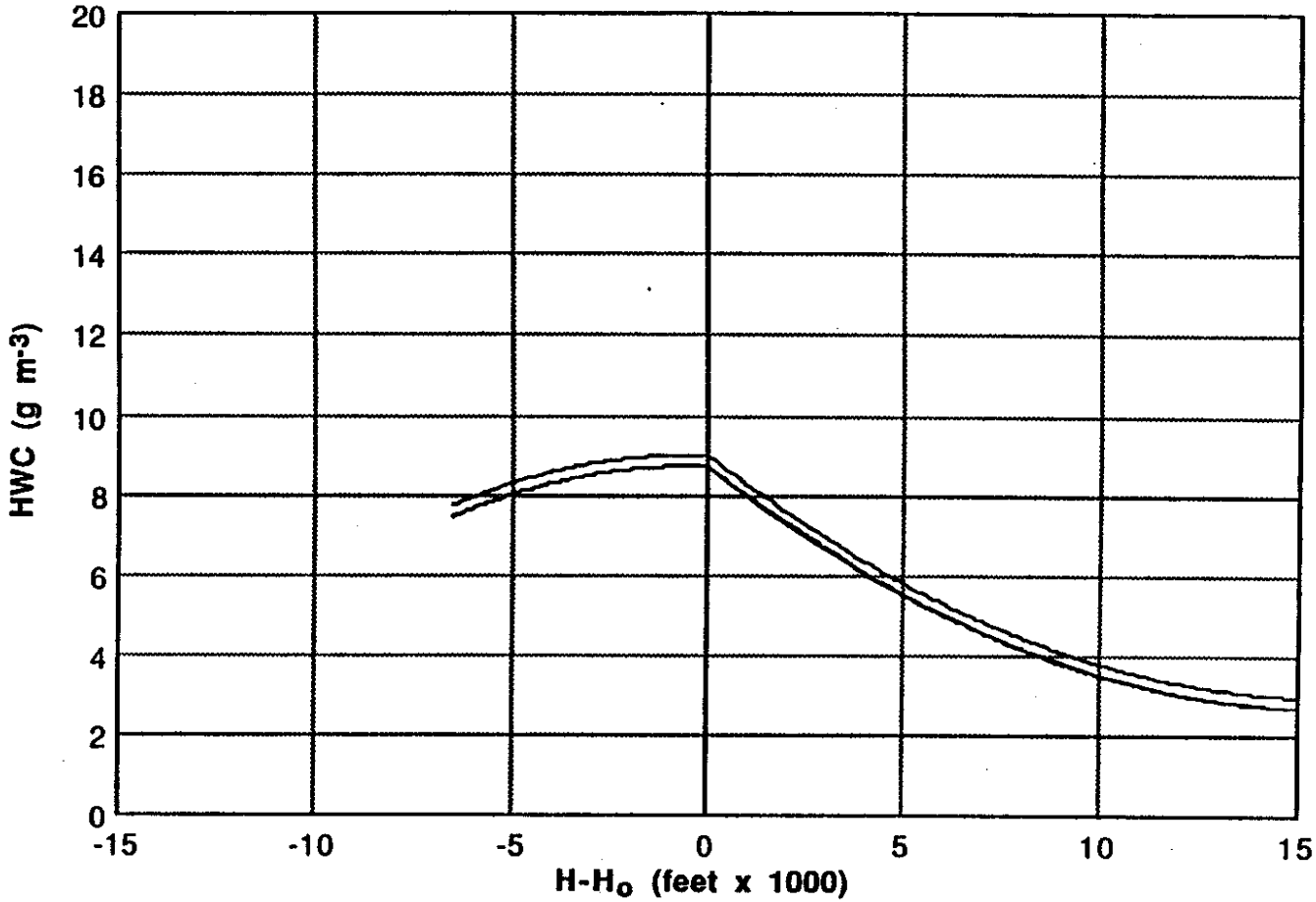

Fig. 7.6. HWC as a function of height, H, above the freezing level height, H_o. The upper curve is CFMI-derived, while the lower curve is Boeing-derived. The values at $H-H_o = 0$ are the airplane threat curve 10^{-8} probability values.

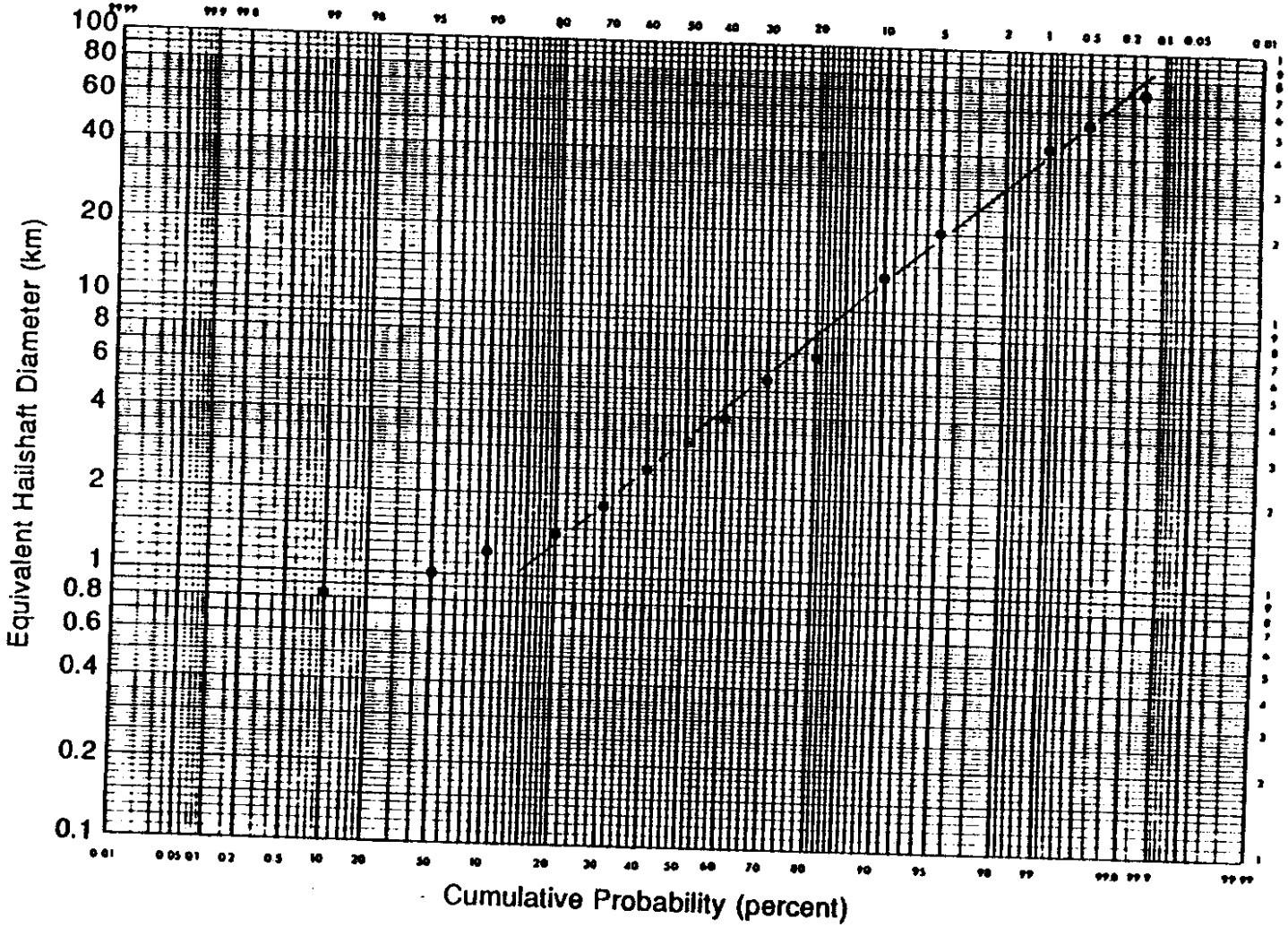

Fig. 8.1. Cumulative distribution of equivalent hailshaft diameters (ARC data). The straight line is the cumulative log normal distribution.

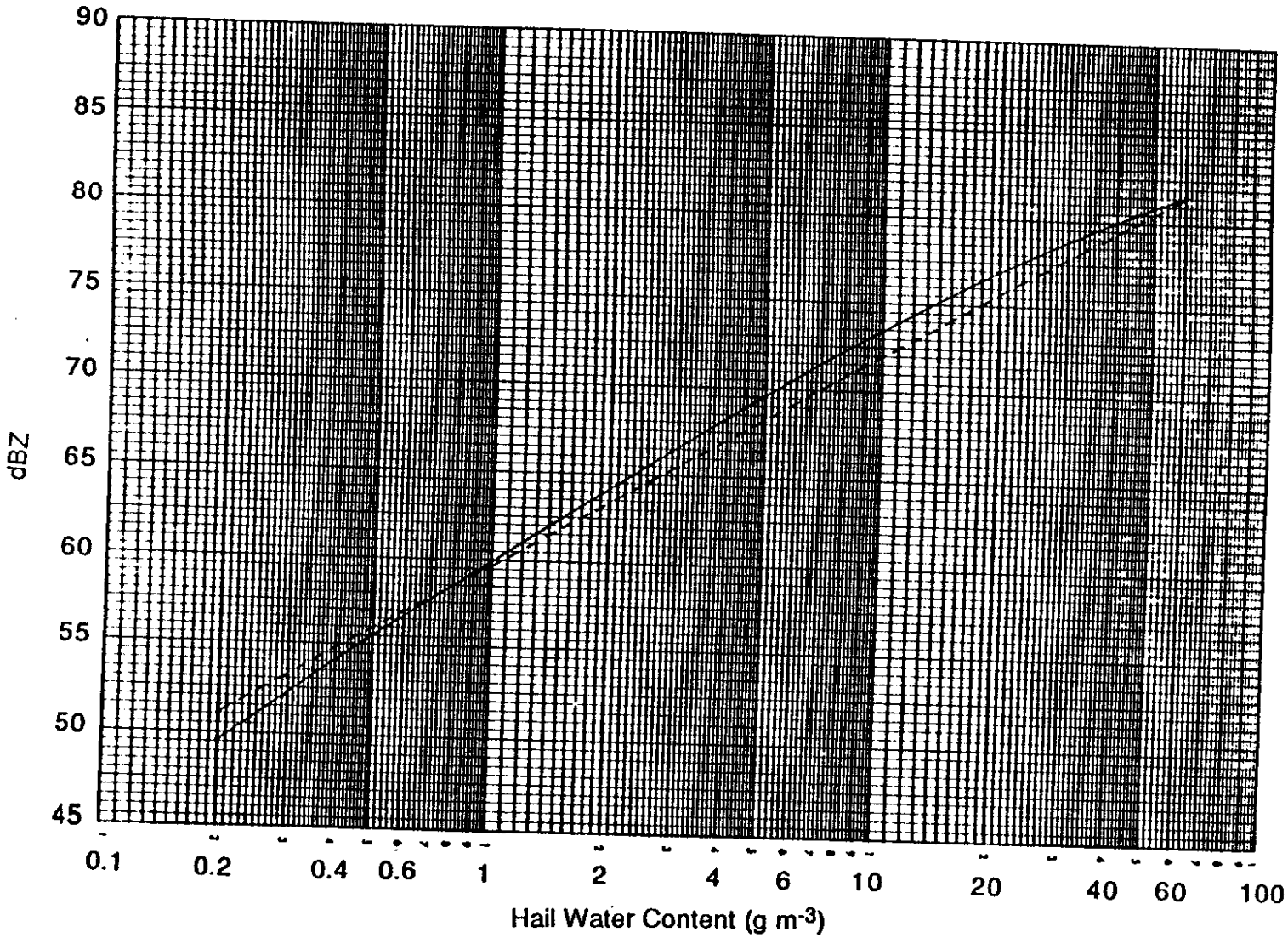

Fig. 8.2. Comparison of dBZ versus HWC from the Ulbrich and Atlas (1982) equation (dashed line) and from the integrated Mie scattering coefficients (solid line).

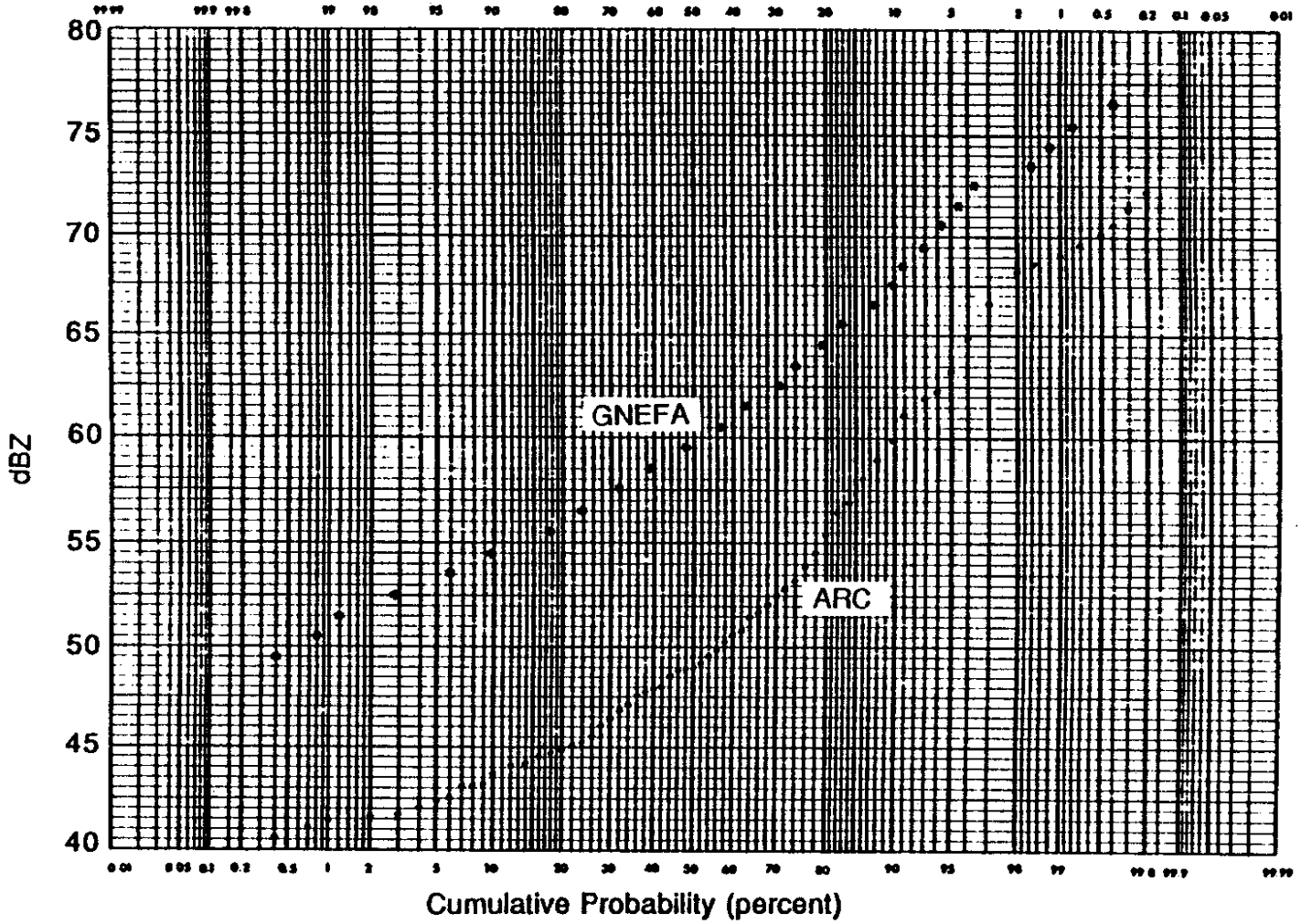

Fig. 8.3. Cumulative dBZ distributions from the ARC (points) and GNEFA (asterisks) data.

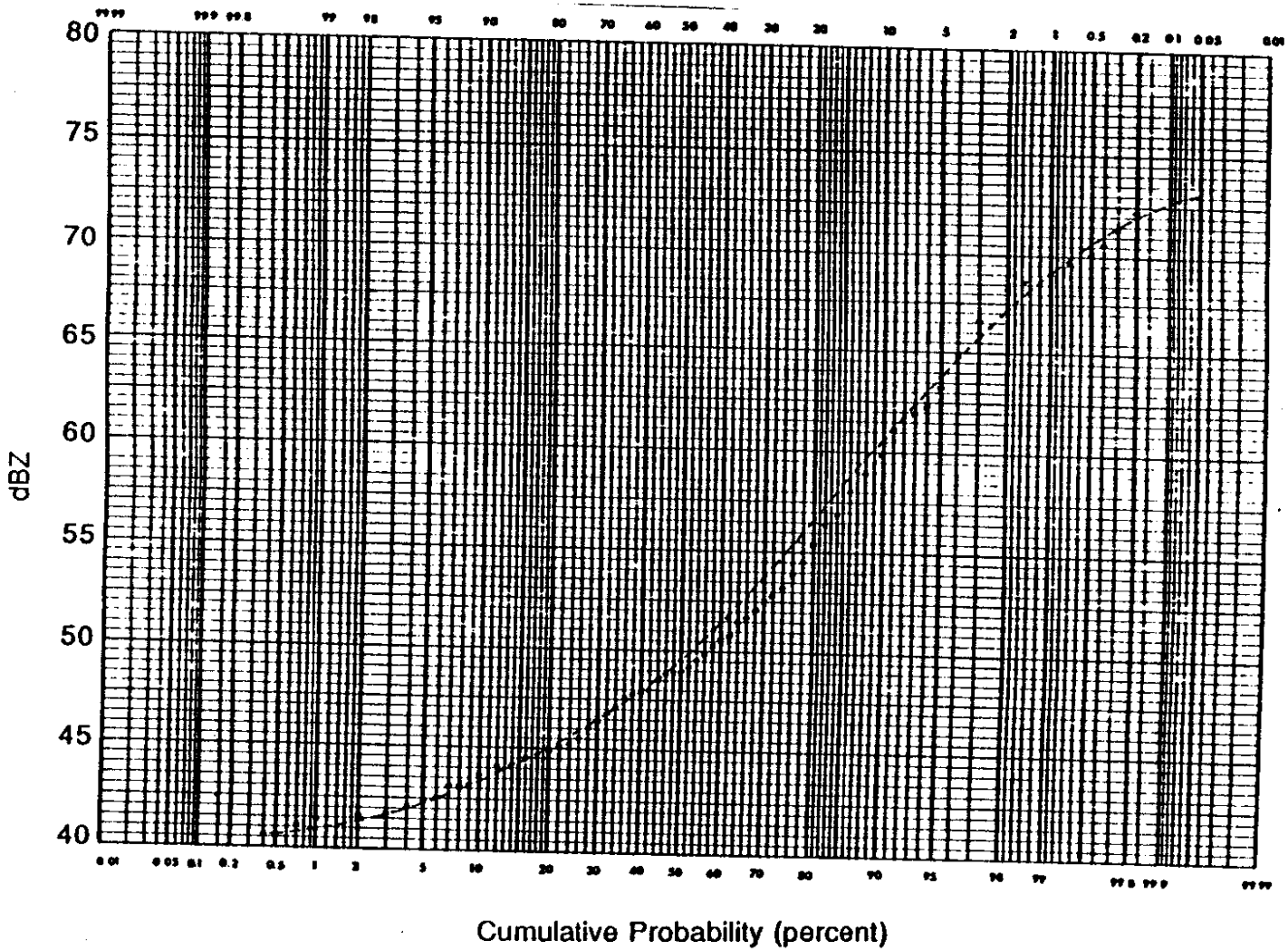

Fig. 8.4. The cumulative beta distribution (dashed line) fitted to the ARC data sample distribution.

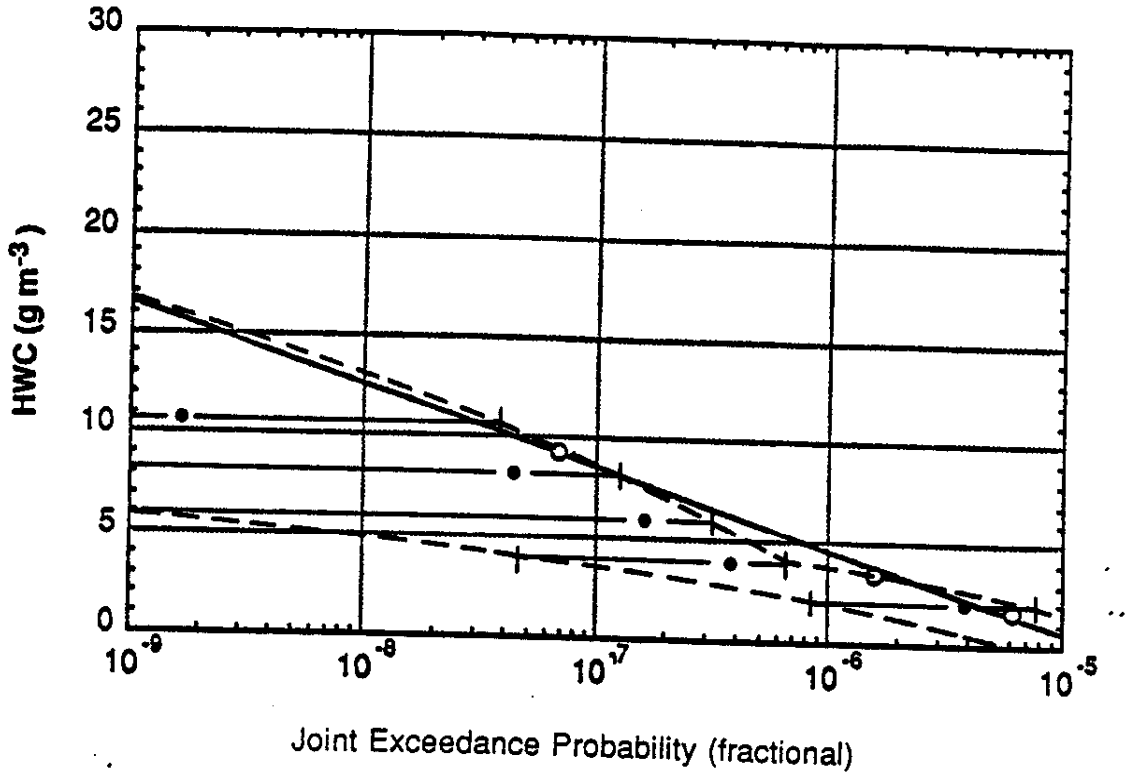

Fig. 8.5. The HWC threat curve (solid line) and the associated 3-sigma error band (dashed lines).

FIGURE 9.1:
AIRCRAFT FLIGHT PATH THROUGH A HAIL SHAFT

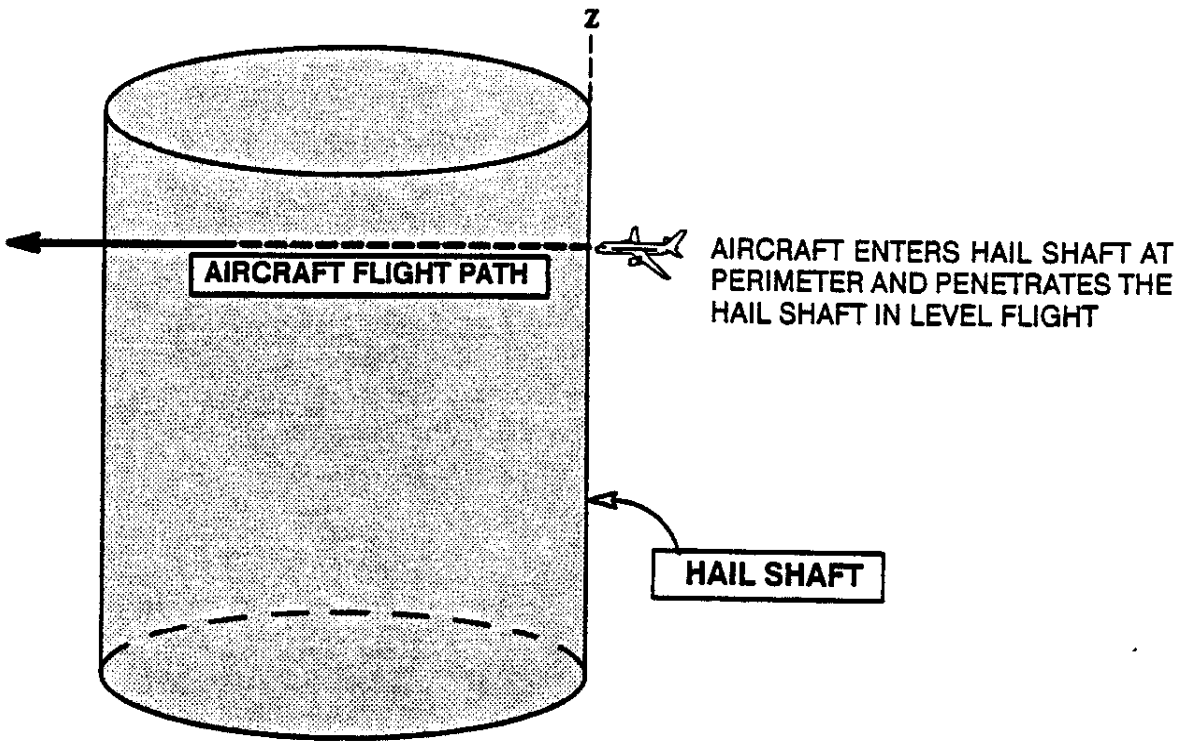

FIG. 9.1a: SIDE VIEW OF HAIL SHAFT

Figure 9.1a shows the aircraft entering a hail shaft. The hail shaft is represented by a cylinder of constant HWC. The airplane enters the side of the shaft and crosses the shaft at an angle relative to the tangent.

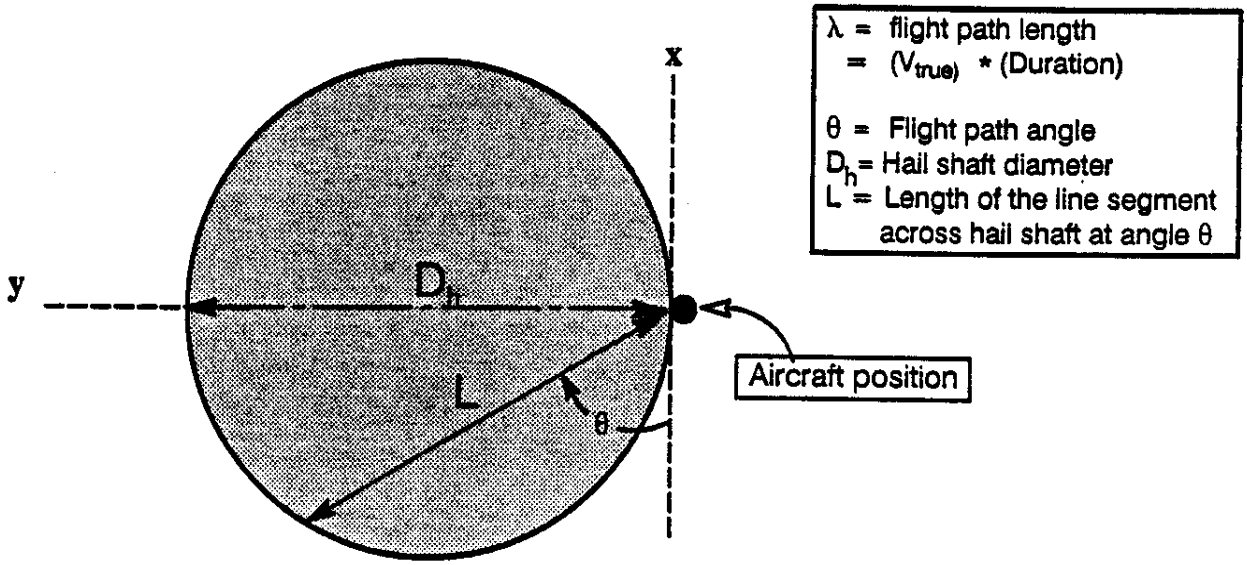

FIG. 9.1b: TOP VIEW OF HAIL SHAFT

Figure 9.1b shows a top view of Fig. 9.1a. The aircraft passes through the hail shaft at angle "θ". "L" is the length of line segment across hail shaft at the angle θ. The hail shaft diameter is "D".

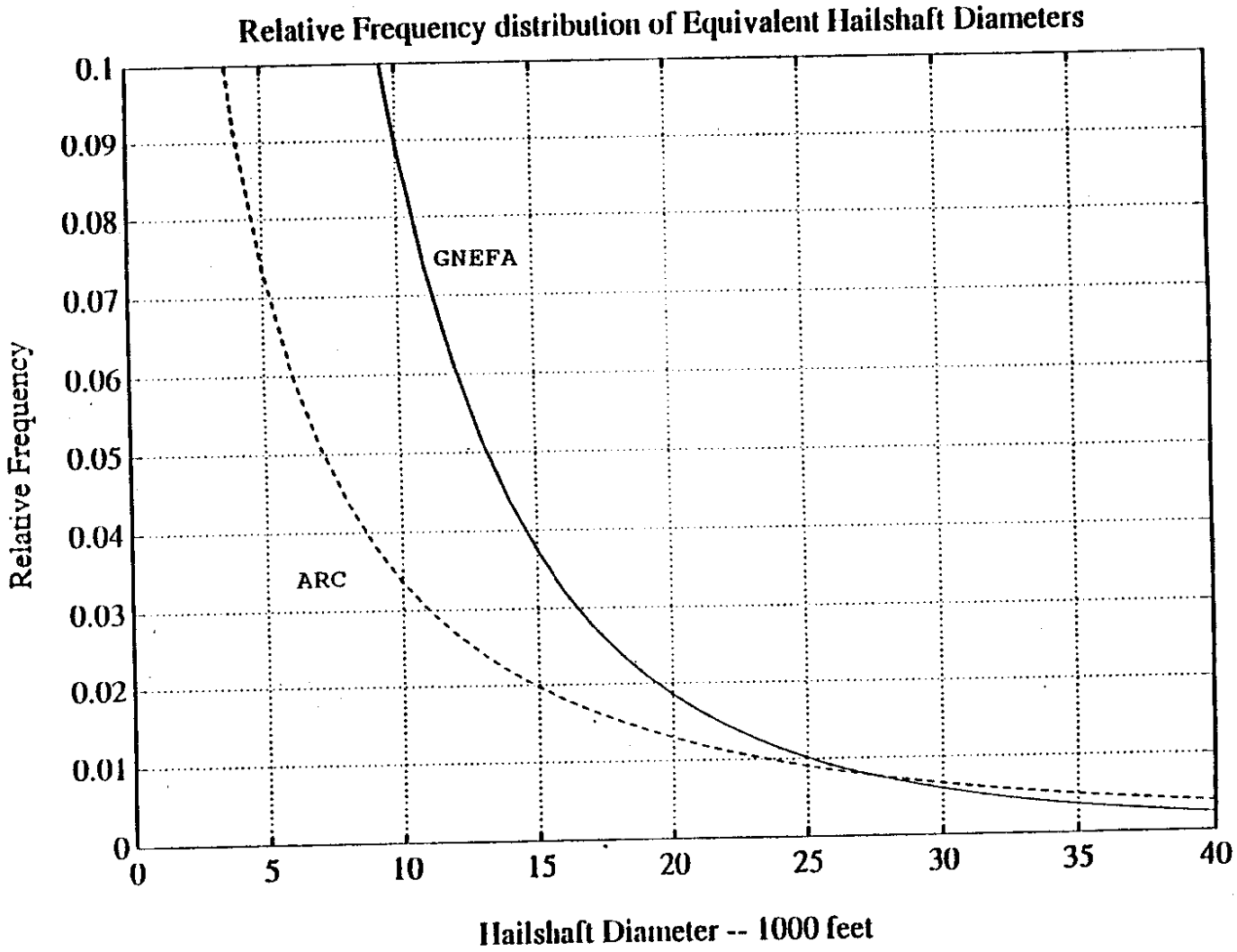

Figure 9.2 shows the relative frequency distribution of equivalent hailshaft diameters derived from data provided by ARC and GNEFA. The ARC frequency distribution was derived from dual-polarization radar measurements. The GNEFA frequency distribution was obtained from hail pad measurements.

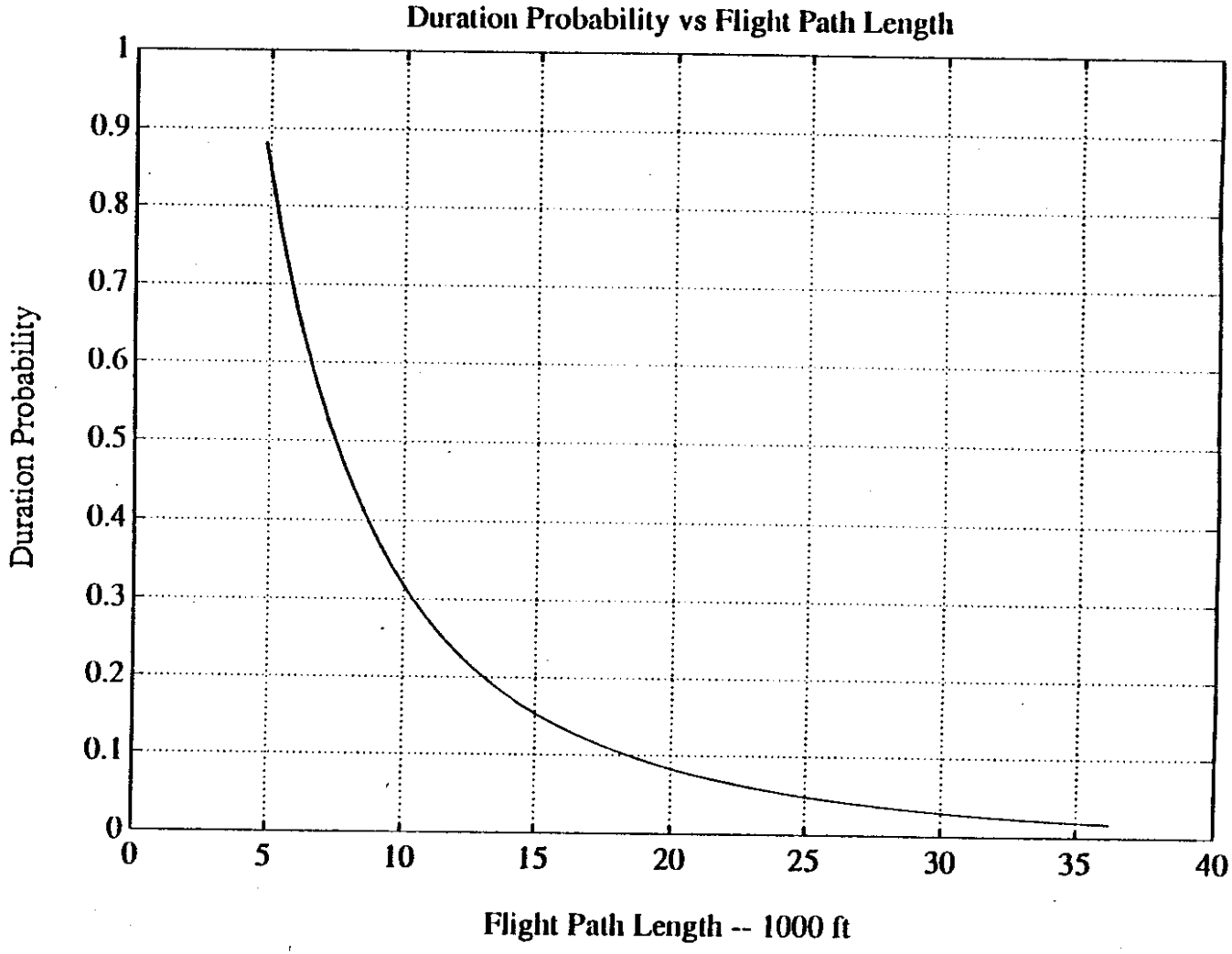

Figure 9.3 shows duration probability as a function of the flight path length. Figure 9.3 was obtained by numerically integrating Eq. 9.7.

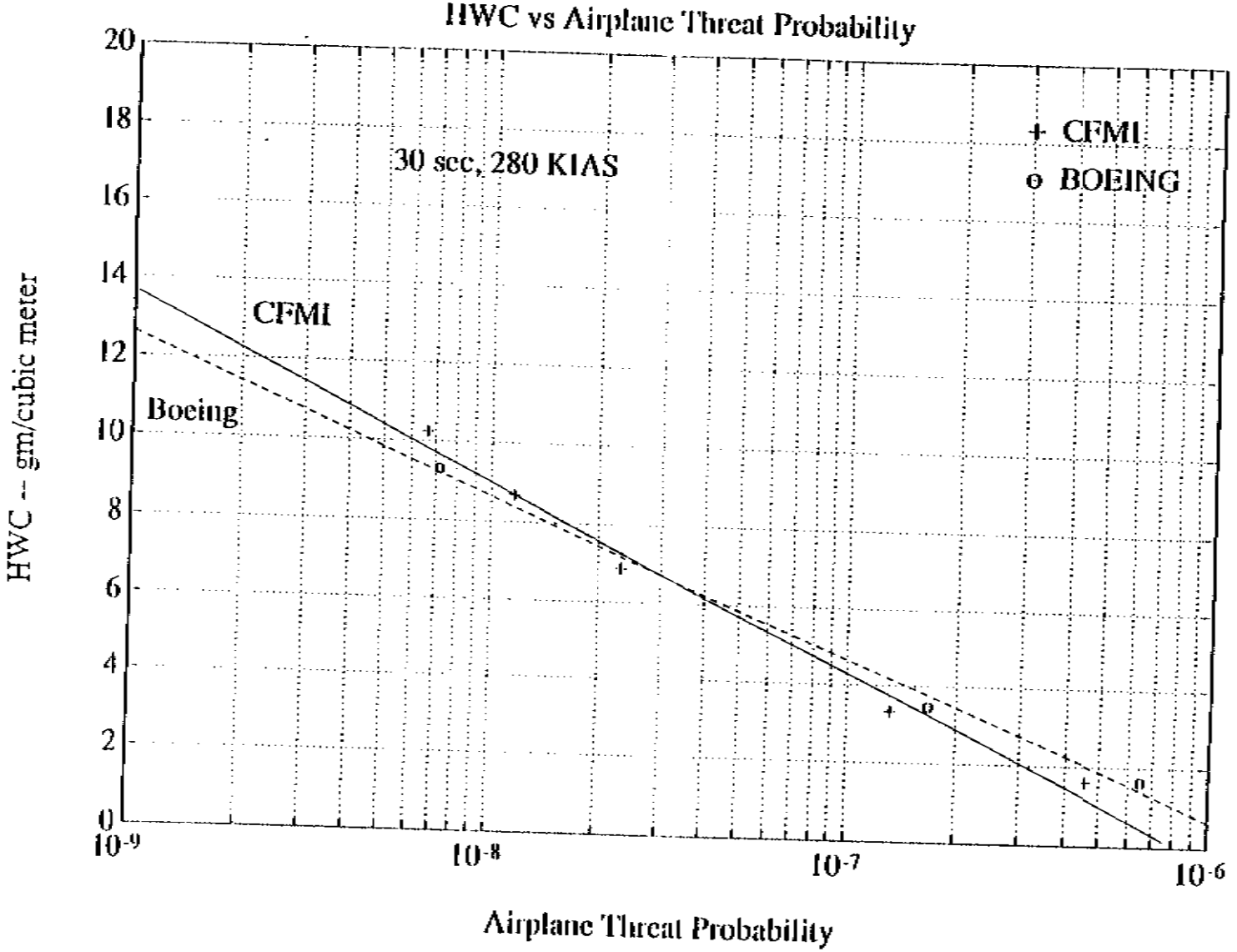

Figure 9.4 shows the Boeing and CFMI airplane threat curves for a 30 second duration probability at 280 KIAS and 0°C T_{amb}. The Boeing curve is applicable to an altitude of 15,000 ft. The CFMI curve is applicable to an altitude of 12,000 ft.

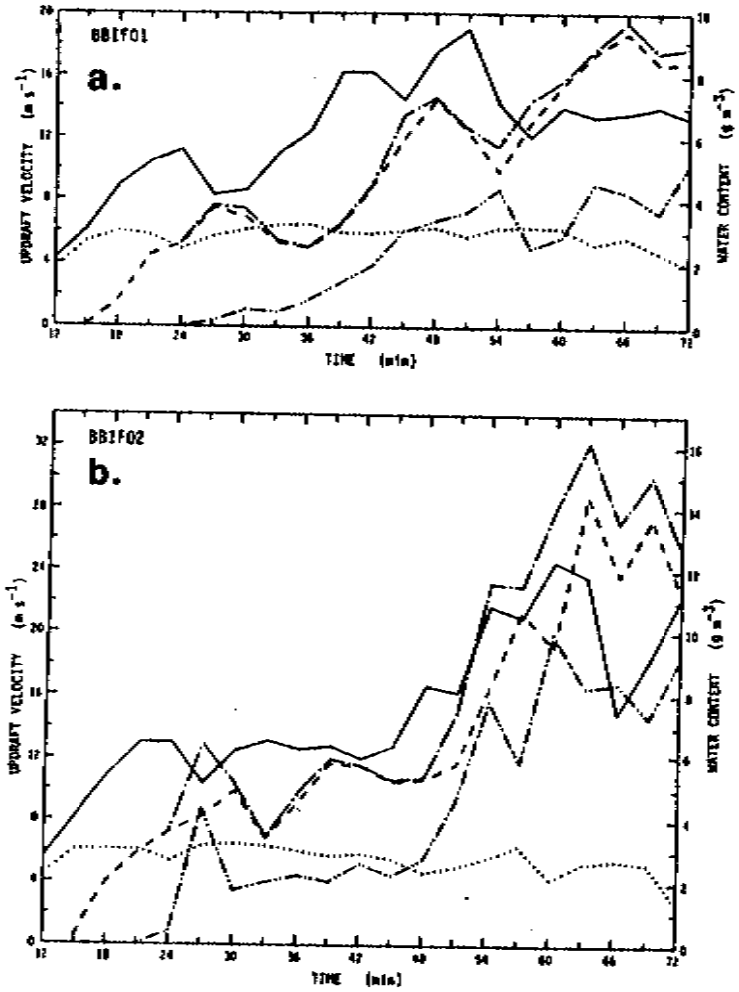

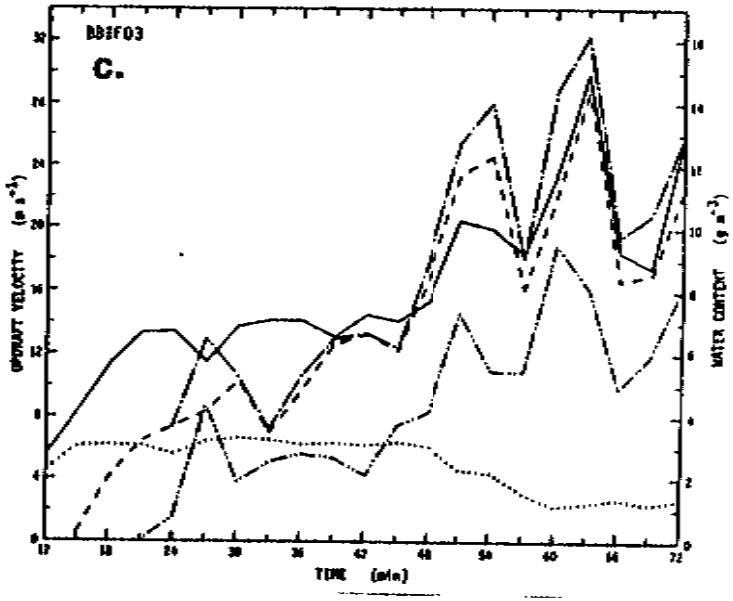

Fig. 10.1. Evolution of the maximum values of updraft velocity, cloud water content, rain content, graupel/hail content, and total precipitation content for the time period 24 to 72 min: a.) case BBIF01, b.) BBIF02, and c.) BBIF03 . The solid line indicates the updraft velocity using the scale on the left axis. The cloud water content is indicated by the dotted line, rain content by the dashed line, graupel/hail content by the double dot-dash line, and total precipitation content by the dot-long dash line, using the scale on the right axis.

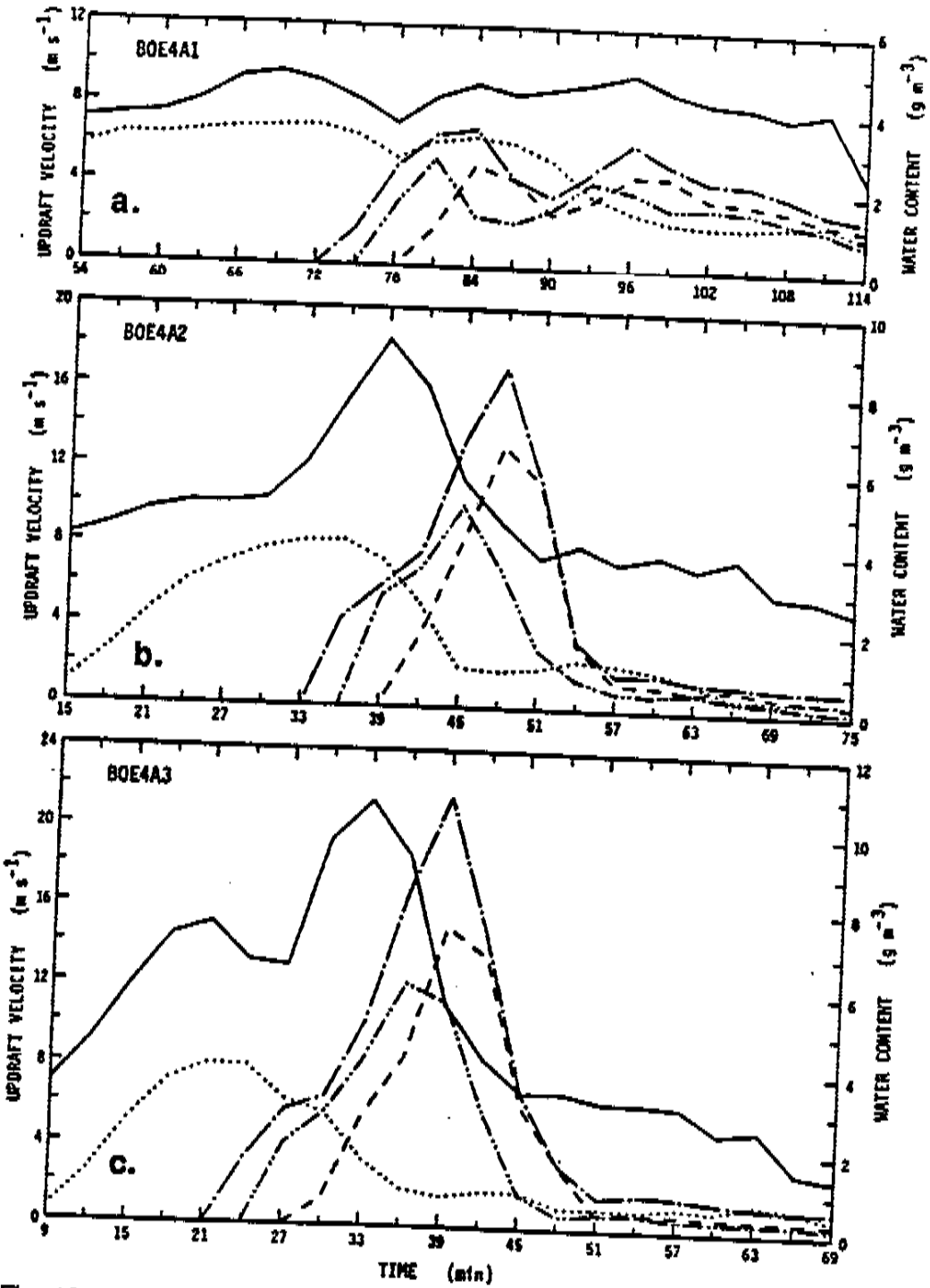

Fig. 10.2. As in Fig. 10.1, but for cases: a.) BOE4A1, b.)BOE4A2, and c.) BOE4A3.

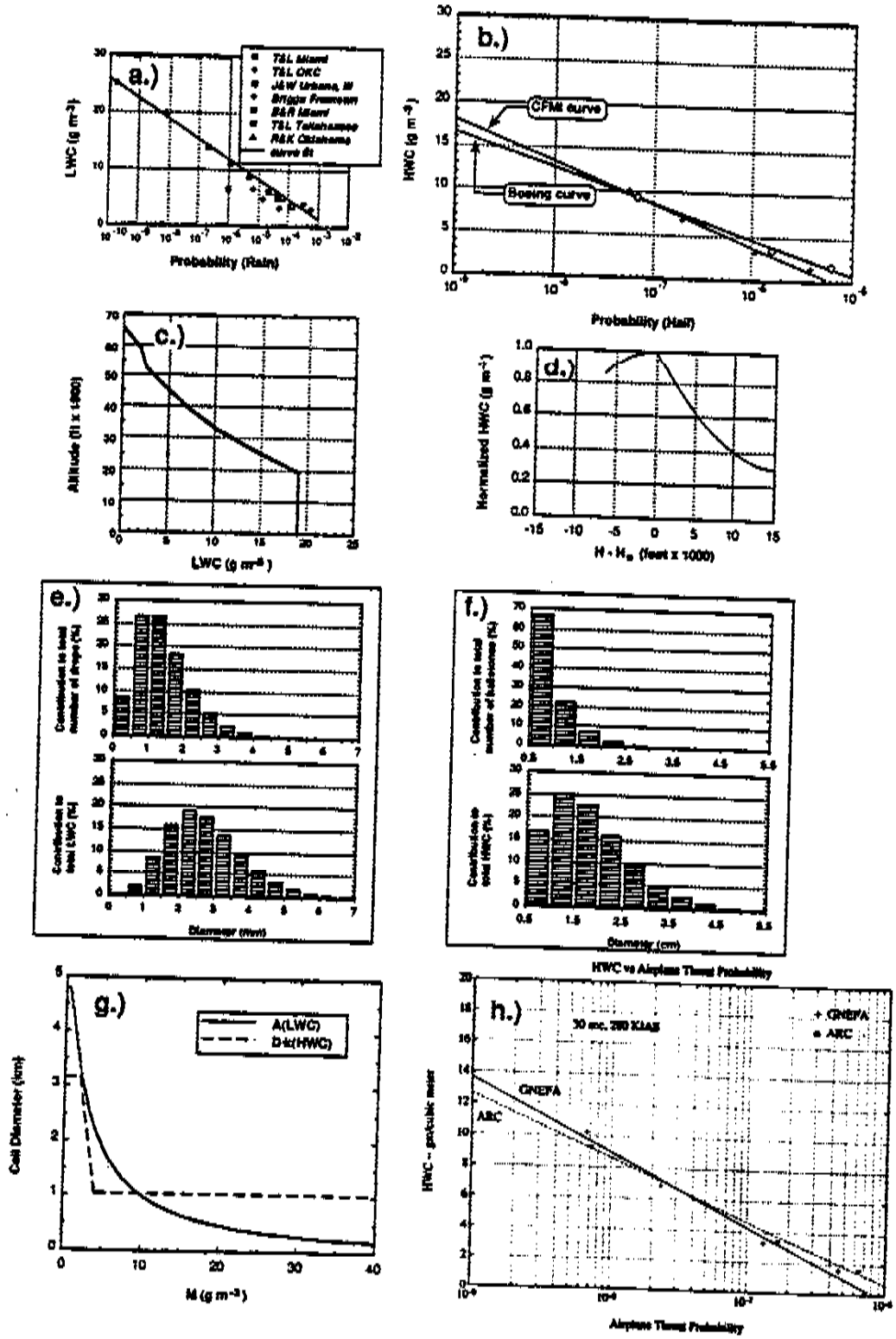

Fig. 11.1. Synthesis of the pertinent figures from this study. a.) Fig. 4.9, b.) Fig. 7.1, c.) Fig. 4.11, d.) Fig. 7.5, e.) Fig. 4.12, f.) Fig. 5.12, g.) Fig. 5.9, h.)Fig. 9.4.

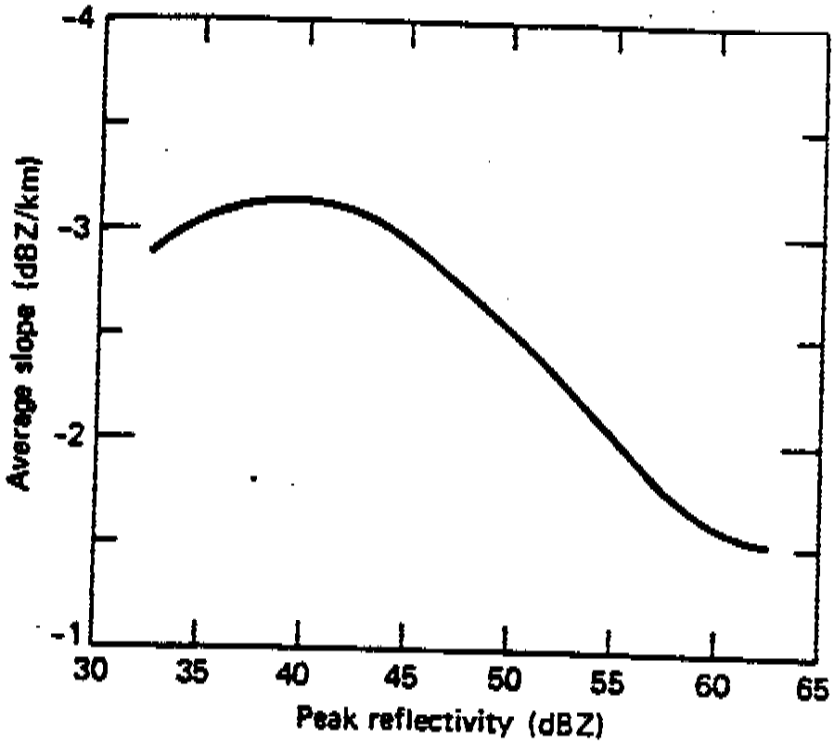

Fig. A.1. Average slope, b, for each core reflectivity interval. (From Konrad, 1978)

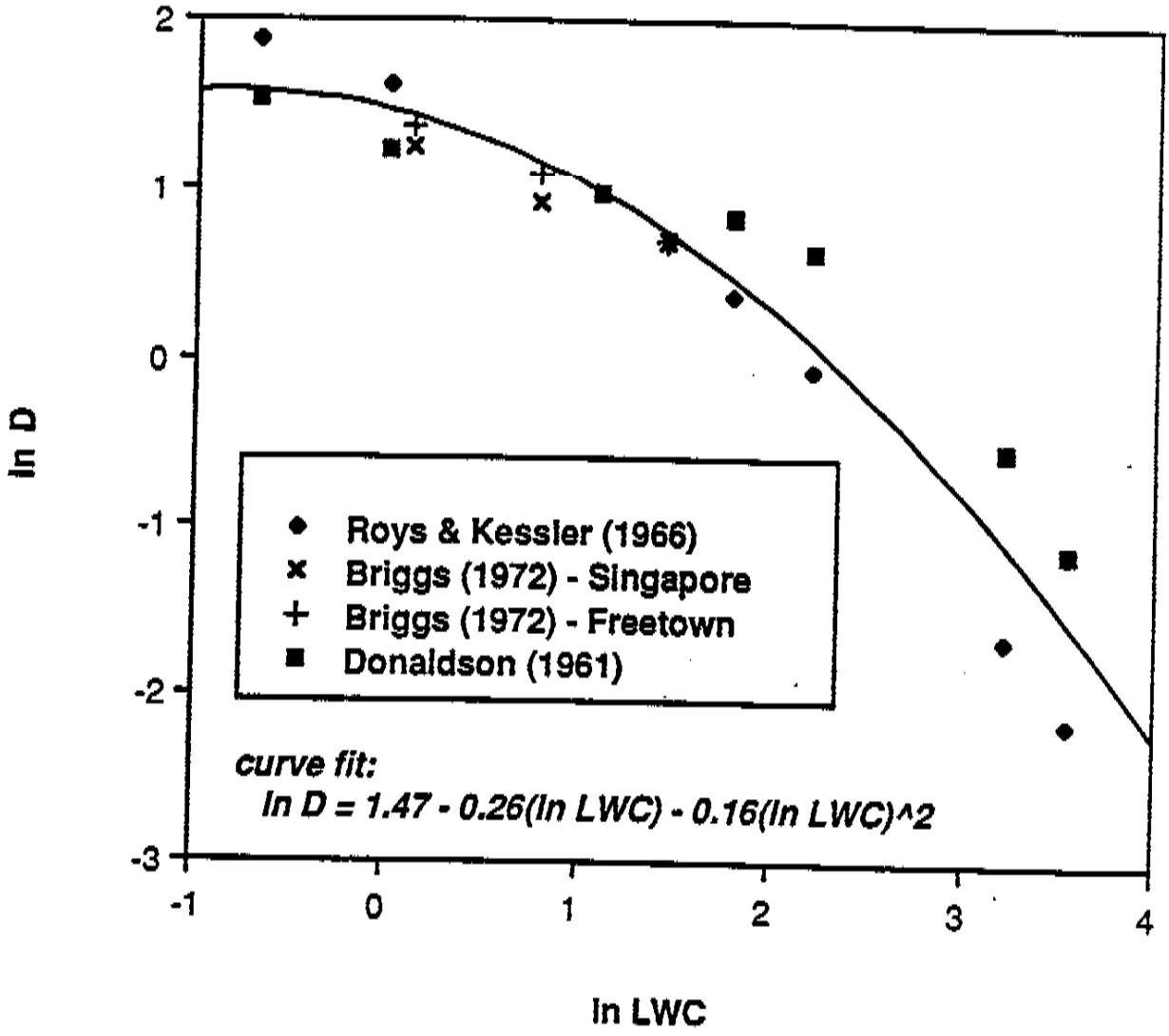

Fig. A.2. Diameter (in units of km) of region in which a given LWC (in units of g m^{-3}) is equalled or exceeded as a function of LWC. Data sources and curve fit equation are given.

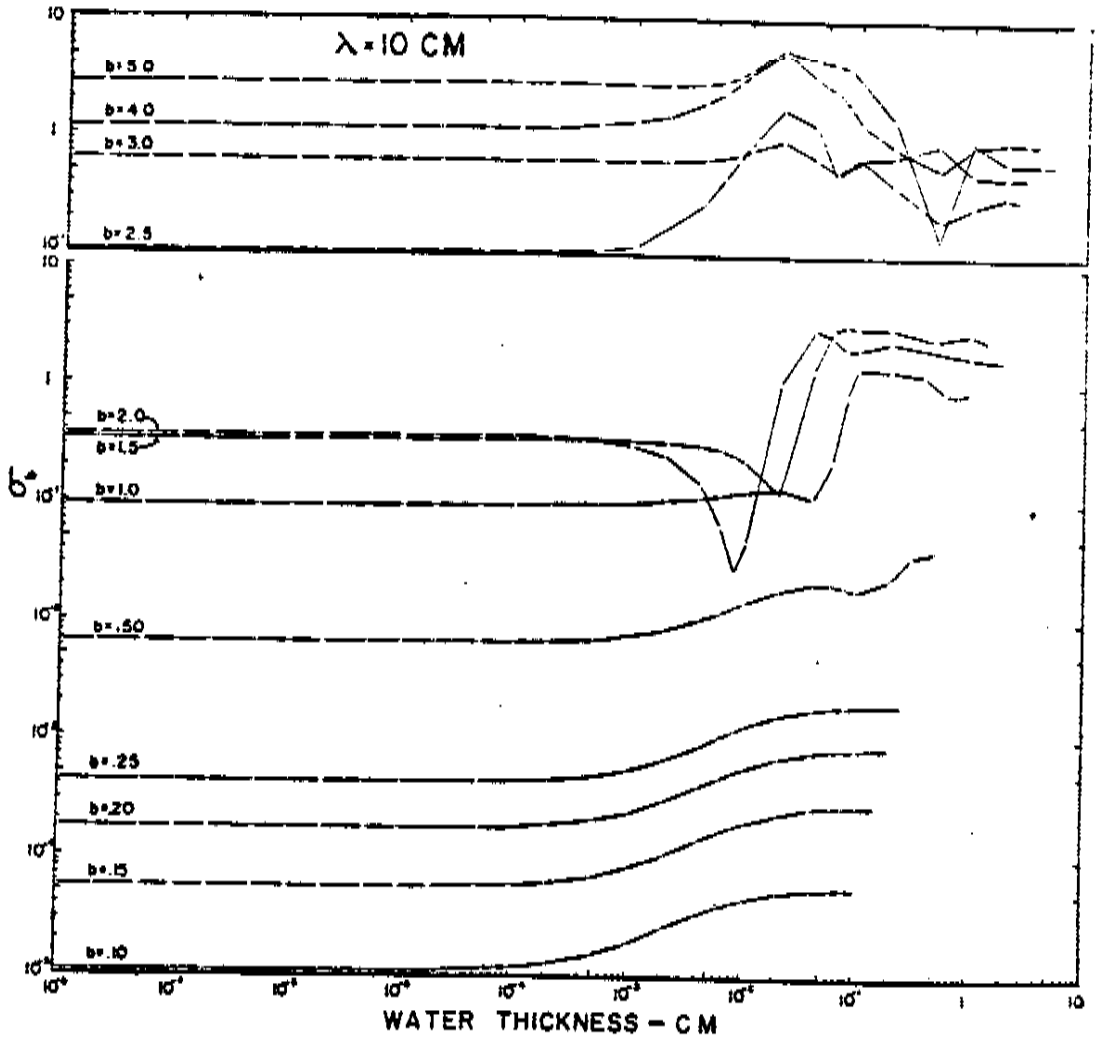

Fig. B.1. Radar back-scattering cross-sections, for a radar wavelength of $\lambda = 10$ cm, of spheres of various radii, b, as a function of the thickness of the water shell surrounding the inner ice sphere. (From Herman and Battan, 1961.)

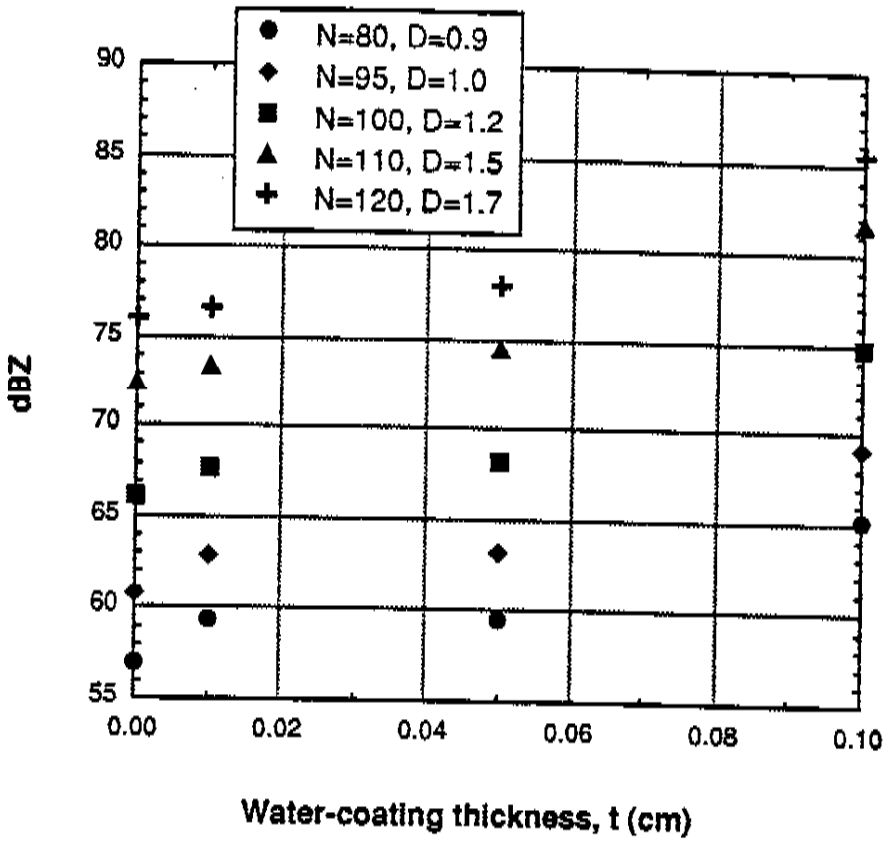

Fig. B.2. Radar reflectivity versus water-coating thickness for five different hail distributions.

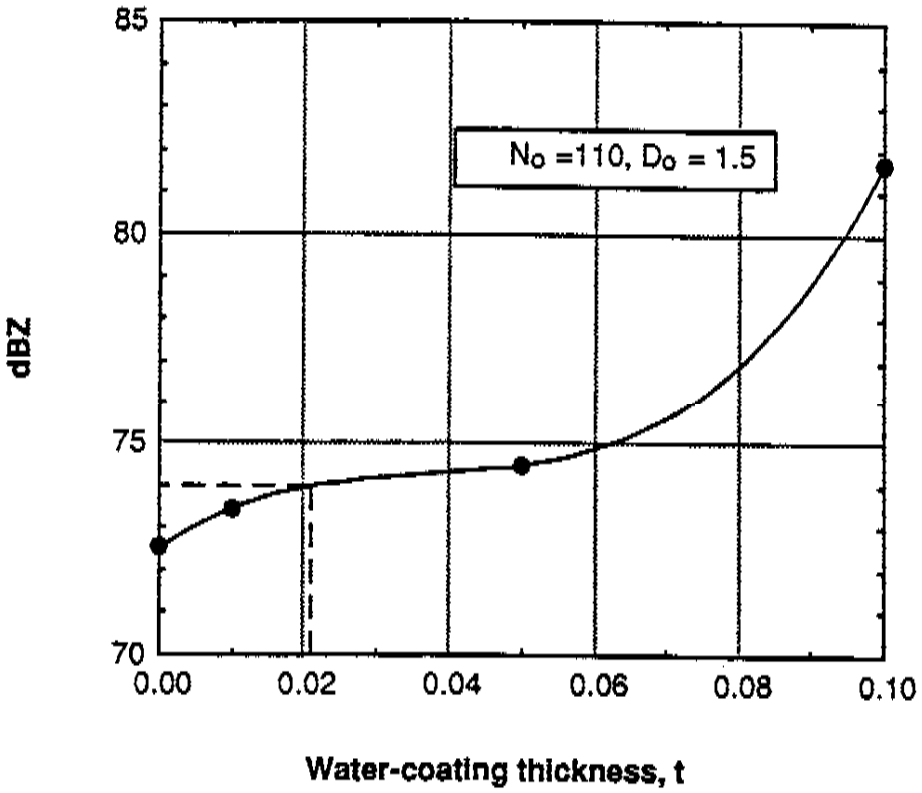

Fig. B.3. Water-coating thickness as a function of reflectivity for a given distribution. Reflectivity for t=0, 0.01, 0.05, and 0.1 cm is calculated using values in Table B.1, then reflectivity at t=0.021 cm is taken from the curve-fit to the 4 points.

--- Table 4.1 ---

Locations of the 42 stations for which Tattelman and Larson (1989) gave rain rate climatology data.

Location	Location
Aberdeen, SD	Newark, NJ
Albuquerque, NM	New Orleans, LA
Allentown, PA	New York, NY
Asheville, NC	Oklahoma City, OK
Bakersfield, CA	Omaha, NE
Billings, MT	Philadelphia, PA
Boise, ID	Phoenix, AZ
Boston, MA	Pittsburg, PA
Cape Hatteras, NC	Raleigh, NC
Charleston, SC	Rapid City, SD
Cheyenne, WY	San Angelo, TX
Chicago, IL	St. Louis, MO
Denver, CO	San Sabastian, PR
Ely, NV	Santa Maria, CA
Grand Junction, CO	Seattle, WA
Houston, TX	Shreveport, LA
Huntsville, AL	Spokane, WA
Internat'l Falls, MN	Tallahassee, FL
Key West, FL	Topeka, KS
Lexington, KY	Urbana, IL
Miami, FL	Yuma, AZ

--- Table 4.2 ---

Locations of the 20 stations for which Bodtmann and Ruthroff (1976) gave rain rate climatology data.

Location	Location
Atlanta, GA	Hudson, NH
Bismarck, ND	Lynchburg, VA
Buffalo, NY	Memphis, TN
Burbank, CA	Miami, FL
Columbia, MO	Milwaukee, WI
Columbus, OH	Newark, NJ
Dallas, TX	New Orleans, LA
Denver, CO	Portland, OR
El Paso, TX	Salt Lake City, UT
Helena, MT	San Diego, CA

--- Table 4.3 ---

Water content data obtained in Oklahoma thunderstorms. (From Roys and Kessler, 1966)

Date	Run No.	Time CST	Altitude to nearest 100 ft.	Aircraft-measured ambient Temperature °C.	Maximum Water content gm. m³	Comment
May 8, 1962	1	1629	30,900	-	15.8	All 4 runs passed through same storm. In addition, 4th run passed through a neighboring storm.
	2	1641	31,000	-	11.9	
			30,000	-	13.9	
	3	1652	32,000	-	12.1	
			31,600	-	10.8	
	4	1706	31,000	-	13.6	
May 20	1	1604	34,300	-	3.0	Runs 1 through 4 were made through the same storm. 5 and 6 were made through separate storms.
	2	1614	34,700	-	1.2	
	3	1625	34,200	-	3.5	
	4	1640	27,400	-	4.5	
	5	1651	27,200	-	6.0	
	6	1701	26,900	-	7.8	
May 20	1	1831	33,300	-45°*	6.7	Runs 1, 2 and 3 passed through the same storm; run 4 passed through a neighboring one.
	2	1839	34,300	-48°*	9.5	
	3	1849	34,100	-48°*	4.9	
	4	1900	29,100	-35°*	43.7	
May 31	1	1815	34,000	-52°	5.3	Only runs 2 and 4 were made in the same storm.
	2	1841	34,700	-52°	3.0	
	3	1850	34,800	-52°	2.5	
	4	1858	34,700	-53°	4.3	
June 5	1	1708	34,800	-45°	7.6	Runs 1, 2 and 3 passed through one storm. It appeared to disintegrate into two storms as the 4th pass began.
			34,800	-52°	5.9	
			34,800	-51°	5.9	
	2	1718	34,900	-51°	5.4	
			34,600	-48°	9.6	
	3	1726	34,000	-49°	7.6	
			33,000	-45°	8.7	
	4	1750	30,000	-38°	3.9	
				Average	8.4	

* Based on soundings made at Oklahoma City

--- Table 4.4 ---

Probability of occurrence of instantaneous rainfall at or exceeding specified intensities (From Briggs, 1972).

	Rainfall intensity (mm/hr)		
	25	50	100
	probability		
Heathrow	1.26×10^{-4}	1.94×10^{-5}	1.14×10^{-6}
Singapore	1.83×10^{-3}	6.85×10^{-4}	1.48×10^{-4}
Freetown	3.31×10^{-3}	1.26×10^{-3}	3.19×10^{-4}

--- Table 4.5 ---

Various equations used to convert rain rate, R, in mm hr^{-1}, to liquid water content, M, in g m^{-3}.

Source	Climate region	M-R Equation	Location where data were collected
Jones, 1956	mid-latitude, continental	$M = 0.052\ R^{0.97}$	Illinois
Mueller & Sims, 1966	subtropical	$M = 0.0528\ R^{0.95}$	Miami
Willis, 1984	tropical	$M = 0.062\ R^{0.913}$	Hurricanes Anita and Frederic

--- Table 4.6 ---

Some maximum LWC data points reported by various authors.

LWC (g m^{-3})	Location	Source	Method of obtaining data
60	Maryland	Riordan and Bourget (1985) Department of Defense (1987)	1-min record rainrate converted to LWC using Willis (1984)
44	Oklahoma	Roys and Kessler (1966)	LWC directly measured by aircraft
29	Florida	Mueller and Sims (1966)	LWC directly measured at ground level
28	Colorado	Kyle and Sands (1973)	LWC directly measured by aircraft
23	"	"	"
22	Florida	Mueller and Sims (1966)	LWC directly measured at ground level

--- Table 4.7 ---

LWC profile used in the weather threat study.
(After Tattelman and Willis, 1985)

Altitude (km MSL)	Ratio of LWC to maximum LWC
0	1.00
2	1.00
4	1.00
6	1.00
8	0.76
10	0.54
12	0.38
14	0.25
16	0.13
18	0.10
20	0.00

— Table 5.1 —

Size of the ARC data base. The numbers below indicate the number of data points from each year.

Year	Maximum hail reflectivity	Hailshaft equivalent diameter
1983	178	1255
1984	117	750
1985	119	863
Total	414	2868

--- Table 5.2 ---

Duration (min) of hailfall at a point according to different authors.
(from Sulakvelidze, 1967)

Author	Location	Minimum	Maximum	Mean
Prohaska	Austria	0.6	50	8-10
Gigineishvili	Eastern Georgia	5-10	-	-
Beckwith	Mountain regions, USA	0.6	45	5
Defur	Belgium	5	20	-
Tverskoi	Rostov Region	5	20	10
Pastukh, Sokhrina	European part of the USSR	2	20-30	15
Chepovskaya	Northern Caucasus	3	30	5-10
Jénève	France	1	90	5-10
Weickmann	USA	-	85	5-10
Mean				6-7

--- Table 5.3 ---

The ARC extreme HWC data. HWC values are the highest that ARC found in the month of July from 1983-85.

YEAR (JULY)	CAPPI ELEVATION (km AGL)	HWC ($g\ m^{-3}$)
1983	2 4 6	8.9 8.6 6.2
1984	2 4 6	5.0 2.9 2.6
1985	2 4 6	10.9 5.1 3.6
1983-85	2 4 6	10.9 8.6 6.2

--- Table 7.1 ---

Various studies reporting data on the height of radar reflectivity maximum values in hailstorms. Heights are given in km MSL.

Location	Height of dBZ_{max} (km)	Height of 0°C level (km)*	Δ Height (km)	Reference
New England	6	4.05	1.95	Donaldson (1961)
Western South Dakota	5.5	4.3	1.2	Dennis *et al.* (1970)
USSR	?	?	1.5 - 2.5	Sulakvelidze (1967)
Central Illinois	4.5 - 6	4.3	0.2 - 1.7	Wilk (1961)

*The freezing levels for New England, South Dakota, and Illinois are the summer (June, July, and August) average at Nantucket, MA, Rapid City, SD, and Rantoul, IL respectively.

--- Table 10.1 ---

Maximum HWC values and elevation for the New Orleans simulations.

Case ID	HWC ($g\ m^{-3}$)	Altitude (km)
B1NOF1	9.74	4.6
B1NOF2	5.95	3.8
B1NOF3	6.57	4.6
BOE1 A02	**4.66**	**5.0**
BNOF05 (Cell 1)	7.09	4.6
(Cell 2)	8.02	6.4
BNOFE5 (Cell 1)	6.33	3.6
(Cell 2)	7.43	5.0
BNOFE3 (Cell 1)	5.88	4.8
(Cell 2)	8.15	2.8
BNOFE2 (Cell 1)	5.66	4.8
(Cell 2)	8.50	2.8
BNOFC5 (Cell 1)	7.33	5.4
(Cell 2)	14.02	5.6

--- Table 10.2 ---

Maximum HWC values and elevation for the Philadelphia simulations.

Case ID		HWC ($g\ m^{-3}$)	Altitude (km)
B2DLF1		9.33	4.8
B2DLF2		5.68	4.6
B2DLF3		7.62	4.6
B2DLF4		7.66	4.2
BOE2 B01		**3.10**	**3.8**
BDLF01	(Cell 1)	5.11	5.0
	(Cell 2)	4.68	3.4
BDLF02	(Cell 1)	5.70	5.0
	(Cell 2)	6.67	4.8
BDLFE2	(Cell 1)	5.32	4.8
	(Cell 2)	7.03	4.6
BDLFE3	(Cell 1)	4.72	4.6
	(Cell 2)	6.14	3.8
BDLFE4	(Cell 1)	4.11	5.6
	(Cell 2)	4.58	4.0

--- Table B.1 ---

Values of constants for calculating radar reflectivity as a function of N_0 and D_0 for various water-coating thicknesses, t, and radar wavelengths, λ. (From Ulbrich and Atlas, 1982.)

$$Z = \alpha N_0 D_0^m \epsilon^{-\Delta D_0}.*$$

λ (cm)	t (cm)	α	m	ϵ
3.21	0	4.67×10^3	5.97	0.629
	0.01	1.09×10^4	5.88	0.967
	0.05	1.65×10^5	6.90	2.43
	0.10	2.63×10^5	7.05	2.67
5.50	0	4.05×10^4	7.40	1.70
	0.01	1.69×10^5	6.10	0.629
	0.05	5.21×10^5	8.19	2.40
	0.10	1.49×10^6	8.68	2.99
10.0	0	2.89×10^4	7.37	0.844
	0.01	5.95×10^4	6.95	1.07
	0.05	2.71×10^4	6.39	0.234
	0.10	2.16×10^5	7.94	0.931

* Z ($mm^6\ m^{-3}$), N_0 ($m^{-3}\ cm^{-1}$), D_0 (cm).